Designing next generation high energy density lithium-ion battery with manganese orthosilicate-capped alumina nanofilm

UNIVERSITY *of the*
WESTERN CAPE

By

Miranda Mengwi Ndipingwi
(BSc Honours)

A mini-thesis submitted in partial fulfilment of the requirements for the degree of

Magister Scientiae in Nanoscience

Faculty of Science
University of the Western Cape
Cape Town / South Africa

Supervisor: Prof. Emmanuel Iwuoha

Co-supervisor: Dr. Chinwe Ikpo

December 2015

Key Words

Lithium-ion battery

Lithium manganese orthosilicate cathode

Aluminum oxide nanofilm

Solid-state Nuclear Magnetic Resonance Spectroscopy

X-ray Photoelectron Spectroscopy

Cyclic Voltammetry

Quasi-reversible electron transfer

Electrochemical Impedance Spectroscopy

Charge transfer resistance

Abstract

Designing next generation high energy density lithium-ion battery with manganese orthosilicate-capped alumina nanofilm

Miranda Mengwi Ndipingwi

MSc. Nanoscience, Department of Chemistry, University of the Western Cape

December 2015

In the wide search for advanced materials for next generation lithium-ion batteries, lithium manganese orthosilicate, Li_2MnSiO_4 is increasingly gaining attention as a potential cathode material by virtue of its ability to facilitate the extraction of two lithium ions per formula unit, resulting in a two-electron redox process involving Mn^{2+}/Mn^{3+} and Mn^{3+}/Mn^{4+} redox couples. This property confers on it, a higher theoretical specific capacity of 333 $mAhg^{-1}$ which is superior to the conventional layered $LiCoO_2$ at 274 $mAhg^{-1}$ and the commercially available olivine $LiFePO_4$ at 170 $mAhg^{-1}$. Its iron analogue, Li_2FeSiO_4 has only 166 $mAhg^{-1}$ capacity as the Fe^{4+} oxidation state is difficult to access. However, the capacity of Li_2MnSiO_4 is not fully exploited in practical galvanostatic charge-discharge tests due to the instability of the delithiated material which causes excessive polarization during cycling and its low intrinsic electronic conductivity. By reducing the particle size, the electrochemical performance of this material can be enhanced since it increases the surface contact between the electrode and electrolyte and further reduces the diffusion pathway of lithium ions. In this study, a versatile hydrothermal synthetic pathway was employed to produce nanoparticles of Li_2MnSiO_4, by carefully tuning the reaction temperature and the concentration of the metal precursors. The nanostructured cathode material was further coated with a thin film of aluminium oxide in order to modify its structural and electronic properties. The synthesized materials were characterized by microscopic (HRSEM and HRTEM), spectroscopic (FTIR, XRD, SS-NMR, XPS) and electrochemical techniques (CV, SWV and EIS). Microscopic techniques revealed spherical morphologies with particle sizes in the range of 21-90 nm. Elemental distribution maps obtained from HRSEM for the novel cathode material showed an even distribution of elements which will facilitate the removal/insertion of Li-ions and electrons out/into the cathode

material. Spectroscopic results (FTIR) revealed the vibration of the Si-Mn-O linkage, ascertaining the complete insertion of Mn ions into the SiO_4^{4-} tetrahedra. XRD and ^7Li MAS NMR studies confirmed a $Pmn2_1$ orthorhombic crystal pattern for the pristine Li_2MnSiO_4 and novel Li_2MnSiO_4/Al_2O_3 which is reported to provide the simplest migratory pathway for Li-ions due to the high symmetrical equivalence of all Li sites in the unit cell, thus leading to high electrochemical reversibility and an enhancement in the overall performance of the cathode materials. The divalent state of manganese present in $Li_2Mn^{2+}SiO_4$ was confirmed by XPS surface analysis. Scan rate studies performed on the novel cathode material showed a quasi-reversible electron transfer process. The novel cathode material demonstrated superior electrochemical performance over the pristine material. Charge/discharge capacity values calculated from the cyclic voltammograms of the novel and pristine cathode materials showed a higher charge and discharge capacity of 209 mAh/g and 107 mAh/g for the novel cathode material compared to 159 mAh/g and 68 mAh/g for the pristine material. The diffusion coefficient was one order of magnitude higher for the novel cathode material (3.06×10^{-6} cm^2s^{-1}) than that of the pristine material (6.79×10^{-7} cm^2s^{-1}), with a charge transfer resistance of 1389 Ω and time constant (τ) of 1414.4 s rad^{-1} for the novel cathode material compared to 1549 Ω and 1584.4 s rad^{-1} for the pristine material. The higher electrochemical performance of the novel Li_2MnSiO_4/Al_2O_3 cathode material over the pristine Li_2MnSiO_4 material can be attributed to the alumina nanoparticle surface coating which considerably reduced the structural instability intrinsic to the pristine Li_2MnSiO_4 cathode material and improved the charge transfer kinetics.

Declaration

I hereby declare that,"**Designing next generation high energy density lithium-ion battery with manganese orthosilicate-capped alumina nanofilm"** is my own work and it has not been submitted before for any degree or examination in any other university, and all the sources I have used or quoted have been indicated or acknowledged by way of complete references.

Miranda Mengwi Ndipingwi

Signed: _____ Date:

Acknowledgements

First and foremost, I would like to give the Almighty God all the glory and adoration for blessing me with the strength, wisdom and courage to complete this work with the best of my ability.

My very sincere gratitude goes to my supervisor, Prof Emmanuel Iwuoha, for his great guidance and for giving me the opportunity to be part of the SensorLab research group.

To my co-supervisor, Dr Chinwe Ikpo, many thanks for your support, advice and mentorship. I truly admire your love for teaching and guiding your students.

To my mum, Mrs Suzan Ndipingwi, my lovely brothers and sisters, Mr/Mrs Adolf and Rosaline Kuja, Mr/Mrs John Ndipingwi, Mr/Mrs Linus Ndipingwi, Mr/Mrs Julius Ndipingwi, Patrick Ndipingwi, Mr/Mrs Davidson Ndipingwi, Fidelis Ndipingwi, Nicoline Ndipingwi, father and mother-in-law Mr Paul Anonchuh and Mrs Martha Anonchuh, brothers and sister-in-law, Elvis Anonchuh, Claudette Anonchuh, Lessly Anonchuh, Divine Anonchuh and family; Dr/Mrs Ignatius and Odilia Ticha, Dr/Mrs Lawrence and Victoir Ticha. Thank you all for your love, constant prayers, support and encouragements.

To my beloved husband, Eric Awa Anonchuh and my charming boy, Felix-Ryan Awa Anonchuh, thank you two for always being there for me, supporting me, caring for me and giving me reason to focus and never give up.

To the Department of Chemistry staff especially Prof P. Baker, Dr F. Ajayi, Dr T. Waryo and Mrs W. Jackson, thank you for your support and encouragements.

My appreciation also goes to SensorLab senior researchers and colleagues especially Dr M. Milua, Anne Lutgarde Djoumessi, Ntuthuko Wonderboy, Lerato Molefe, Anovuyo Jonnas, Lindsay Wilson, Xolani Simelani, Unathi Sidwaba, Ezo Nxusani and all my Nanoscience friends. Thank you all for your great support and friendship. You have indeed been a great team to work with.

I will also like to thank the Nanoscience and Nanotechnology Postgraduate Teaching and Training platform especially Mrs V. Jamalie and Mrs C. Abrahams for their constant support and the Department of Science and Technology for awarding me the MSc Nanoscience scholarship.

Table of Contents

Title Page i

Key Words ii

Abstract iii

Declaration v

Acknowledgements vi

Table of Contents vii

Acronyms and Abbreviation ix

List of Figures xi

List of Tables xiv

List of Schemes xv

CHAPTER 1 1

Chapter Overview 1

1.0 Introduction 1

1.1 General Background 1

1.2 Problem statement 6

1.3 Rationale and motivation for the research 6

1.4 Research aims and objectives 8

1.5 Research framework 8

1.6 Thesis outline 9

CHAPTER 2 11

Chapter Overview 11

2.0 Literature Review 11

2.1 Electrochemical energy Storage and fundamental aspects 11

2.2 Battery systems for energy storage applications 14

2.2.1 Lead-acid batteries 15

2.2.2 Sodium-sulfur batteries 16

2.2.3 Flow batteries 17
2.2.4 Nickel-Cadmium batteries 19
2.2.5 Nickel-metal hydride batteries 20
2.2.6 Lithium-ion batteries 21
2.3 Basic Concepts in Lithium-ion batteries 23
2.3.1 Potential 23
2.3.2 Theoretical capacity 26
2.3.3 Coulombic Efficiency 26
2.3.4 C-rates 27
2.4 Materials in Lithium-ion batteries 27
2.4.1 Cathode materials for lithium-ion batteries 27
2.4.2 Anode Materials 35
2.4.3 Electrolytes 40
2.4.4 Separator 42
2.5 Significance of Nanotechnology on the performance of Li-ion batteries 42
CHAPTER 3 45
Chapter Overview 45
3.0 Experimental Section 45
3.1 Chemicals 45
3.2 Procedures 45
3.2.1 Synthesis of Nanostructured pristine Li_2MnSiO_4 cathode material 46
3.2.2 Synthesis of the Novel lithium manganese orthosilicate-capped alumina nanofilm 46
3.3 Material characterisation techniques and instrumentation 47
3.3.1 Structural and spectroscopic characterisation techniques/ instrumentation 48
3.3.2 Electrochemical Characterisation techniques and instrumentation used 55
..... 62

CHAPTER 4 63

Chapter Overview 63

4.0 RESULTS AND DISCUSSION 63

4.1 Microscopic Techniques 63

4.1.1 High-Resolution Scanning Electron Microscopic Studies 63

4.1.2 High-Resolution Transmission electron Microscopic Studies 72

4.2 Spectroscopic Techniques 75

4.2.1 Fourier Transform Infra-Red Spectroscopic Studies 75

4.2.2 X-ray Diffraction Studies 76

4.2.3 Solid-state Nuclear Magnetic Resonance Spectroscopic Studies 79

4.2.4 X-ray Photoelectron Spectroscopic Studies 82

4.3 Electrochemical Techniques 85

4.3.1 Cyclic Voltammetric Studies 85

4.3.2 Square wave Voltammetric investigation 93

4.3.3 Electrochemical Impedance Spectroscopic Studies 93

CHAPTER 5 100

5.0 Conclusion and recommendations 100

5.1 Conclusion 100

5.2 Recommendations 101

References 102

Acronyms and Abbreviations

CV: Cyclic Voltammetry

SWV: Square Wave Voltammetry

EIS: Electrochemical Impedance Spectroscopy

SS-NMR: Solid-state Nuclear Magnetic Resonance Spectroscopy

XRD: X-ray Diffraction

XPS: X-ray Photoelectron Spectroscopy

FTIR: Fourier Transform Infra-Red Spectroscopy

HRSEM: High resolution Scanning Electron Microscopy

HRTEM: High resolution Transmission Electron Microscopy

R_{ct}: Charge transfer resistance

CPE: Constant phase element

$W_{s:}$ Warburg short component

E_{pa}: Anodic peak potential

I_{pa}: Anodic Peak current

E_{pc}: Cathodic peak potential

I_{pc}: Cathodic peak current

E°: Formal potential

Al_2O_3: Aluminium Oxide (alumina)

Li_2MnSiO_4: Lithium manganese orthosilicate

Li_2MnSiO_4/Al_2O_3: Lithium manganese orthosilicate-alumina capped

Redox: Oxidation-reduction

List of Figures

Figure 1.1: Comparison of different battery technologies in terms of volumetric and gravimetric energy density……. (2)

Figure 1.2: Development in battery technology over the past few decades showing the main electrode materials…….. (3)

Figure 2.1: Energy storage systems for large scale stationary applications…….. (12)

Figure 2.2: Basic units of an electrochemical cell…… (13)

Figure 2.3: Schematic representation of a Li-ion battery with graphite as anode and $LiCoO_2$ as the cathode……. .. (21)

Figure 2.4: Voltage versus capacity of various cathode and anode materials for rechargeable lithium-ion batteries……. (23)

Figure 2.5: Schematic energy diagram of a cell at open circuit…….. (25)

Figure 2.6: Crystal structures of Li_2MnSiO_4 polymorphs (a) orthorhombic $Pmn2_1$ phase, (b) orthorhombic Pmnb phase, (c) monoclinic $P2_1/n$ phase, revealing arrangement of MnO_4tetrahedra (purple), SiO_4tetrahedra (blue) with Li-ions (green)…… (34)

Figure 3.1: Basic operating principles of HRSEM…….. (49)

Figure 3.2: A typical cyclic voltammogram for an electrochemically reversible system… (56)

Figure 3.3: A typical square wave voltammogram consisting of a forward (anodic, Ψ_a) backward (cathodic, Ψ_c) and the net current (Ψ_{net})……. …(59)

Figure 3.4: A typical Nyquist plot ……... (61)

Figure 3.5: A typical Bode plot…… (62)

Figure 4.1: HRSEM image of pristine Li_2MnSiO_4cathode material at the scale view of 200 nm…… (64)

Figure 4.2: Elemental distribution of pristine Li_2MnSiO_4cathode material; (a), Electron image, (b), layered image, (c), (d), and (e), the corresponding x-ray maps for O, Si, and Mn..... (65)

Figure 4.3: EDX spectra of pristine Li_2MnSiO_4 nanoparticles obtained from HRSEM… .(66)

Figure 4.4: HRSEM image of novel Li_2MnSiO_4/Al_2O_3 cathode material at the scale view of 200 nm……... (67)

Figure 4.5: Elemental Distribution of novel Li_2MnSiO_4/Al_2O_3 cathode material: (a), Electron image, (b), layered image and (c), (d), (e), (f), the corresponding x-rays maps for O,Si, Mn, and Al…… (68)

Figure 4.6: EDX spectra of novel Li_2MnSiO_4/Al_2O3 cathode material obtained from HRSEM…… (69)

Figure 4.7: HRTEM micrographs of the pristine Li_2MnSiO_4 (a) and novel nanostructured Li_2MnSiO_4/Al_2O_3 (b) at the scale view of 200 nm…… (71)

Figure 4.8: EDX spectra of pristine Li_2MnSiO_4 cathode material obtained from HRTEM…… (72)

Figure 4.9: EDX spectra of novel Li_2MnSiO_4/Al_2O3 cathode material obtained from HRTEM…… (73)

Figure 4.10: FTIR spectra of Al_2O_3 nanoparticles, Pristine (Li_2MnSiO_4) and novel (Li_2MnSiO_4/Al_2O_3) nanostructured cathode materials…… (74)

Figure 4.11: XRD patterns of pristine Li_2MnSiO_4 and novel Li_2MnSiO_4/Al_2O_3 cathode materials…… (75)

Figure 4.12: ^{7}Li MAS NMR spectra of pristine Li_2MnSiO_4 (a) and the novel Li_2MnSiO_4/Al_2O_3 (b) at a MAS spinning speed of 10 kHz……. (79)

Figure 4.13: XPS full spectrum of the pristine Li_2MnSiO_4 cathode material showing the composition of the sample…… .(80

Figure 4.14: XPS full spectrum of the novel Li_2MnSiO_4/Al_2O_3 cathode material showing the composition of the sample……... ……. (81)

Figure 4.15: Fitted XPS spectra of Mn2p **(a)** Pristine $Li_2MnSiO4$, **(b)** Novel Li_2MnSiO_4/Al_2O_3 and Al2p spectrum **(c)** in the novel Li_2MnSiO_4/Al_2O_3 cathode material……..(83)

Figure 4.16: Cyclic voltammograms of the bare GCE and Li_2MnSiO_4/GCE in 1 M $LiNO_3$ at a scan rate of 10 mV/s…… (84)

Figure 4.17: Cyclic voltammograms of the pristine Li_2MnSiO_4/GCE and Novel Li_2MnSiO_4/Al_2O_3/GCE cathode materials in 1 M $LiNO_3$ at a scan rate of 10 mV/s…… .(85)

Figure 4.18: Effect of scan rate on the electrochemical cycling behavior of the novel Li_2MnSiO_4/Al_2O_3 cathode material……... (89)

Figure 4.19: Linear relationship between the peak current (I_{pa} and I_{pc}) versus the square root of the potential scan rate of the pristine Li_2MnSiO_4 cathode material…… (90)

Figure 4.20: Linear relationship between the peak current (I_{pa} and I_{pc}) versus the square root of the potential scan rate of the novel Li_2MnSiO_4/Al_2O_3 cathode material…….. .(91)

Figure 4.21: Anodic Square wave voltammogram (forward scan) of the novel Li_2MnSiO_4/Al_2O_3 in 1 M $LiNO_3$ at a scan rate of 24 mVs^{-1}…….. (92)

Figure 4.22: Cathodic Square wave voltammogram (reverse scan) of the novel Li_2MnSiO_4/Al_2O_3 in 1 M $LiNO_3$ at a scan rate of 24 mVs^{-1} …… (92

Figure 4.23: Nyquist plots for the bare GCE, the pristine Li_2MnSiO_4 and the novel Li_2MnSiO_4/Al_2O_3 cathode materials obtained at a frequency range of 0.1 Hz – 100 kHz in 1M $LiNO_3$…….(93)

Figure 4.24: Bode plot for the pristine Li_2MnSiO_4 cathode material obtained at a formal potential of 272 mV in 1M $LiNO_3$…… 94)

Figure 4.25: Bode Plot for the novel Li_2MnSiO_4/Al_2O_3 cathode material obtained at a formal potential of 266 mV in 1 M $LiNO_3$…….. (94)

Figure 4.26: The Randles equivalent circuit model……..(95)

List of Tables

Table 2.1: Most widely studied conversion reaction-based transition metal oxide anodes…… (40)

Table 2.2: Non-aqueous electrolyte systems for Li-ion batteries…….(41)

Table 4.1: Elements and their corresponding weight percentages obtained from the EDX of the pristine cathode material……(67)

Table 4.2: Elements and their corresponding weight % obtained from the EDX of the novel nanostructured cathode material…….....(72)

Table 4.3: Crystallographic parameters calculated from the XRD patterns of the pristine and novel cathode materials…….(78)

Table 4.4: Redox parameters obtained from the cyclic voltammograms of the pristine and novel cathode materials…… (88)

Table 4.5: Charge and discharge capacity values for the pristine and novel cathode materials with their capacity loss and Coulombic efficiencies……. (90)

Table 4.6: Kinetic parameters obtained from the EIS Plots of the different electrodes used……... (97)

Table 4.7: Kinetic parameters of the pristine Li_2MnSiO_4 and novel Li_2MnSiO_4/Al_2O_3 calculated from EIS data obtained at 298 K……..(99)

List of Schemes

Scheme 1.1: Research framework…….....(9)

Scheme 3.1: Experimental design for the synthesis of the pristine and novel nanostructured Li_2MnSiO_4 cathode materials……(47)

Scheme 3.2: A typical representation of Bragg's law…….. (51)

CHAPTER 1

Chapter Overview

Chapter 1 presents a brief overview of the transition towards renewable energy, highlighting the relevance of electrochemical storage systems. It further discusses in brief, advances and current research in lithium ion battery technology. The need for high performing electrode materials for extensive applications in electric vehicles, hybrid electric and smart grids is also presented, laying emphasis on cathode materials. The research impetus, aims, objectives and outline are also included.

1.0 Introduction

1.1 General Background

The global demand for new supplies of clean, secured and sustainable energy to power the planet is debatably the most scientific and technological challenge facing today's modern society. Attaining global energy demand in a sustainable way will not only promote energy efficiency and new methods of using existing carbon based fuel but also an enormous amount of carbon-neutral energy. Moreover, economic security, national and environmental security may likely be addressed by solving the energy crisis in the nearest future [1-2].

Due to economic and population growth, future energy demand is projected to rise relative to present. The technology regime of the past has been driven mainly by the combustion of fossil fuels, resulting in emissions of carbon dioxide which have been at the forefront of global climate change [1]. To switch from the traditional fossil fuels, there is a strong urge and ever growing need for renewable energy sources and reliable energy storage and conversion devices. Massive amount of research has been devoted to exploring renewable energy sources such as solar, wind, geothermal and hydrothermal energy. Conversely, these energy sources are intermittent and require suitable electrical energy storage systems.

Among various electrical storage technologies, electrochemical batteries are one of the most efficient, simple and reliable systems which convert reversely, electrical energy into chemical energy through reversible electrochemical oxidation-reduction reactions. Batteries are

presently developed to power an increasingly wide range of applications, from cars to microchips [1, 3].

According to Beck and Ruetschi, three main factors known as the three 'E'criteria, are used to establish the success of a battery system [4]. These include; energy (high energy density with respect to unit weight and volume), economics (low manufacturing and maintenance costs, long cycle life) and environment (high reliability, toxic free materials, safety, low energy consumption during manufacture and use, long service life, ease of recycling). Amongst these three factors, high energy density is the principal concern for most applications of energy storage especially for power sources in today's mobile world.

Owing to their high energy density and design flexibility, lithium-ion rechargeable batteries dominate amongst the most common rechargeable batteries such as nickel-metal hydride (Ni-MH), lead acid, redox flow and sodium-sulfur batteries [5]. It provides twice the energy density of nickel cadmium or Ni-MH, in terms of weight and volume.

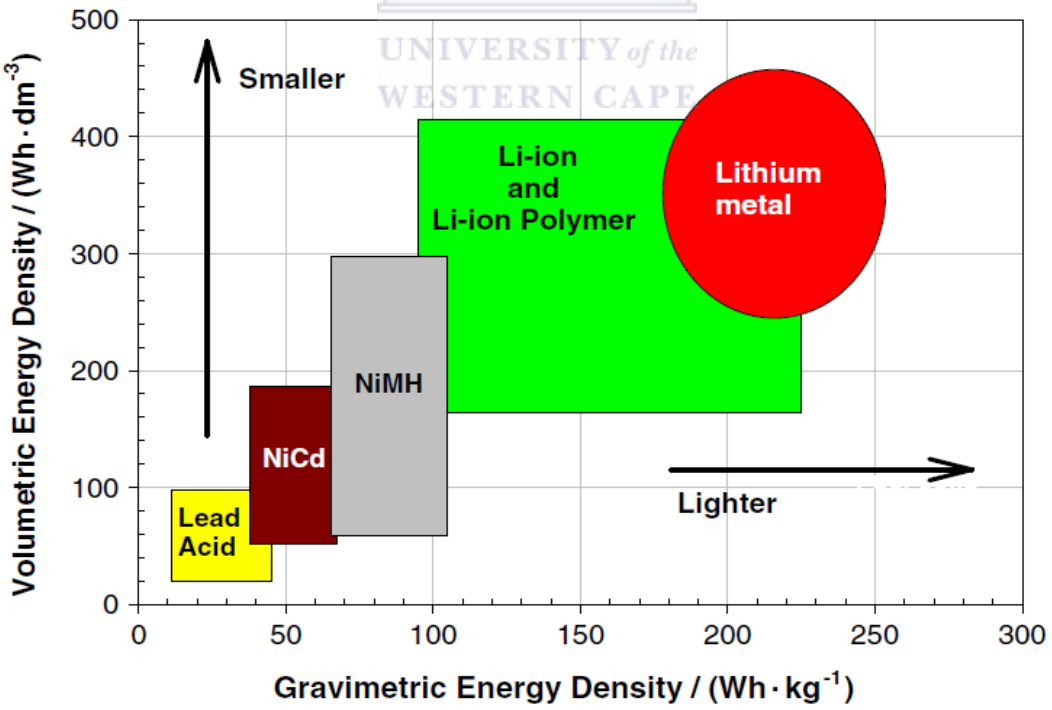

Figure 1.1: Comparison of different battery technologies in terms of volumetric and gravimetric energy density [1].

Wide-ranging research on the lithium battery started in the 1960s, inspired by the demand for greener, high efficiency and more durable batteries, and formerly focused on the non-aqueous primary batteries using lithium metal as anode. However, their use was narrowed down due to the formation of lithium dendrites which arouse serious safety concerns. The first commercial lithium ion (Li-ion) battery was developed in 1991 by SONY Corporation [5], and with gradual developments in the technology over the past few decades; Li-ion batteries are currently the prevailing portable power source. Current research is targeted towards extensive applications in hybrid electric vehicles, electric vehicles and smart grids.

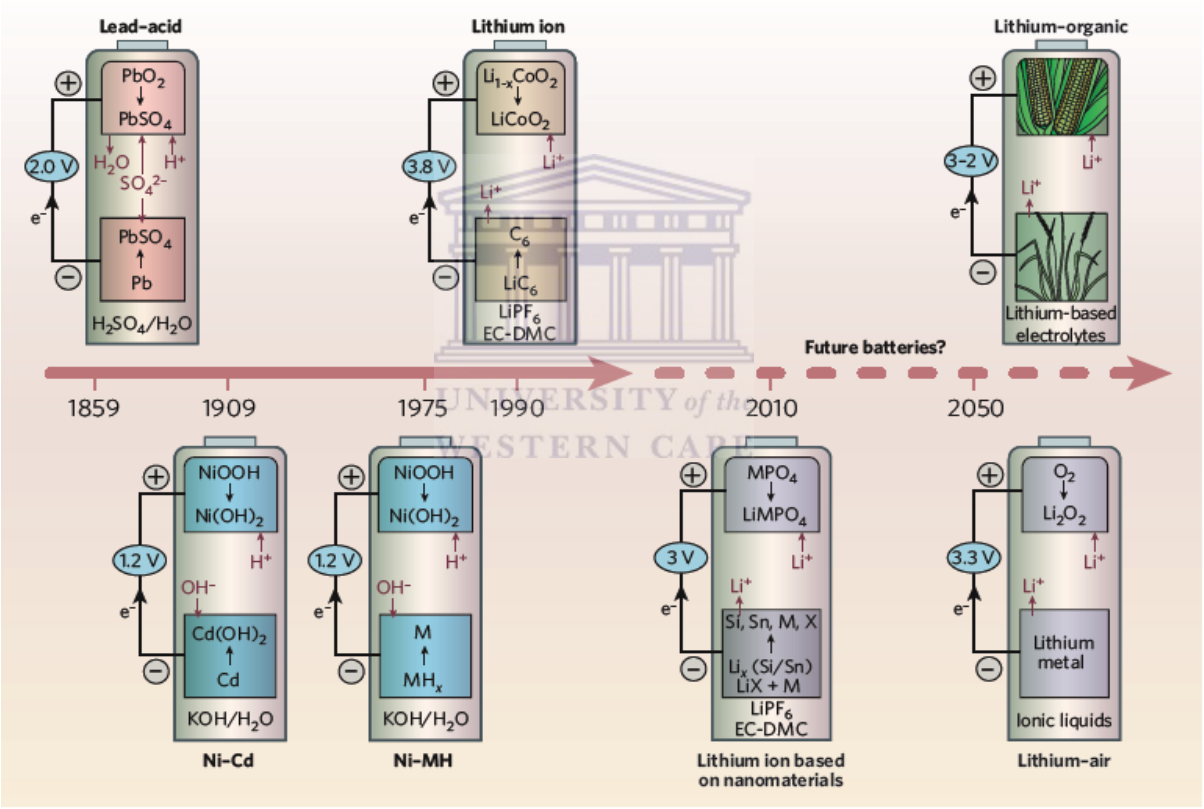

Figure 1.2: Development in battery technology over the past few decades showing the main electrode materials [1].

Even though great progress is currently being made, it is true to say that we still lack batteries with the essential performance to overcome the challenge. Present large scale battery technologies still fall short in terms of energy and power density, cyclability, cost and most

importantly – safety. The new 3G and 4G technologies used in portable communication devices will lead to even higher demand for high rate batteries. Ideal batteries in this case will require the following qualities; long life, light weight, small size, high energy density, safety, environmental affability, low cost and global distribution. But none of the current rechargeable batteries satisfy the above requirements since most of them deliver capacities and energy density far below their theoretical values [6]. Significant breakthroughs are therefore needed especially as concerning the active electrode materials since the practical energy and power density, safety, cycling life and cost of Li-ion batteries are determined specifically by the composition, morphology and the microstructure of the electrode materials used [7]. Up to now, three types of cathode materials have been explored intensively; layered transition metal oxides ($LiCoO_2$), manganese-based spinels ($LiMnO_2$ and $LiMn_2O_4$) and polyanion-type cathode materials (phosphates - $LiMPO_4$; M = Fe, Mn and orthosilicates - Li_2MSiO_4; M = Mn, Fe, Co, Ni). $LiCoO_2$ is the presently leading cathode material with an energy density of about 150 Wh Kg^{-1} [8]. Conversely, layered transition metal oxide cathode materials suffer from some limitations such as oxygen evolution at high charging potential which poses serious safety concerns for practical applications; low energy density and high cost. Thus layered transition metal oxide cathode materials are restricted to applications in small scale batteries for portable electronic devices [9-10]. Mn-based spinel such as $LiMn_2O_4$ has several advantages such as low cost, high thermal stability and environmental friendliness. Thus Mn- based spinels cathode materials are being considered as candidates for high rate applications in EV and HEV. However, they suffer from a poor cycling behaviour caused by the Jahn-Teller distortion resulting from the disproportionation of Mn^{3+} ions [11].

With the continuous search for high rate electrode materials for lithium ion batteries, polyanion-type electrode materials (phosphates and orthosilicates) were proposed in 2002 as possible substitutes for layered transition metal oxide cathodes. The possibility of enhanced safety of these compounds compared to the oxides, and the opportunity of using non-toxic and cheap metals such as iron to replace cobalt gave the impetus for this research. Furthermore, the oxygen atoms in the polyanionic lattice are held by strong covalent bonds, thereby reducing the risk for oxygen release during the charged state and further improving their safety characteristics. Their electrochemical properties could also be tuned by changing the nature of the X atom in the XO_4 polyanions owing to their different electronegativities [12]. $LiFePO_4$ has been extensively investigated in the phosphate class due to its high specific capacity, excellent

structural stability, environmental benignness and abundance of iron. Even though $LiFePO_4$ demonstrates high potential for high power tool applications, its low electronic conductivity and lithium ion diffusivity limits its high rate applications [13].

Amongst the orthosilicate family, Li_2MnSiO_4 is the cathode material which shows great potential to deliver high capacity due to its numerous advantages such as: high theoretical capacity above 330 $mAhg^{-1}$ upon complete extraction of 2 mols of Li^+ ions per formula unit; improved safety; high thermal stability via strong Si-O bonds; environmental friendliness and low cost [14]. As for the Fe, Co and Ni counterparts, the voltage for extracting the second electron lies above the voltage stability window for common electrolytes, thus only 1 mol of Li^+ ion is perhaps extracted [15]. However, Li_2MnSiO_4 also has some drawbacks like: Structural instability linked with the Jahn-Teller distortion at the Mn site and intrinsic low electronic conductivity resulting in large capacity fading and poor rate capability which limits its practical application. To circumvent these challenges, several solution-based synthetic routes such as sol-gel, solvothermal, hydrothermal synthesis, surface carbon coating and particle size reduction approaches to produce nanoparticles/ nanocomposite Li_2MnSiO_4/C have been employed. Nevertheless, the electrochemical performance of the composite cathode material has been improved to some extent, though the reported initial reversible capacities and cycling life vary between 100-210 $mAhg^{-1}$ [16-19].

Surface modification has been proven to be an effective approach for enhancing the electrochemical properties of various electrode materials, acting as a protective layer to prevent direct contact of the active core material with the electrolyte thereby restricting the dissolution of the active material and stabilizing the crystal structure. Metal oxides such as Al_2O_3, ZrO_2, MgO, SnO_2 and TiO_2 have effectively been applied to modify electrode materials such as $LiCoO_2$, $LiMn_2O_4$, $LiFePO_4$ and LiV_3O_8, and have been found to enhance their electrochemical performance and provide facile transport of Li^+ ions [20-22].

The design of nanostructured electrode materials is very crucial for next generation lithium ion batteries so as to provide large surface area between the electrode and electrolyte thereby increasing the number of reactive sites for electrode reactions. Moreover, nanostructured electrode materials offer the possibility of enhanced flexibility for surface modification, improved surface transport of electro-active species by reducing the diffusion pathway and decreased surface compliance against undesired electrode-electrolyte reactions [7]. Hence

adoption of nanotechnology in Li-ion battery systems further enables reduction in the electrode polarization loss, improves the power density, energy efficiency and practical energy density.

In line with the above facts, this project will involve the design of nanostructured Li_2MnSiO_4 via the hydrothermal synthetic route by carefully tuning the reaction conditions in order to enhance the energy density and inherent low electronic conductivity of the cathode material. To stabilize the surface of the active material/electrolyte interface and reduce Mn dissolution during cycling, the nanostructured cathode material will be coated with a thin film of Al_2O_3 due to its stabilizing effect through a rapid wet chemical process and subsequent calcination steps.

1.2 Problem statement

Li_2MnSiO_4 is attractive in terms of environmental sustainability because of the non-toxicity, low-cost and abundance of its constituent elements. It also has the advantage of being able to intercalate/de-intercalate 2 mols of lithium ion per formula unit, which translates into a theoretical specific capacity of 334 $mAhg^{-1}$, and is higher than that obtained from other competing cathodes. However, its electrochemical activity is impeded by very low intrinsic electronic conductivity at ~6 x 10^{-16} Scm^{-1} which is about two orders of magnitude lower than its iron analogue. This drawback is attributed to the Jahn-Teller distortion associated with the Mn^{3+} which causes a big change in the lattice parameters and the crystalline structure. In order to overcome this disadvantage, the proposed study involves the manufacture of nanostructured Li_2MnSiO_4 and introducing a stabilizer by coating with aluminium oxide nanofilm, which will further stabilize phase transitions and reduce manganese dissolution during cycling. On the other hand, the nanostructures offer increased surface area and decreased diffusion distance for charge transfer [7].

1.3 Rationale and motivation for the research

With the increased awareness for global warming and the high demand for renewable energy sources, electrical energy storage and conversion systems have become very crucial to replace the traditional fossil fuels. Li-ion batteries are at the forefront of the electronics market, providing high energy densities, long cycle life and high voltage with no memory effect when compared with other electrochemical storage devices. However, the adoption of this

technology for large scale application is limited by material challenges. In order to realize the next generation rechargeable lithium-ion batteries for applications in HEV and EV, there is need for the continuous expansion of lithium ion battery chemistry and design of new intercalation materials with better performance characteristics, as well as enhancement of the properties of the existing ones. Layered transition metal oxides and Mn-based spinels such as $LiMO_2$, M= Ni, Mn, Co and $LiMn_2O_4$ have been used. However, the safety concern arising from oxygen evolution at high potential could result in heat production and fire, and inherent chemical stability of highly oxidised species like Co^{4+} and Ni^{4+} limits their usable capacities. Polyanion compounds such as phosphates have also been investigated as cathode materials and the olivine type $LiFePO_4$ has attracted more attention as iron is inexpensive and environmentally benign, with the covalently bonded PO_4 groups offering excellent stability. With these advantages, it still suffers from low electronic conductivity and poor lithium ion diffusivity. Possible strategies have been made to overcome this problem including carbon coating, particle size reduction through various synthetic methods. Though with a lower voltage of around 3.4 V and theoretical capacity of 170 $mAhg^{-1}$, the energy density of $LiFePO_4$ is lower than that of the transition metal oxide cathodes.

The continuous development of Li-ion battery cathodes since the 1990's has been motivated by the need to maintain high discharge voltage to maximize the energy density. Expanding the usable range of lithium intercalation /deintercalation to maximize capacity and to enhance safety by reducing the reactivity of the electrode materials at charged state; while striving to use non-toxic and inexpensive materials to eliminate environmental impact and cost has also been part of this call [15].The orthosilicate family of polyanionic electrode materials (Li_2MSiO_4; M= Mn, Fe and Co) which were proposed at almost the same time as the phosphates show great potential of fulfilling the above demands. This group of materials are highly attractive, as silicon is among the most abundant and low cost elements coupled with the high stability of the covalently bonded SiO_4 group. An obvious step in the search for further active intercalation material from this family is to find a material that would allow the extraction of the two lithium ions. This makes Li_2MnSiO_4 an attractive target because in addition to the advantages offered by the orthosilicates, its constituent elements are non-toxic and is capable of achieving the desired insertion/ extraction of two lithium ions per formula unit, unlike the other analogues whose potentials are out of the voltage stability window for current electrolytes.

1.4 Research aims and objectives

The aim of this project is to design a nanostructured high energy density cathode material with improved electrochemical or battery performance, which may possibly be applied in high power rate applications. With this aim, the following objectives are required to be achieved.

- Preparation of pristine and modified lithium manganese silicate (Li_2MnSiO_4) cathode materials and optimization of parameters to obtain the desired nanostructure.
- Surface, elemental and particle size analysis of the pristine and composite Li_2MnSiO_4 materials by High Resolution Transmission Electron Microscopy (HRTEM), High Resolution Scanning Electron Microscopy (HRSEM), Energy Dispersive X-ray (EDX) and X-ray photoelectron spectroscopy (XPS).
- Crystallographic and functional group analysis of the pristine and modified cathode materials by X-ray Diffraction (XRD), Fourier Transform Infra-Red Spectroscopy (FTIR) and Solid-State Nuclear Magnetic Resonance Spectroscopy (SS-NMR).
- Electrochemical characterisation of pristine and composite Li_2MnSiO_4 materials to verify material dynamics at the electrode surface using Cyclic, Square-Wave Voltammetry (CV, SWV) and Electrochemical Impedance Spectroscopy (EIS).
- Fabrication of Li-ion coin cells using pristine and composite Li_2MnSiO_4 cathode materials to determine galvanostatic charge/discharge capacity profiles at different C-rates.

1.5 Research framework

According to the research objectives and experimental procedures, the research framework was structured as follows;

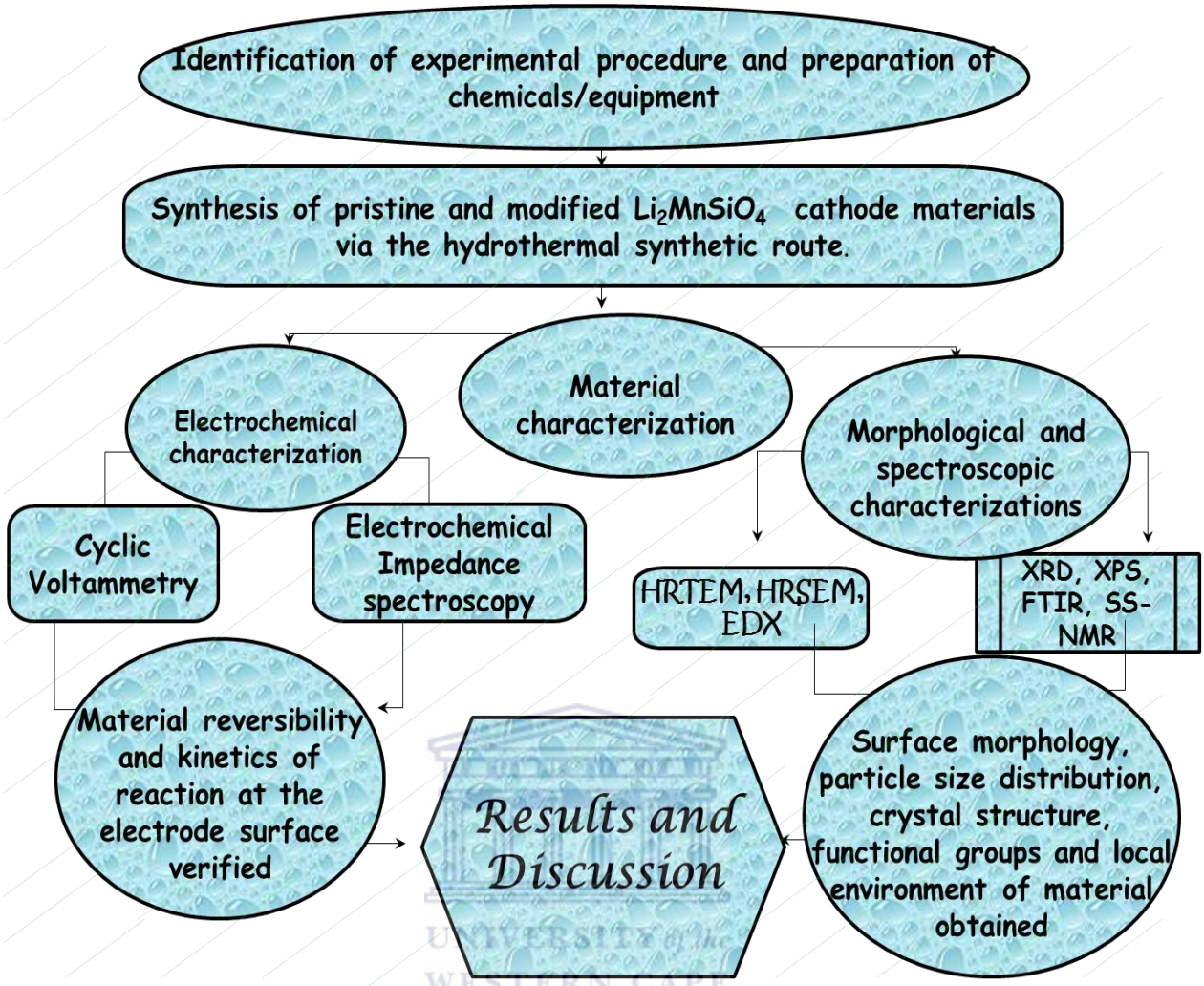

Scheme 1.1: Research framework.

1.6 Thesis outline

This study focuses on the synthesis of nanostructured Li_2MnSiO_4 and novel modified Li_2MnSiO_4/Al_2O_3 cathode materials with improved electrochemical performance and high energy/power density for rechargeable Li-ion battery applications. The success of this goal depends on an understanding of how the component materials influence device performance as well as an understanding of material synthesis and processing to optimize material quality and eventually improve device performance. Therefore, the physical features, crystal structures and electrochemical performance of the as-prepared materials will be investigated systematically, and the results and key findings presented as outlined below.

Chapter 1 presents a brief introduction to the background knowledge on the transition towards renewable energy, highlighting the relevance of electrochemical storage systems as aforementioned. It discusses in brief, advances and current research in lithium ion battery technology. The need for high performing electrode materials for extensive applications in electric vehicles, hybrid electric and smart grids is also presented, with particular emphasis on cathode materials. The research impetus, aims, objectives and thesis outline are also outlined.

Chapter 2 provides a comprehensive review of electrochemical energy storage systems and fundamentals of Li-ion batteries. Various battery systems for energy storage applications are discussed laying particular emphasis on lithium-ion batteries. Basic concepts as well as materials in lithium-ion batteries are also outlined. The significance of nanosized materials on the performance of lithium-ion batteries is discussed as well. The literature presented in this chapter will be of critical significance since it will shed more light on the research proper.

Chapter 3 starts by listing the various chemicals used in this study. The experimental methods and procedures used during synthesis are explained in detail. A brief background on the characterization techniques and instrumentation employed in the study such as HRSEM, HRTEM, FTIR, SS-NMR, XRD, XPS, CV, SWV and EIS is presented.

Chapter 4 discusses the outcomes of the morphological, spectroscopic and electrochemical interrogations conducted on the pristine and novel cathode materials and stating their significance.

Chapter 5 summarizes the various achievements of the study and outlook for possible future improvements, closely followed by references.

CHAPTER 2

Chapter Overview

As previously mentioned in Chapter one, this chapter presents a comprehensive review of the fundamentals of electrochemical energy storage and battery energy storage systems highlighting the potential market for Li-ion batteries. Elementary concepts such as potential, theoretical capacity and C-rates in Li-ion batteries as well as materials (cathodes, anodes and electrolytes) in Li-ion batteries are discussed. The relevance of nanomaterials on the performance of Li-ion batteries is also presented. The literature presented in this chapter will be of critical significance since it will shed more light on the research work.

2.0 Literature Review

2.1 Electrochemical energy Storage and fundamental aspects

Energy storage and power control are increasingly gaining special attention as many countries are focusing on electricity generation from renewable energy sources [23]. Harvesting green energy from renewable energy sources and storing it in electrical energy systems for power supply will enable a greener and less energy intensive transportation industry and future smart city power systems. Although the demand for energy storage will be far greater in future, the bondage of ensuring power quality is already on us as evidenced by recent power outages. For instance; it is estimated that poor power quality in the US economy results in productivity losses about 400 billion dollars a year [8].

Various energy storage systems such as electrochemical, kinetic, thermal, potential, electrical, magnetic and thermo-chemical energy storage systems as illustrated on Figure 2.1 below have been investigated and are described based on how the electrical energy is stored. Among them, electrochemical energy storage systems such as batteries are more appealing as they are more efficient when compared with potential energy storage systems such as commercial pumped hydroelectric storage (PHES) and compressed air energy storage (CAES) which have been conventionally considered due to their high power storage up to gigga watt levels for bulk

storage. Batteries can as well be situated anywhere, without geographical concerns, which allows them to be installed near residential areas. Their sizes enable applications ranging from few KWh to numerous MWh, concurrently for power and

energy management applications.

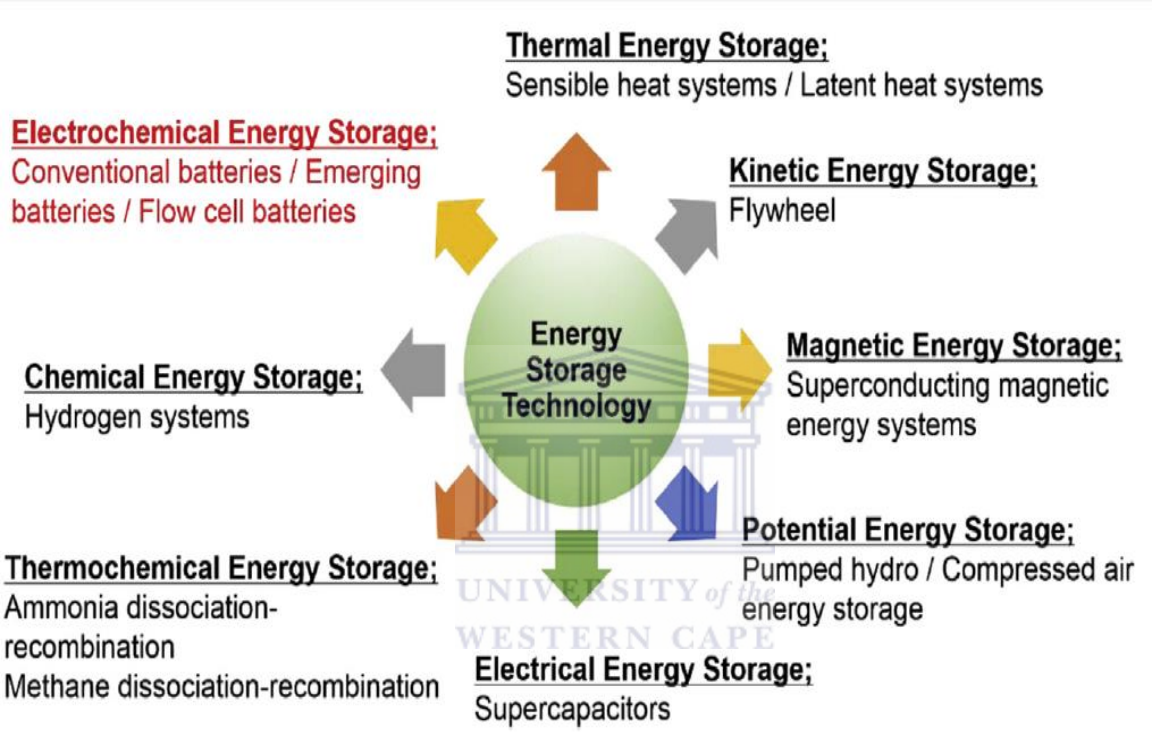

Figure 2.1: Energy storage systems for large scale stationary applications [8].

The basic unit of an electrochemical storage system is known as a cell. The cells are connected either in series or in parallel to obtain a high voltage or capacity, and in both cases; the resultant ensemble is called a battery [24]. An electrochemical cell (Figure 2.2 below), consists of a cathode, anode and the electrolyte or ionic conductor. In the electrochemical cell, when a current (I) in amperes passes through the external circuit for a certain length of time (t) in seconds, the quantity of charge (Q) in coulombs transferred is equal to $I\,t$. The applied charge consumes moles (N_m) of reactants O or R given by:

$$N_m = \frac{It}{n\,N_A\,e} = \frac{It}{nF} \tag{2.1}$$

Where n = number of electrons given or accepted by O or R, N_A = Avogadro's constant, e = charge on an electron, and F = Faraday constant [8].

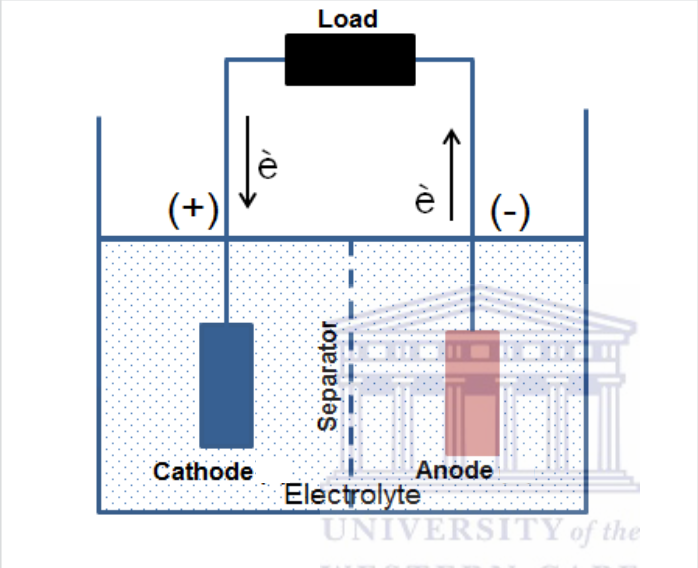

Figure 2.2: Basic units of an electrochemical cell.

At the electrode/ electrolyte interface, oxidation or reduction occurs, caused by electron transfer. The amount of chemical reactions caused by the flow of current is proportional to the amount of electricity passed. This charge transfer process is controlled by the Faraday's law while the rate of current flow is controlled by the Butler-Volmer formula: Equation (2.2) below.

$$i = i_o \exp(\alpha F\eta / RT) - \exp\frac{(1-\alpha)F\eta}{RT} \tag{2.2}$$

where i = the exchange current, α = the transfer coefficient, η = polarization, F = Faraday constant, R = gas constant, and T = temperature [8].

During the discharge process, the anode (O) is oxidized and electrons are delivered to the external circuit. The cathode (R) on the other hand, accepts electrons from the external circuit and is reduced, as illustrated by the two half-cell reactions.

Anode: $O \longrightarrow O^{n+} + ne'$ (2.3a)

Cathode: $R + ne' \longrightarrow R^{n-}$ (2.3b)

Overall cell reaction: $O + R \longrightarrow O^{n+} + R^{n-}$ (2.3)

The separator acts as a physical barrier to prevent electrical shorting between the anode and cathode while the electrolyte provides a medium for ionic transport.

2.2 Battery systems for energy storage applications

Batteries consist of a stack of electrochemical cells where-in chemical energy is converted to electrical energy and vice versa, to power a variety of applications. They can either be primary (non-rechargeable due to non-reversibility of electrode reactions) or secondary batteries (rechargeable and reusable due to reversibility of electrode reactions) [25]. The required battery voltages as well as current levels are obtained by electrically connecting the cells in series and parallel as aforementioned. Batteries are rated in terms of their energy and power capabilities, which are not independent but pre-set during battery design [26]. Other significant features of a battery include; efficiency, operating temperature, self-discharge (rate of discharge in cases where a battery is stored in a shelf and it cannot retain its electrical capacity), depth of discharge (extent of discharge since batteries are generally not completely discharged) and energy density [26]. Several types of batteries are being developed for large scale energy storage applications and are available commercially while others are still in the experimental stage.

2.2.1 Lead-acid batteries

The lead-acid battery was developed back in the 18th century (1859) by Gaston Planté and it has been modified for use in various applications, ranging from starting engines in electric vehicles to electrical storage in renewable energy systems [8]. This system consists of a positive electrode of lead dioxide (PbO_2) and a negative electrode of high surface area metallic lead (Pb), separated by a micro-porous material and immersed in an aqueous sulphuric acid electrolyte [8, 26]. During its reversible charging and discharging processes, it utilizes the electrode reactions of Pb oxidation (2.4a) and PbO_2 reduction (2.4b), resulting in the formation of lead (II) sulphate ($PbSO_4$) at both electrodes. The electrode reactions are as follows:

At the anode; $Pb \rightarrow Pb^{2+} + 2e'$ (2.4a)

At the cathode; $Pb^{4+} + 2e' \rightarrow Pb^{2+}$ (2.4b)

Combining the above half reactions, the overall cell reaction goes thus

$$Pb + PbO_2 + 2H_2SO_4 \rightleftharpoons 2PbSO_4 + 2H_2O \quad (2.4)$$

A voltage of 2.1 V is provided by the overall reaction and an open circuit voltage of 1.75 V on moderate discharging per cell. The open circuit voltage varies with the concentration of the electrolyte indicating that the state of charge in a lead-acid battery could be determined by measuring the relative density of sulphuric acid [8].

Lead-acid batteries have been used in a variety of electrical power applications due to their ease of manufacture, moderate power supply range (from kWs to a few tens of mWs), relative low cost, moderate electrical efficiency and life time. Moreover, the cell components can be recycled efficiently from used batteries. But the cycle life of the lead-acid battery can be restricted by continues accumulation of lead sulphate on the surface of the negative plate during high discharge rate. This reduces the effective surface area of the plates for electrochemical reactions, thus resulting in poor rate performance. Subsequent charging of the cell results in

hydrogen evolution, which also promotes poor cycle efficiency and an explosion hazard [8, 27].

2.2.2 Sodium-sulfur batteries

Sodium-sulfur (Na-S) batteries are rechargeable high temperature molten metal batteries consisting of molten sulfur as the positive electrode, molten sodium as the negative electrode and beta-alumina as a solid electrolyte and separator [28]. Since their introduction in the 1970s, Na-S batteries have been considered as promising candidates for large scale electrical energy storage applications due to the low redox potential and abundance of sodium, high energy density, high efficiency of the charge/discharge processes and cycling flexibility [8, 28].

At the negative electrode during the discharge process, sodium is oxidized given Na^+ ions which move through the solid electrolyte to the positive electrode, reacting with sulfur to form disodium pentasulfide (Na_2S_5). The Na_2S_5 separates from the rest of the sulfur in the cathode to form a two-phase liquid mixture which is slowly converted to a single-phase sodium polysulfide (Na_2S_{5-x}) until the rest of the sulfur is completely consumed [8]. These reactions are reversible during the charge process, yielding the following cell reactions.

At the anode; $2Na \rightleftharpoons 2Na^+ + 2e^-$ (2.5a)

At the cathode; $xS + 2Na^+ + 2e^- \rightleftharpoons Na_2S_x$ (2.5b)

Overall cell reaction; $2Na + xS \rightleftharpoons Na_2S_x$ (2.5)

Na-S batteries require high operating temperatures of 300 – 350 ºC to maintain sodium and sulfur in the molten state and also to ensure efficient sodium transportation through the solid electrolyte. This high temperature aspect limits their possible applications and they are better suited for large scale, non-mobile technologies such as grid energy storage [28]. Another issue with Na-S batteries is the highly corrosive and electrical insulating nature of discharged products such as sodium polysulfide. Hence an anti-corrosive current collector and a carbon source material as electronic conductor are needed to properly mix with the discharge products to enhance electron transport [8].

2.2.3 Flow batteries

Flow batteries are rechargeable batteries which consist of two electrolyte reservoirs whereby, the electrolytes circulate through an electrochemical cell. The energy density of the system can be determined from the volume of the electrolyte stored while the power density essentially dependents on the cathodic and anodic reactions [23]. The vanadium redox battery, the zinc bromine and polysulfide bromide batteries are the three main designs of flow batteries. The vanadium redox and zinc bromide batteries will be discussed below.

2.2.3.1 Vanadium redox battery

The vanadium redox (reduction-oxidation) battery (VRB) is a type of flow battery which uses vanadium ions in different oxidation states to store chemical energy. The VRB makes use of the ability of vanadium to exist in four different oxidation states in solution and utilizes this aspect to make a battery that has just one electro-active specie, instead of two [28]. The VRB system consist of two external reservoirs, containing two electro-active species; V^{4+}/V^{5+} as the positive electrode and V^{2+}/V^{3+} as the negative electrode, with two stacked electrodes [8]. The two segments are separated by an ion-exchange membrane and have a pumped circulatory system. The electrochemical reactions which occur are represented below.

At the negative electrode; $V^{2+} \rightleftharpoons V^{3+} + e^{-}$ (2.6a)

At the positive electrode; $VO_2^{+} + 2H^{+} + e^{-} \rightleftharpoons VO^{2+} + H_2O$ (2.6b)

Overall cell reaction; $VO_2^{+} + 2H^{+} + V^{2+} \rightleftharpoons VO^{2+} + H_2O + V^{3+}$ (2.6)

The VRB is relatively a clean technology with high availability and long cycle life. It offers almost unlimited capacity by simply using larger and larger tanks, and can be left discharged for a long duration of time with no detrimental effects. Where there is no power source for recharging it, it can simply be recharged by replacing the electrolyte [28]. The main drawbacks of the VRB are its low energy density and the complexity of the system in comparison with

standard storage batteries [28]. Their almost unlimited capacities make them suitable for use in large scale power storage applications such as assisting to level out the production of highly variable generation sources like wind and solar power, or helping generators cope with high power demand. The possibility of being discharged for longer periods of time with no ill effects also makes them useful for applications where batteries are required to be stored for long periods of time with little or no maintenance while maintaining a steady state. This has led to their use in some military electronics [28].

2.2.3.2 *Zinc bromine battery*

The zinc bromine battery is a type of hybrid flow battery which stores its electrolyte in two tanks, one tank is used to store electrolyte for the positive electrode and the other for the negative electrode [28]. During the charge/discharge process, the electrolytes are pumped through a reactor stack and back into the tanks. The most commonly used aqueous electrolyte is composed of zinc bromide dissolve in water. During charging, zinc is deposited unto the negative electrode surfaces of the cell stacks from the electrolyte and bromide is converted to bromine at the positive electrode surface of the cell stack. These processes are reversed during discharge and are represented as follows [28-29]:

At the negative electrode; $Zn \rightleftharpoons Zn^{2+} + 2e^{-}$ (2.7a)

At the positive electrode; $Br_2 + 2e^{-} \rightleftharpoons 2Br^{-}$ (2.7b)

Overall cell reaction; $Zn + Br_2 \rightleftharpoons ZnBr_2$ (2.7)

The zinc bromine battery is referred to as an electroplating machine. Metallic zinc deposited on the negative electrode during charging dissolves in the electrolyte and is ready to be plated again during the next charging cycle. The battery can be left fully discharged for long periods of time without damage. The important features of the zinc bromine battery include; high energy density relative to the lead-acid batteries, 100 % depth of discharge regularly, no shell life limitations and the capacity to store energy from any electricity generating source [28]. A major drawback of the zinc bromine battery is the high capital and running cost associated with

the operation of the complex system. That is, a chemical plant involving pumped systems and flow control with external storage [23].

2.2.4 Nickel-Cadmium batteries

Nickel-cadmium (Ni-Cd) secondary batteries are the most recognized alkaline secondary batteries with several cell designs, robust reliability and wide range of sizes. They can be operated over a wide temperature range and at relatively discharge rates [30]. Ni-Cd batteries consist of nickel oxyhydroxide as the positive electrode, metallic cadmium as the negative electrode, a micro-porous polypropylene plastic membrane as the separator, and an alkaline electrolyte (potassium hydroxide). Ni-Cd batteries usually contain a metal case with a sealing plate and a self-sealing safety valve, which encloses the electrodes kept apart by the micro-porous ion-permeable separator [28, 31]. During discharge, nickel oxyhydroxide combines with water and produces nickel hydroxide and a free hydroxide ion at the positive electrode whereas, cadmium hydroxide is produced at the negative electrode [28]. The reverse process occurs during charging. However, oxygen might be produced at the positive electrode and hydrogen at the negative electrode during charging; requiring venting and water addition [28]. The chemical reactions occur according to the equations below:

At the negative electrode; $Cd + 2OH^- \rightleftharpoons Cd(OH)_2 + 2e^-$ (2.7a)

At the positive electrode; $2NiOOH + 2H_2O + 2e^- \rightleftharpoons 2Ni(OH)_2 + 2OH^-$ (2.7b)

Overall cell reaction; $2NiO(OH) + Cd + 2H_2O \rightleftharpoons 2Ni(OH)_2 + Cd(OH)_2$ (2.7)

Two main types of Ni-Cd battery designs are commercially available; the sealed and the vented battery designs. The sealed battery design is the most common rechargeable Ni-Cd battery used in commercially electronic devices such as remote controls and lamps where light weight, portability and rechargeable power are important. No gases are released in these batteries except a fault occurs [28]. The vented Ni-Cd battery has the same operating principle as the sealed battery design but releases gases upon rapid discharge or overcharging. Vented Ni-Cd batteries are used in aircraft and diesel engine starters where large energy per weight and

volume are desired [28]. Ni-Cd batteries are best suited for providing standby power in harsh conditions and have recently become popular as storage for solar generation since they can withstand high temperatures [28].The major drawbacks of Ni-Cd batteries are its high cost owing to the expensive manufacturing process, cadmium toxicity leading to environmental safety concerns associated with the disposal of Ni-Cd batteries, and the low cycle life caused by the hydrolysis of the nylon-based separator in the KOH electrolyte, which seriously degrades the battery life [30-31].

2.2.5 Nickel-metal hydride batteries

The nickel-metal hydride batteries (Ni-MH) are alkaline storage batteries similar in many facets as the Ni-Cd batteries. Environmental concerns regarding the toxicity of cadmium and the safe disposal of Ni-Cd batteries have hastened the commercialization of Ni-MH batteries [32]. Electrode processes in Ni-MH batteries are related to those of the Ni-Cd batteries except for that, the Ni-MH use only hydrogen-absorbing negative electrode instead of the cadmium negative electrode as in Equation (2.7a) above [33]. These processes are as follows:

At the anode; $H_2 + 2OH^- \rightleftharpoons 2H_2O + 2e^-$ (2.8a)

At the Cathode; $2NiOOH + 2H_2O + 2e^- \rightleftharpoons 2Ni(OH)_2 + 2OH^-$ (2.8b)

Cell Reaction; $2NiOOH + H_2 \rightleftharpoons 2Ni(OH)_2$ (2.8)

The Ni-MH batteries have the advantage of being able to replace the Ni-Cd batteries practically without any alternations in the power systems for many electronic devices since they are very similar in physical make-up and almost the same charge/discharge voltage profiles. Even though the charging system for these batteries is virtually the same, there is no need to minimize the overcharge of Ni-MH batteries as opposed to the Ni-Cd batteries. Ni-MH offer more energy per unit volume or weight than the Ni-Cd or lead acid batteries are environmentally friendly, and at present, they are being considered among the preferred rechargeable batteries for the future in the field of portable energy devices [32].

2.2.6 Lithium-ion batteries

The lithium-ion (Li-ion) battery is seen as the power source of preference for sustainable transportation systems, since they store higher energy per unit weight or volume compared to other rechargeable battery systems [34-35]. They are light, compact and work with a specific energy in the range of 100 $WhKg^{-1}$to 150 $WhKg^{-1}$ [34]. Li-ion batteries use lithium intercalation compounds as the anode and cathode materials. In their most conventional structure, they contain graphite as the anode, layered transition metal oxides as the cathodes ($LiMO_2$, M= Co, Mn), and an electrolyte consisting of a solution of lithium salt ($LiPF_6$) in a mixed organic solvent (ethylene carbonate-dimethyl carbonate).

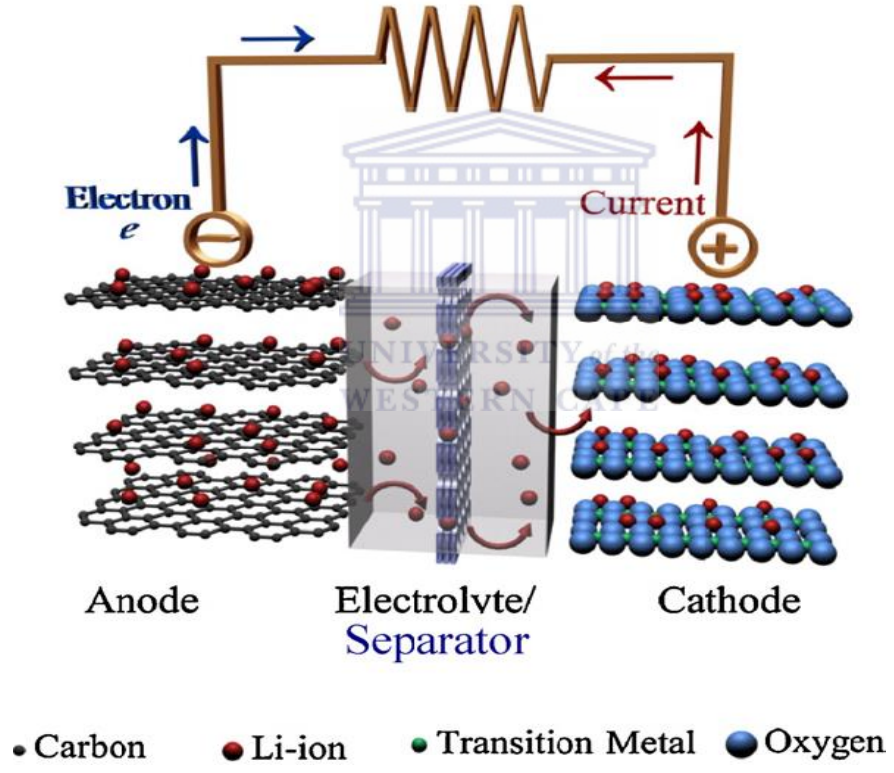

Figure 2.3: Schematic representation of a Li-ion battery with graphite as anode and $LiCoO_2$ as the cathode [7].

The operating principle of Li-ion batteries is based on the shuttling of lithium ions between two insertion host electrodes (anode and cathode) during the charge-discharge process, resulting in a so called "rocking chair" battery [35]. During the discharge process, Li-ions move from the anode through the electrolyte and are inserted into the layered oxide, with an external

flow of electrons from the anode to the cathode, generating electrical power. During charging, Li-ions and electrons are both driven back by an external voltage in the opposite direction, resulting in the storage of electrical energy as chemical energy in the battery [7].

At the anode: $Li_xC_6 \rightleftharpoons 6C + xLi^+ + xe^-$ (2.9a)

At the cathode: $Li_{1-x}CoO_2 + xLi^+ + xe^- \rightleftharpoons LiCoO_2$ (2.9b)

Cell reaction: $Li_{1-x}CoO_2 + Li_xC_6 \rightleftharpoons LiCoO_2 + 6C$ (2.9)

Lithium-ion batteries have the following advantageous qualities;

- High specific energy and power density
- High voltage scaling up to 4 V depending on the active materials used
- Wide operating temperature ranging from -40 to 70 °C
- Long cycle life
- High Coulombic and energy efficiency
- Long shelf life, can be stored for long periods with no memory effects
- High rate and rapid charge capability

Even though Li-ion batteries possess many appealing features, there are some drawbacks which are needed to be addressed in order to achieve optimum performance with Li-ion batteries. These drawbacks include:

- Degrading at high temperatures
- Venting and possible thermal runaway when crushed
- Capacity loss and possible thermal runaway when overcharged
- Moderate initial cost and extra cost for recycling

2.3 Basic Concepts in Lithium-ion batteries

The following terms are frequently used in the course of this study to evaluate the properties and performance of lithium-ion batteries.

2.3.1 Potential

The theoretical potential of a cell is dependent on the active materials present in the cell. It can be obtained from free-energy data or standard electrode potentials. Figure 2.4 below summarises the potential versus capacity of various electrode materials for lithium-ion batteries.

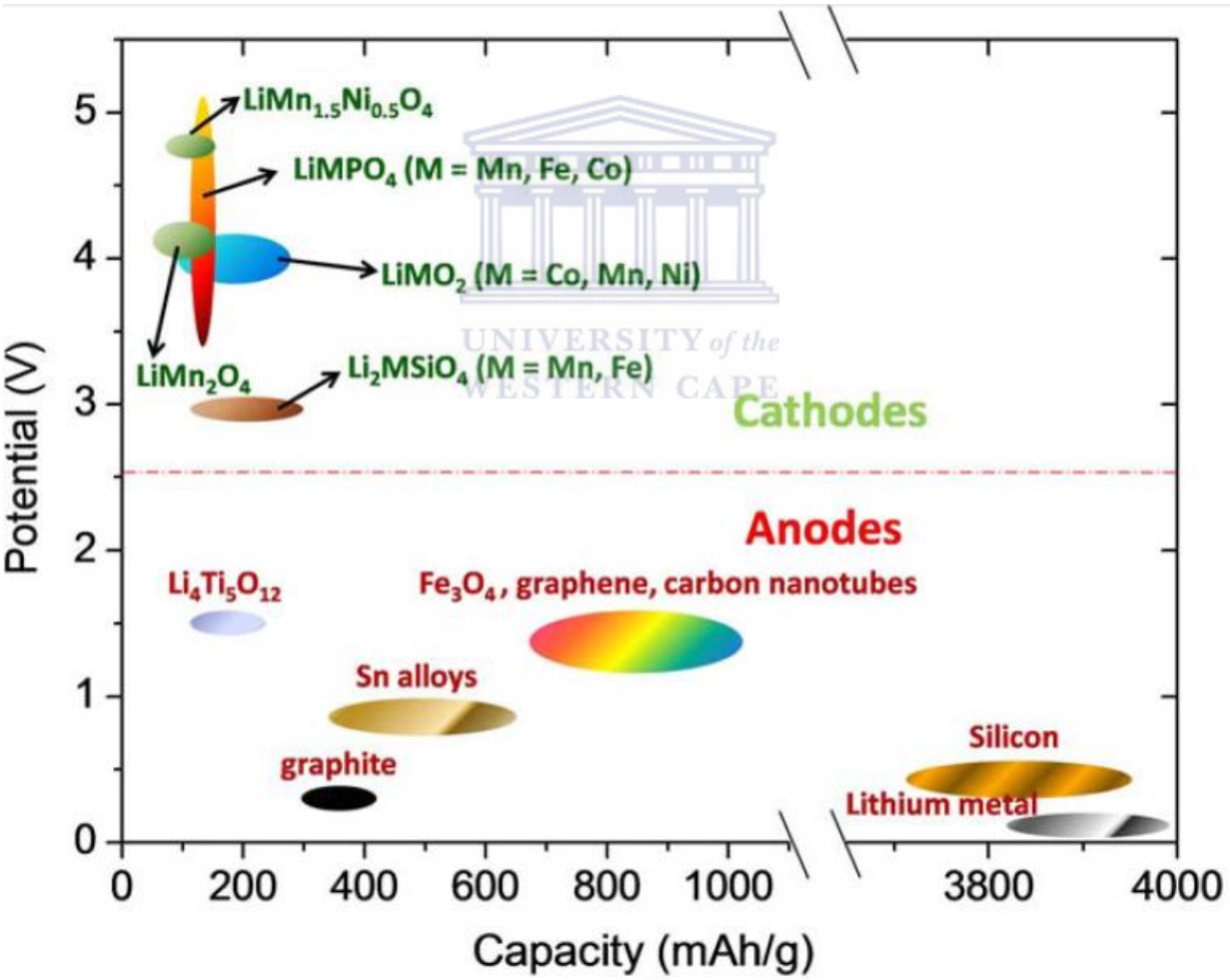

Figure 2.4: Voltage versus capacity of various cathode and anode materials for rechargeable lithium-ion batteries [36].

The development of high energy density batteries requires the use of high capacity electrode materials which can also provide high cell voltages at open circuit. The open circuit voltage

(V_{OC}) is the voltage of a cell when it is not loaded and it's usually close to the theoretical voltage. The V_{OC} of a lithium cell is given by the difference in the lithium chemical potential between the cathode $\mu_{c\,(Li)}$ and the anode ($\mu_{a\,(Li)}$, according to the following equation:

$$V_{OC} = \mu_{c(Li)} - \mu_{a(Li)} / F \tag{2.10}$$

Where F is the Faraday constant (F= 96485 C/mol). A high V_{OC} can be obtained from a negative anode and a positive cathode that have, smaller and larger work functions respectively.

The cell voltage is given by the energies involved in both electron transfer and Li^+ transfer. The energy involved in the Li^+ transfer is determined by the crystal structure and the coordination geometry of the site into/from which Li^+ is inserted/ removed. Whereas, the energy involved in the electron transfer process is associated with the redox potentials of the ions involved in the cathode and anode [37]. The stability window of the electrolyte is defined by the band gap/energy separation (E_g) between the lowest unoccupied molecular orbital (LUMO) and the highest occupied molecular orbital (HOMO) of the electrolyte. Consequently, thermodynamic stability considerations require the redox energies of the cathode (E_c) and the anode (E_a) to lie within the band gap of the electrolyte, as shown in figure 2.2 below. This is to avoid unnecessary side reactions (oxidation/reduction) with the electrolyte, because a cathode with the $\mu_{c\,(Li)}$ below the HOMO will oxidize the electrolyte and an anode with the $\mu_{a\,(Li)}$ above the LUMO will reduce the electrolyte [36, 38]. The electrochemical stability requirement therefore imposes a limitation on the cell voltage according to the following equation:

$$V_{OC} = (\mu_{c(Li)} - \mu_{a(Li)}) / F \leq E_g \tag{2.11}$$

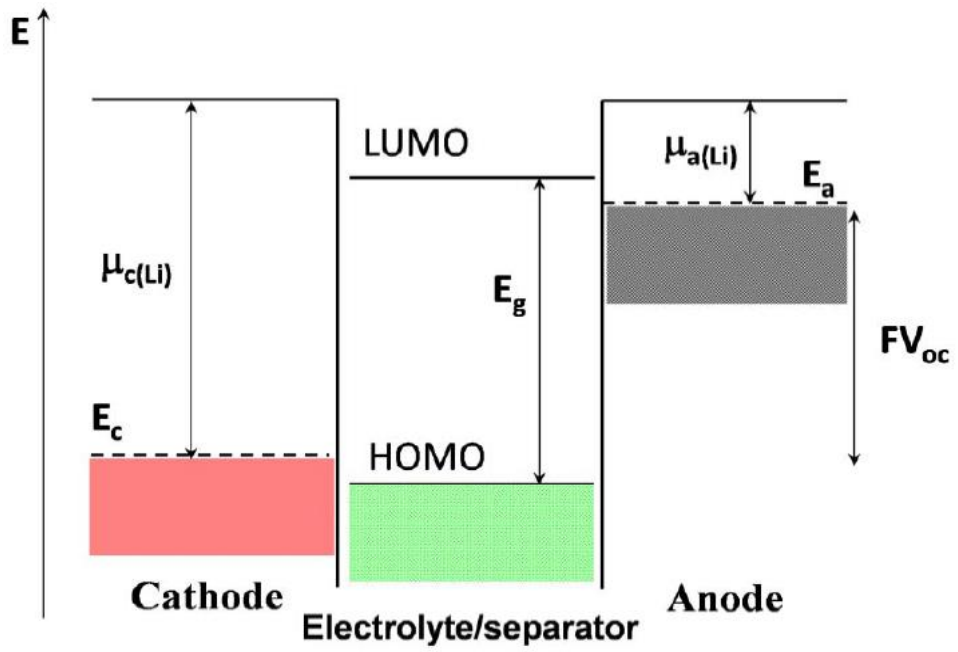

Figure 2.5: Schematic energy diagram of a cell at open circuit [36].

The driving force to work an electrochemical cell is the decrease in the standard free energy, ΔG^{o}, of the cell reaction, given by:

$$\Delta G^{o} = -nFE^{o} \qquad (2.12)$$

Where E^{o} is the potential difference between the cathode and anode; while n is the number of electrons given or accepted by the cathode and anode. When the value of E^{o} is positive, a spontaneous cell reaction occurs [8]. However, when current (I) is applied to the cell, an irreversible energy loss occurs, induced by varying degrees of polarization. The polarizations can be categorized into three classes: activation, Ohmic (IR drop) and concentration polarizations. Activation polarization (η_a) is related to the kinetics of the electrode reaction, arising from charge transfer processes across the electrode-electrolyte interface. Ohmic polarization (IR drop) is associated with the internal impedance of the cell, originating from the ionic resistance of the electrolyte, electronic resistance of the electrodes and contact resistance between the electrode and current collector [36]. Concentration polarization (η_c) is related to mass transfer limitations arising from the difference in concentration of the

reactants/products between the electrode surface and bulk. These polarization losses result in a voltage drop from the open circuit voltage as a function of the operating current, by an amount known as overpotential (η) [8, 36]. The operating voltage (V_{OP}) is given by:

$$V_{OP} = V_{OC} - \eta \tag{2.13}$$

Where, $\eta = \eta_a + \eta_c + IR$ (2.14)

2.3.2 Theoretical capacity

The theoretical capacity of an electrode material is the total quantity of electricity available in a specific electrochemical reaction, and it is dependent on the electron transfer process and the molecular weight of the active material. It can be calculated from Faraday's law as given below. One-gram equivalent weight of a material will deliver 96487 C or 26.8 Ah, known as the Faraday constant.

1F = 1 electron (1.602 x 10-^{19} C) * Avogadro's number (6.023 x 10^{23} atoms/mol), given 96487 C/mol or 26.8 Ah/mol.

If a battery delivers a current of I (amperes) at a time t (seconds), the capacity (Q) is therefore given by I*t in coulombs or ampere seconds [36]. The specific capacity (Q_{sp}) of a battery is given by the capacity of the cell divided by the mass or volume of the cell, given in units of Ah/g (gravimetric capacity) or Ah/L (volumetric capacity) [36].

2.3.3 Coulombic Efficiency

The coulombic efficiency of a battery is the ratio of the discharge capacity (Q_d) to that of the charge capacity (Q_c) of the cell. It indicates the reversibility of the specific battery and is expressed as follows:

$$\text{Coulombic efficiency} = \frac{Q_d}{Q_c} \times 100\ \% \tag{2.15}$$

2.3.4 C-rates

The C-rate of a battery refers to the charged or discharged current of the battery, given as:

$$I = C \times Q_s \tag{2.16}$$

Where I is the discharge or charge current (amperes) and Q_s the specific capacity of the cell. For example, a battery charge/discharge at a 0.1 C-rate indicates a 10-hour charge/discharge of the battery to its cut-off voltage and the charge/discharge current can be calculated from Equation (2.16) above.

2.4 Materials in Lithium-ion batteries

Herein, a detailed review is presented for electrode (cathode, anode), electrolyte, and separator materials for lithium-ion batteries, highlighting their significance on the performance of the state-of-the-art lithium-ion batteries.

2.4.1 Cathode materials for lithium-ion batteries

The cathode in a Li-ion battery is the positive electrode which is associated with the reductive chemical reactions that gain electrons from the external circuit. As earlier mentioned in this chapter, the potential at which lithium is de-intercalated or intercalated is one of the major aspects of a lithium intercalation electrode. Therefore, the potential plays a pivotal role in determining whether a new material is used as a cathode material. Practically, lithium cannot be de-intercalated if the potential is too high, even though it will benefit a high energy density for the material, whereas; a very low potential will lead to moisture sensitivity of the electrode material [39]. The key requirements of a material to be used successfully as a cathode material for the Li-ion battery are outlined below.

- The material should have a low lithium chemical potential to maximise cell voltage
- The redox energy of the material should lie within the band gap of the electrolyte to avoid undesirable site reactions at the electrode-electrolyte interface

- The insertion compound should be able to insert/extract a large number of lithium ions to maximise cell capacity
- The intercalation material should be able to reversibly insert/extract lithium ions with minimal or no change in structure to attain good cycle life
- The material should show good electronic and lithium ion conductivity to eliminate polarisation losses during cycling
- The insertion compound should be low cost and environmentally friendly

Based on the above criteria, a variety of intercalation compounds have been investigated as cathode materials for lithium-ion batteries, some of which have been commercialized while others are still under research. A brief review on some cathode materials for lithium-ion batteries will be presented below, ranging from the layered metal oxides ($LiCoO_2$, $LiNiO_2$), the spinel ($LiMn_2O_4$), polyanionic compounds (olivine $LiFePO_4$) to the orthosilicate (Li_2MnSiO_4, Li_2FeSiO_4) families of electrode materials.

2.4.1.1 Layered metal oxides

2.4.1.1.1 Layered $LiCoO_2$

$LiCoO_2$ is the conventional cathode material used in lithium-ion batteries, which was discovered by Goodenough and co-workers in 1980 [40]. It is a high energy density cathode material with a distorted rock salt (α-$NaFeO_2$) structure where the cations (Li^+ and Co^{3+}) fill octahedral closed packed alternating (111) planes, through which delithiation and lithiation can occur [39-40]. $LiCoO_2$ offers a high theoretical capacity of ~274 mAh/g upon complete delithiation, and a high operating voltage ~4 V. However, only about half of its theoretical capacity (~140 mAh/g), is used in practical lithium-ion cells due to structural and chemical instabilities during the delithiation process [36]. Delithiation of more than 0.5 mols of Li^+ ions per formula unit of $LiCoO_2$ results in chemical instabilities due to oxygen evolution [41], according to the following equation:

$$2Co^{4+} - O^{2-} = 2Co^{3+} - O^{-} = 2Co^{3+}(O_2)^{2-} + O_2 + 2e^{-} \qquad (2.17)$$

The Low-spin $C0^{4+}/Co^{3+}$ couples are pinned at the top of the O^{2-}:$2p^6$ bands, with corresponding pi-bonding, which leads to a transition from polaronic to migratory holes in the CoO_2 array [41]. This eventually causes a significant disorder in the structure which leads to capacity fading during cycling.

Considerable efforts have been made to minimise the chemical instability and capacity fading of $LiCoO_2$ by surface modifications using nanostructured inert oxides such as Al_2O_3, MgO, ZnO, ZrO_2 and TiO_2. Significant enhancement in the reversible capacity of $LiCoO_2$ were achieved from ~140 mAh/g to ~200 mAh/g, equivalent to reversible extraction of 0.7 mols of Li^+ ions per formula unit [36].

Despite the high energy density and performance of $LiCoO_2$ as cathode material in lithium-ion cells, alternatives are being developed to reduce cost and improve stability. Moreover, cobalt is even more expensive than other transition metals such as manganese, nickel and iron [40]. Therefore, other layered metal oxide cathode materials like $LiNiO_2$ and the spinel $LiMn_2O_4$ have been extensively studied to replace $LiCoO_2$ due to their low cost and chemical stability.

2.4.1.1.2 Layered $LiNiO_2$

$LiNiO_2$ also forms the α-$NaFeO_2$ structure. It is lower in cost and comparatively higher in energy density than $LiCoO_2$. However, $LiNiO_2$ possesses a major structural instability due to the migration of nickel ions (Ni^{3+}) from the octahedral sites of the nickel plane to those of the lithium plane, especially at high temperatures due to the lower octahedral-site stabilization energy associated with the low spin Ni^{3+} [36, 40]. This eventually leads to degradation in capacity during the charging/discharging process.

Partial substitution of nickel with cobalt in $LiNiO_2$ results in improved ordering, whereby, nickel ions occupy the octahedral nickel/cobalt planes instead of lithium planes. The $LiNi_{1-x}Co_xO_2$ layered oxide with more nickel content (x=0.2) has been successfully used as a replacement for the toxic and unavailable $LiCoO_2$ due to its low cost and higher capacity.

2.4.1.2 The Spinel

2.4.1.2.1 The Spinel Oxide $LiMn_2O_4$

$LiMn_2O_4$ forms a spinel structure in which manganese occupies octahedral sites whereas lithium occupies the tetrahedral sites, forming a 3D-network of channels instead of planes as in the layered α-$NaFeO_2$ structure [40]. The spinel $LiMn_2O_4$ is considered as a potentially attractive substitute for the already commercialized layered $LiCoO_2$ oxide due to its high abundance, cost effectiveness and environmental friendliness [42]. However, the reversible capacity and cycleability of this intercalation compound is limited by Jahn-teller distortions (disproportionation reaction of Mn^{3+} ions into Mn^{2+} and Mn^{4+} ions upon the first discharge process), manganese dissolution and electrolyte decomposition. During the discharge process, the diffusion of Li^+ ions is much faster in the electrolyte than the spinel $LiMn_2O_4$ cathode material, causing Li^+ ions to heap at the surface of the spinel and in effect, forming a Mn^{3+} region which promotes Jahn-teller distortion [43]. And the faster the discharge rate, the higher the distortion.

Many approaches have been employed by researchers to inhibit the Jahn-teller distortion of the spinel $LiMn_2O_4$ cathode material, ranging from cationic doping of the manganese site with cations such as Co, Ni, Fe, and Cr to surface modifications by coating the surface of the spinel with a metal oxide (Al_2O_3) or a substituted intercalation compound ($LiNi_xMn_{2-x}O_4$) as shell [43-44]. Cationic doping significantly decreases the Jahn-teller distortion (due to the reduced amount of the Jahn-teller active Mn^{3+} ions) and enhances electrochemical cycling of the cathode material. Surface modification of the spinel $LiMn_2O_4$ reduces manganese dissolution and shows stable cycling performance [44-45].

2.4.1.3 Polyanion intercalation compounds

Following the instability at deep charge and the associated safety concerns coupled with the highly oxidized redox couples of $Co^{3+/4+}$ and the $Ni^{3+/4+}$in the layered oxides, and the Jahn-teller distortion of Mn^{3+} ions in the spinel cathode, Manthiram and Goodenough introduced the polyanion compounds as lithium intercalation hosts in the late 1980's [46]. The most extensively studied polyanion cathode materials are the phosphates ($LiMPO_4$, M= Fe, Mn, Co,

and Ni) crystallizing in the olivine structure [10]. The olivine structure consists of a slightly distorted hexagonal close-packed oxygen array with an orthorhombic structure, wherein: Li and M metal atoms are found in half of the octahedral sites and P atoms occupy 1/8 of the tetrahedral sites of the oxygen hexagon [10]. The MO_6 octahedra and PO_4 tetrahedra both share edges and corners forming a host structure with strong 3-dimensional bonding.

2.4.1.3.1 Olivine $LiFePO_4$

$LiFePO_4$ was identified in the late 1990's as a cathode material, crystallizing in the olivine structure with a flat discharge profile around 3.4 V and a theoretical capacity of 170 mAh/g [46]. It is the most commercially successful and extensively studied polyanion olivine phosphate, and has attracted much attention due to its low cost, environmental benignity, abundant raw materials and excellent safety offered by the covalently bonded PO_4 groups with the chemically more stable $Fe^{2+/3+}$ couple [46-47]. $LiFePO_4$ is considered as the most promising cathode material for application in Plug-in and Hybrid Electric vehicles. It has high thermal stability in both charged and discharged states, which enables proper functioning both at high temperatures and even under harmful conditions [10].

However, $LiFePO_4$ suffers from poor electronic conductivity and slow Li^+ ion transport, which limits its high rate applications. Many efforts have been made to improve the electrochemical performance of this cathode material, including cationic doping on the lithium and iron sites, surface modification using conductive additives and particle size reduction [48]. Of these methods, particle size reduction is an effective approach which significantly enhances the electrochemical performance of olivine $LiFePO_4$. For instance, Manthiram *et al.,* produced single-crystalline $LiMPO_4$ with nano-thumblike morphologies which demonstrated excellent high rate capability due to a decrease in the diffusion path length of both Li^+ ions and electrons [49]. Moreover, addition of a conductive phase is usually needed to achieve satisfactory performance [40].

2.4.1.4 Lithium transition metal orthosilicates

The drive to extend the useful range of lithium intercalation and deintercalation to maximise cell capacity and to keep a high discharge voltage to achieve optimal energy density with improved safety while using non-toxic, low cost and environmental benign materials, attracted lithium transition metal orthosilicates (Li_2MSiO_4, M = Mn, Fe) as the most promising candidates for next generation cathode materials for lithium-ion batteries [50]. Interestingly, the orthosilicates show the possibility of extracting 2 mols of Li^+ ions per formula unit (FU) (utilizing the $Mn^{2+/3+}$ and $Mn^{3+/4+}$ redox couples), which translates to a high theoretical capacity (> 300 mAh/g upon complete extraction and re-insertion of the 2 mols of Li^+ ions) unlike the lithium transition metal phosphates which can only exchange one mol of Li^+ ion per formula unit. The natural abundance of Si, Mn and Fe coupled with the strong Si-O bonds which offer excellent stability and safety make the orthosilicate class of electrode materials an attractive alternative to the layered transition metal oxides and the most commercially available olivine phosphate [51-53].

Li_2MSiO_4 intercalation compounds are related to the Li_3PO_4 structure, where lithium and transition metal cations are positioned in tetrahedral sites in a distorted hexagonal-closed-packed oxygen array [10, 15]. This family of tetrahedral compounds exhibit a rich polymorphism with two main classes (β and γ-Li_3PO_4 phases) depending on the distribution of cations over the tetrahedral sites [10]. The β and γ-phases represent the low and high temperature forms of Li_2MSiO_4 respectively, and can change from one form to the other when half of the occupied cation tetrahedra sites replace the unoccupied sites. All the cation tetrahedra point in the same direction for the β-phase and are aligned perpendicular to the closed packed planes, sharing only corners with each other. For the γ–phase, half of the cation tetrahedra point in one direction and the other half points in the opposite direction, sharing only edges [10, 54].

2.4.1.4.1 Lithium manganese orthosilicate (Li_2MnSiO_4)

Li_2MnSiO_4 is the most promising cathode material among the orthosilicate family of electrode materials due to its high redox potential and the possibility of complete delithiation of $Li_2Mn^{2+}SiO_4$ to $Mn^{4+}SiO_4$, exploiting the $Mn^{2+/3+}$ and $Mn^{3+/4+}$ (~4 V versus Li) with a high

theoretical capacity of 333 mAh/g, unlike its Fe counterpart which only functions on the $Fe^{2+/3+}$ (~2.76 V versus Li) with a nominal capacity of 166 mAh/g [55-57]. Despite the numerous outstanding potentials of Li_2MnSiO_4, it possesses low electronic conductivity (~5 x 10^{-16} Scm^{-1}at room temperature to ~3 x 10^{-14} Scm^{-1} at 60 ^oC [58], which greatly affects its high rate applications. Previous electrochemical reports on Li_2MnSiO_4 demonstrate low electrochemical performance with severe capacity fading. Moreover, the Mn^{2+} in Li_2MnSiO_4 cathode material presents structural instability caused by the Jahn-Teller distortion of the manganese site upon discharging, leading to subsequent amorphization.

Polymorphism which is more prevalent in the orthosilicate intercalation compounds also significantly affects the electrochemical performance of Li_2MnSiO_4 electrode material. Li_2MnSiO_4 exhibits three structural forms (polymorphs) related to the low and high temperature forms. The orthorhombic forms which are based on the β-Li_3PO_4 structure with space groups $Pmn2_1$ and Pmnb, have two-dimensional pathways for Li^+ ion diffusion whereas, the monoclinic form based on the γ–Li_3PO_4 structure with space group $P2_1/n$ has Li^+ ion sites interconnected in three directions [15]. Previous work by Kuganathan and Islam on intrinsic defects and Li^+ ion mobility on different polymorphs of Li_2MnSiO_4 cathode material demonstrated lower activation energies for Li^+ migration in the monoclinic polymorph compared to the orthorhombic forms, indicating better Li^+ ion mobility, hence better rate capability and capacity retention in the later than the former [60].

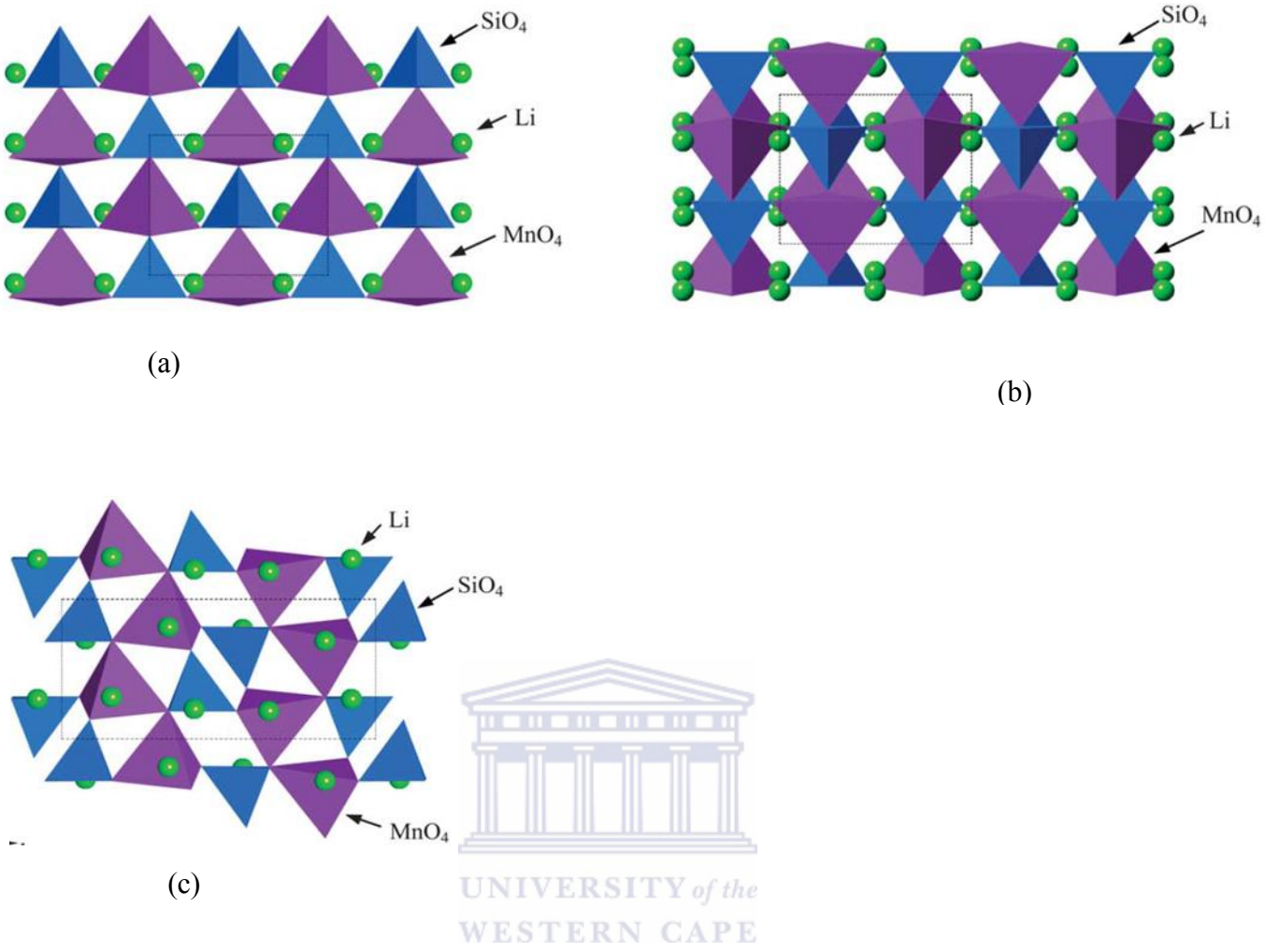

Figure 2.6: Crystal structures of Li_2MnSiO_4 polymorphs (a) orthorhombic $Pmn2_1$ phase, (b) orthorhombic Pmnb phase, (c) monoclinic $P2_1/n$ phase, revealing arrangement of MnO_4 tetrahedra (purple), SiO_4 tetrahedra (blue) with Li-ions (green) [54].

Several strategies have been devoted by many researchers to overcome the low intrinsic electronic conductivity and structural instability of Li_2MnSiO_4 cathode material, including particle size reduction, partial substitution of the manganese site with metals like Fe, Cu and Mg, surface modification using carbon coating and metal oxides such as ZnO and fine-tuning the morphology for optimal performance using specialised matrices [55, 61-64]. Considerable improvements have been achieved in enhancing the electrochemical performance of Li_2MnSiO_4 cathode material.

High charge capacities of 275 mAh/g and 216 mAh/g with good capacity retention over 80 cycles have been reported by Wang and Zhu *et al.,* [64]. Recently, novel synthesis methods have been developed to fine-tune the particle size and morphology of the Li_2MnSiO_4 particles, which also demonstrated high capacities [65]. However, further studies are required to fully realize the structural instability when lithium is extracted from Li_2MnSiO_4, the effect of different polymorphs on the electrochemical performance and the production of well-defined, reliable and high performing Li_2MnSiO_4 materials.

2.4.2 Anode Materials

The anode in a lithium-ion battery is the negative electrode, associated with the oxidative chemical reactions that release electrons into the external circuit. Materials with high specific capacity and low voltage have attracted great attention. Lithium metal due to its appealing properties such as being the lightest ($0.534 gcm^{-3}$) and most electronegative (-3.04 V) metal, which conferred on it a high theoretical capacity (3860 mAh/g) had been long used as an anode material [66]. Lithium dendrite formation which resulted to serious safety hazards lead to the failure of lithium metal as an anode material and inspired the search for safer and high capacity anode materials. 'Host-guest' chemistry has been considered and many intercalation compounds have been investigated as anode materials for lithium-ion batteries ranging from carbon based materials, metal alloys to metal oxides [67].

2.4.2.1 Carbon based anodes

Carbonaceous materials are very attractive as carbon is so abundant, with a high chemical stability and a wide electrochemical potential window [36]. Graphite with a redox energy close to that of lithium is the most commonly used anode material in commercial lithium-ion batteries. Carbon based anodes can overcome the problem of lithium dendrite formation by reversible intercalation of lithium into the carbon host lattice, providing good cyclability and safety for the lithium-ion battery anode [67]. The host-guest (lithium insertion/extraction) process in graphite can be illustrated by Equation (2.18) below.

$$6C + xLi^+ + xe^- \leftrightarrow Li_xC_6 \qquad (2.18)$$

However, graphite has a restricted theoretical capacity ~ 372 mAh/g. Moreover, the insertion of lithium results in the formation of a solid-electrolyte interface (SEI) at very low potentials, which inhibits the exfoliation of graphite layers and any further reaction of the graphite anode during cycling [36, 67]. The SEI results in irreversible capacity loss and overall capacity fading during cycling.

To increase the lithium storage capacity and the overall energy and power densities of the carbon based anodes, nanostructured one-dimensional (1D) and two-dimensional (2D) structures such as carbon nanotubes and graphene due to their high surface-to-volume ratios and excellent surface activities have been studied as anode materials for lithium-ion cells. These nanostructured 1D and 2D carbonaceous materials have demonstrated a high degree of Li intercalation with a reversible capacity exceeding 460 $mAhg^{-1}$ up till 1116 $mAhg^{-1}$ for the carbon nanotubes (1D), depending on the post-treatment methods, and first charge and discharge capacities of 1233 $mAhg^{-1}$ and 672 $mAhg^{-1}$ for graphene (2D) respectively [67]. But, the coulombic efficiency of carbon based 1D anodes was found to be low compared to graphite, due to large structural defects and a high voltage hysteresis. 2D carbon based anodes have also been found to show low initial Coulombic efficiency and large irreversible capacity. This can be explained by the reaction of Li-ions with oxygen functional groups, and the formation of the SEI during the oxidation of graphene.

2.4.2.2 Metal alloy anodes

Li can be alloyed electrochemically with metals and non-metals especially elements of groups IV and V such as Si, Sn, Ge, Pb, P, AS, Sb and Bi with other metal elements like Al, Zn, Au, In, Ga, Cd, Mg and Ag [67]. The Li alloying process can be achieved when preparing the electrodes or during the first charge cycle after the electrodes have been prepared. The alloyed electrodes possess modest operation potentials versus Li insertion/extraction, good safety and high specific capacities.

The only drawback obstructing the establishment of these anodes is the volume change during the alloying/de-alloying stages, which results in serious cracking and collapsing of the electrodes with subsequent electrical contact between the particles and overall significant irreversible capacity and severe capacity fading [67].

Several approaches have been used by many researchers to overcome this challenge including: preparation of unique nanostructures; forming nanocomposites using metal nanoparticles and a carbon matrix to act as a buffer for the volume change; and forming alloys with an electrochemically active/inactive phase which will be responsible for accommodating the volume change during cycling. Although the nanostructured anodes have demonstrated promising properties such as high stable and reversible capacities of 900 $mAhg^{-1}$ over 50 cycles, their high cost and poor capacity retention limits them from meeting the requirements of many practical applications such as hybrid electric vehicles and advanced electrical storage devices [67]. Therefore, a proper production process is required in this regard to make use of relatively cheap materials and suitable electrode designs in terms of microstructure and composition which are necessary to lower production cost and maintain the structural integrity and improve the capacity retention and rate capability.

2.4.2.3 Metal Oxide anodes

Various metal oxides have been investigated as anode materials for Li-ion batteries because of their diverse physical and chemical properties and their high reversible capacities ranging from 500 – 1000 $mAhg^{-1}$. SnO_2, TiO_2 and transition metal oxides (MO_x, where M= Fe, Co, Ni, Cu, Ru and Gr) have been extensively studied as anode materials but these materials operate according to different reaction mechanisms, namely: Li-alloy reaction mechanism, insertion/extraction mechanism which involves the insertion/extraction of Li into/from the lattice of the transition metal oxide; and the formation reaction mechanism involving the formation and decomposition of Li_2O accompanying the oxidation and reduction of the transition metal nanoparticle respectively [66-68].

SnO_2 which is the most important metal oxide in the category of the Li-alloy reaction mechanism alloys with Li according to the following mechanism; on the first charge, Li bonds with oxygen from SnO_2 forming Li_2O while Sn continues to form an alloy with Li with an upper limit of $Li_{4.4}Sn$ which translates to a theoretical capacity of 783 $mAhg^{-1}$. The reaction is reported as follows:

$$SnO_2 + 4Li^+ + 4e^- \rightarrow Sn + 2Li_2O \quad (2.19)$$

$$Sn + 4.4Li^+ + 4.4e^- \leftrightarrow Li_{4.4}Sn \quad (2.20)$$

Upon continues cycling, Sn formed from the delithiation of Li-Sn alloy possesses a strong aggregation tendency and starts forming clusters. These clusters quickly degrade the reversible capacity of the Li-Sn alloy due to the volume change of Sn and the destruction of the Li_2O matrix. Much attention has been devoted to reduce the irreversible capacity and improve the performance of SnO_2 anodes, including: porous SnO_2 nanostructures; SnO_2-carbon nanocomposites; SnO_2 thin films and hollow-sphere mesophores. Most of these materials showed high reversible Li storage capacities and improved cycling performance, due to the synergistic effect of the conductive and structural stabilizing carbon matrices and the high storage capacity of the SnO_2 nanoparticles [68].

Owing to the wide-spread availability, low toxicity and eco-friendliness of TiO_2, it has become one of the most studied insertion reaction-based metal oxide anodes [68]. Insertion reaction-based anodes are usually low specific capacity electrodes due to limited sites for accommodating Li during the insertion reaction. Anatase is the most electro-active polymorph of TiO_2 compared to its counterparts (rutile and TiO_2-B). The reversible reaction between Li and TiO_2 can be expressed according [68]:

$$xLi^+ + TiO_2 + xe^- \leftrightarrow Li_xTiO_2 (0 \leq x \leq 1) \quad (2.21)$$

This insertion/ extraction reaction takes place at ~1.7 V versus Li/Li^+, where the Li^+ insert into and de-intercalate out of the interstitial vacancies of the TiO_2 framework, with a maximal lithium exchange of around x= 0.5 in anatase [68]. The major limitation of the TiO_2-based anodes is the poor Li^+ transport kinetics and the low electronic conductivity of TiO_2. Nanostructured mesoporous anatase TiO_2 has been recently prepared and these materials exhibited improved Li-storage capacity and good cycling performance [67]. For instance, anatase TiO_2 nanotubes with mesoporous walls within anodic aluminium oxide membranes

showed a Li-storage capacity of 340 $mAhg^{-1}$. This could be explained by the fact that, the nanotubes provided effective pathways for both Li-ions and electrons which are crucial for high-rate capabilities [67].

Many transition metal oxides follow the conversion reaction mechanism: whereby the oxides are converted to the metallic state with the formation of Li_2O component at the first lithiation, and are reversibly brought back to their initial state after delithiation. This mechanism is illustrated as follows [67]:

$$M_xO_y + 2yLi^+ + 2ye^- \leftrightarrow xM + yLi_2O \quad (2.22)$$

The conversion reaction-based transition metal oxide anodes exhibit high reversible capacities and high energy densities due to the fact that the oxidation state is fully utilized and more than one electron is involved in the conversion process. Table 2.1 below summarizes the most widely investigated conversion reaction-based transition metal oxide anodes with their theoretical capacities and typical nanostructures.

Table 2.1: Most widely studied conversion reaction-based transition metal oxide anodes [67]

Metal Oxide		**Theoretical capacities ($mAhg^{-1}$)**	**Typical Nanostructures**	**Common problems and possible solutions**
Iron oxides	Fe_2O_3	1007	Nanostructures and C-based nanocomposites	**Common problems**; Low Coulombic efficiency at first cycle, unstable SEI film formation, large potential hysteresis and poor capacity retention **Possible solutions**; • Metal Oxide/C composites using
	Fe_2O_4	926		
Cobalt oxides	Co_3O_4	890	Nanostructured Co_3O_4 or Co_3O_4/C nanocomposites	
	CoO	715	CoO composites	
Manganese oxides	MnO_x	700-1000	Nanostructures and MnO_x/C nanocomposites	
Molybdenum oxides	MoO_3	1111	Doped MoO_3	
	MoO_2	830	MoO_2nanomaterials	

Copper oxides	CuO	674	Nanostructured CuO	carbon as buffer and electro-active materials • Nanostructured metal oxides to provide high surface area and quantum confinement effects
	Cu_2O	375	Cu_2O/C composites	
Chromium oxide	Cr_2O_3	1058	Nanostructures, hetero-atom doping and C-based nanocomposites	
Nickel oxide	NiO	718	NiO/C nanocomposites and porous NiO	
Ruthenium oxide	RuO_2	1130	RuO_2/SnO_2nanocomposites	

2.4.3 Electrolytes

An electrolyte is a component in a battery cell which provides pure ionic conductivity between the cathode and anode materials. Apart from having a large energy window Eg, the electrolyte is required to satisfy several other requirements [69] such as:

- Chemical stability with respect to the electrodes, including the ability to form rapidly a passivating SEI layer where kinetic stability is required because the electrode potential lies outside the electrolyte window.
- Chemical stability over ambient temperature ranges and temperature in the battery under high power.
- A Li-ion conductivity> 10^{-4} Scm^{-1} over the temperature range of a battery operation.
- An electronic conductivity < 10^{-10} Scm^{-1}
- Retention of the electrode/electrolyte interface during cycling even after volume change of the electrode particles
- Safe, for instance, non-flammable and non-explosive even when cell is short-circuited
- Low toxicity and low cost.

However, meeting these requirements has proven to be a tough challenge, even though every electrolyte has its drawbacks and benefits.

Table 2.2: Non-aqueous electrolyte systems for Li-ion batteries [66, 69]

Electrolytes	Example of classical electrolytes	Ionic conductivity (10^{-3} S/cm) at room temp	Electrochemical window vs Li^+/Li^0		Remark
			Reduction	**Oxidation**	
Organic liquids	1M $LiPF_6$ in EC: DEC (1:1)	7.0	13	4.5	Flammable
	1M $LiPF_6$ in EC: DEC (1:1)	10	13	>5	
Ionic liquids	1M LiTFSI in EMI-TFSI	2.0	1.0	5.3	Non-flammable
	1M $LiBF_4$ in EMI-BF_4	8.0	0.9	5.3	
Polymer	LiTFSI-P(EO/MEEGE)	0.1	<0.0	4.7	Flammable
	$LiClO_4$-PEO + 10 wt% TiO_2	0.02	<0.0	5.0	
Inorganic solid	$Li_{4-x}Ge_{1-x}P_xS_4$(x=0.75)	70	<0.0	>5.0	Non-flammable
	$0,05Li_4SiO_4$ + 0.5 Li_2S+ $0.38SiS_2$			>8.0	
Inorganic liquid	$LiAlCl_4$ + SO_2	4.2	<0.0	4.4	Non-flammable
Inorganic liquid + polymer	$0.04LiPF_6$ + 0.2EC + 0.62DMC + 0.1PAN	3.0	-	4.4	Flammable
	$LiClO_4$ + EC + PC PVdF		-	5.0	
Ionic liquid + polymer	1M LiTFSI + P_{13}TFSI + PVdF- HFP	0.18	<0.0	5.8	Less flammable
Ionic liquid + polymer + liquid organic	56 wt% LiTFSI-Py_{24}TFSI + 30 wt% PVdF-HFP + 14 wt% EC/PC	0.81	1.5	4.2	Less flammable
Polymer + Inorganic solid	2 vol% $LiClO_4$-TEC-19 + 98 vol%	0.03	<0.0	>4.5	Non-flammable
	95 ($0.6Li_2S$ + $0.4Li_2S$) + $5Li_4SiO_4$				

A typical electrolyte for lithium ion batteries consists of a lithium salt and a solvent. The lithium salt provides the source of lithium ions in the electrolyte while the solvent serves as a medium for lithium ion diffusion during the insertion/extraction of lithium ions into/out of the electrodes. For instance, majority of current electrolytes for lithium ion batteries are based on two prime components; ethylene carbonates (EC), used as the solvent and lithium hexafluorophosphate ($LiPF_6$), used as the lithium source. Generally, one or more linear carbonates chosen from dimethyl carbonate (DMC), diethyl carbonate (DEC), and even ethylmethyl carbonate (EMC), are used as co-solvents to enhance the fluidity and decrease the melting point of the electrolyte, and hence forming a common mixture consisting of $LiPF_6$/EC/linear carbonate (S) [70].

2.4.4 Separator

The Separator is a crucial component in liquid electrolyte batteries and is located between the cathode and anode materials to prevent physical contact of the electrodes while enabling free ionic transport and preventing electrons from flowing directly from anode to cathode, thus allowing the electrons to flow through an external circuit. The separator mostly is a micro porous layer consisting of either a polymeric membrane or a non-woven fabric mat. It is chemically and electrochemically stable towards the electrolyte and electrode materials, and doesn't participate in any cell reactions. However, its properties considerably affect the performance and safety of the battery [71]. Most commercial lithium-ion batteries use polyethylene (PE) and Polypropylene (PP) separators or their blends (PE-PP).

2.5 Significance of Nanotechnology on the performance of Li-ion batteries

One of the major innovations of the 21st century has been the design of materials in nanodimensions, which led to miniaturization in micro-electronics [72]. The rapid growth of consumer electronics necessitates the fabrication of high energy density and high power density materials for energy storage devices. Lithium-ion battery technology is an efficient power source due to its high potential, energy density and cycle life [72].

In the lithium-ion battery, the relevant size effects range from purely geometrical effects to those in which the local thermodynamics is diverse. However, the advantages of using nanosized materials in lithium-ion batteries have been presented in many review articles [73-75]. Lithium-ion diffusion in host electrode materials is associated with lithium-ion diffusion coefficient and the diffusion length. The characteristic time for diffusion can be represented according to the following equation [73]:

$$\tau = {L^2}/{D_{Li}} \tag{2.23}$$

where L is the lithium ion diffusion length, which is related to the size of the intercalation compound particle, D_{Li} is the lithium-ion diffusion coefficient.

The time (τ) for lithium ion intercalation decreases with the square of the diffusion length. Thus, minimizing the particle size to shorten the lithium-ion diffusion length is an effective strategy for enhancing the rate capability of electrode materials [76]. Moreover, nanosized materials have higher surface area which can achieve a high contact interface between the electrode and electrolyte, and therefore providing more sites for lithium-ion diffusion [76-77].

Other exclusive properties of materials with nanodimensions include: high surface energy, fast lithium-ion dynamics, better strain accommodation and mechanical integrity during lithium-ion intercalation/de-intercalation and low charge transfer resistance [72-73, 75]. These properties are all beneficial to high power lithium-ion rechargeable batteries. In contrast, commercial batteries are mostly based on micrometre-sized electrode materials having low surface area with longer diffusion lengths for lithium-ions. From the point of view of Li-ion diffusion, these micro-sized electrode materials are not favourable for high-rate lithium-ion batteries [76, 78]. Even though the strategy of enhancing the rate capacity by making use of nanosized particles has been successfully applied with most electrode materials, cost effective synthetic routes which produces phase pure nanostructures have not been widely exploited. In this research, we make use of nanostructured materials coupled with the advantage of hydrothermal synthesis which produces phase pure materials and using environmentally

friendly and cost effective raw materials to design a next generation high energy density cathode material for possible application in Li-ion batteries.

CHAPTER 3

Chapter Overview

This chapter kicks off by outlining the various chemicals used in the design of the nanostructured pristine lithium manganese orthosilicate (Li_2MnSiO_4) and the novel alumina-capped lithium manganese orthosilicate (Li_2MnSiO_4/Al_2O_3) cathode materials. It further discusses in detail the experimental procedures involved in the fabrication of the nanostructured pristine and novel cathode materials. And lastly, a summary on the instrumentation and experimental techniques used for the characterisation of the synthesized nanostructured pristine and novel Li_2MnSiO_4 cathode materials is presented.

3.0 Experimental Section

3.1 Chemicals

The chemicals used in the experimental section include: aluminum isopropoxide ($C_9H_{21}O_3$, ≥ 98%), ethanol (C_2H_6O, absolute), reagent grade lithium hydroxide (LiOH, 98%), lithium nitrate ($LiNO_3$, 99.99% trace metal basis), manganese (II) chloride tetrahydrate ($MnCl_2.4H_2O$, 99.99% trace metal basis), N-methyl-2-pyrollidone (anhydrous, 99.5%) and silicon dioxide nanopowder, 10-20 nm particle size, (SiO_2, 99.5% trace metal basis). All the chemicals were purchased from Sigma Aldrich, and were used without further purification.

3.2 Procedures

The following procedures were employed for the synthesis of the nanostructured pristine and modified Li_2MnSiO_4 cathode materials.

3.2.1 Synthesis of Nanostructured pristine Li_2MnSiO_4 cathode material

The pristine cathode material was prepared by a versatile hydrothermal synthetic pathway using stoichiometric amounts of SiO_2 nanopowder, LiOH and $MnCl_2.4H_2O$. Typically, 1.2016 g of nano SiO_2 was dispersed in 8 mL of oxygen free distilled water and stirred for 30 min. Thereafter, 9 mL of 0.04 moles of LiOH were slowly added to the SiO_2 dispersion and mixture was vigorously stirred for another 30 min. 9 mL of 0.02 moles of $MnCl_2.4H_2O$ was subsequently added to the above mixture and allowed to stir further for an hour, then sealed in a 25 mL Teflon-lined autoclave under auto-generated pressure for 6 h at 200 ^oC. After the hydrothermal treatment was completed, the resulting powder was purified by way of centrifuging, rinsed severally with water and ethanol and dried under vacuum overnight at 80 ^oC to obtain a powder. The nanostructured pristine Li_2MnSiO_4 was finally obtained by calcinating the dry powder at 750 ^oC in a muffle furnace for 10 h, in order to get rid of any amorphous precursors or impurities introduced during synthesis.

3.2.2 Synthesis of the Novel lithium manganese orthosilicate-capped alumina nanofilm

The novel nanostructured cathode material was obtained by dispersing desired amounts of aluminum isopropoxide [$Al(OR)_3$] and the pristine material (Li_2MnSiO_4 nanoparticles) in ethanol (absolute) with constant stirring, followed by evaporation to dryness with a subsequent calcination step. The amount of $Al(OR)_3$ used in forming the nanofilm was 3 wt% of the pristine material. Firstly, alumina nanoparticles were formed by dispersing $Al(OR)_3$ powder in ethanol for 2 h, followed by the addition of Li_2MnSiO_4 nanoparticles to the dispersion. The slurry was mixed vigorously for 4 h, transferred to a rotor evaporator (rotavapor) to evaporate the solvent, and then dried in a vacuum oven for 6 h at 70 ^oC to obtain a powder. The novel lithium manganese orthosilicate-capped alumina nanofilm (Li_2MnSiO_4/Al_2O_3) nanostructured cathode material was finally obtained by calcinating the powder at 550 ^oC in a muffle furnace for 5 h to remove any organic residues or impurities hovering around the nanoparticles. Al_2O_3 nanoparticles were obtained using the same procedure, but without addition of the pristine cathode material.

The experimental design for the synthesis of the pristine and novel nanostructured cathode materials is structured as follows:

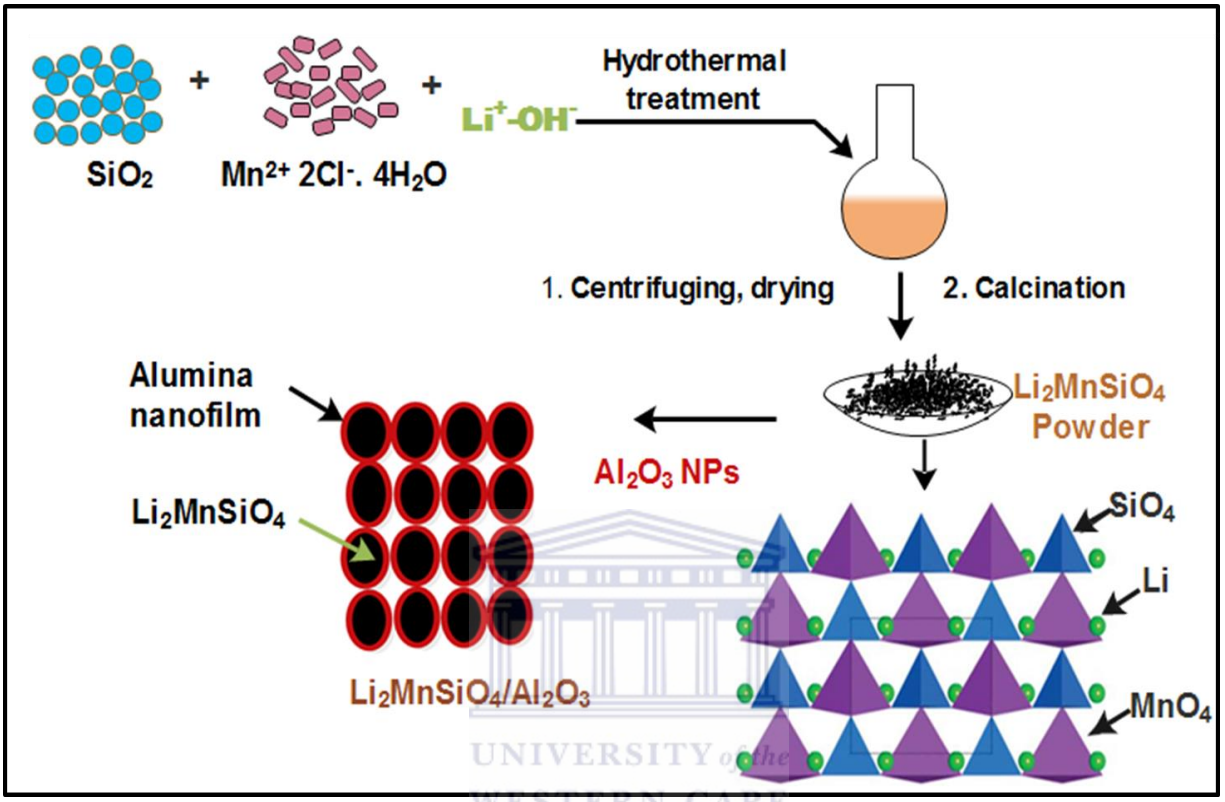

Scheme 3.1: Experimental design for the synthesis of the pristine and novel nanostructured Li_2MnSiO_4 cathode materials.

3.3 Material characterisation techniques and instrumentation

A variety of characterisation techniques and instrumentation were employed to investigate the structural, morphological and spectroscopic features of the synthesized materials and their electrochemical performance.

3.3.1 Structural and spectroscopic characterisation techniques/ instrumentation

The surface morphology and particle size distribution, functional groups present, crystal and electronic structure of the synthesized pristine and novel Li_2MnSiO_4 cathode materials were ascertain using High Resolution Scanning Electron Microscopy (HRSEM) and Transmission Electron Microscopy (HRTEM), Fourier-Transform Infra-red Spectroscopy (FTIR), X-ray Diffraction (XRD), Solid State ^{7}Li- Nuclear Magnetic Resonance spectroscopy (^{7}Li SS-NMR) and X-ray Photoelectron Spectroscopy (XPS) respectively.

3.3.1.1 Microscopic characterisation by HRSEM and HRTEM and instrumentation used

3.3.1.1.1 High-Resolution Scanning Electron Microscopy

HRSEM is one of the most powerful tools used to establish the surface morphology and elemental composition of nanomaterials. Generally, a beam of electrons (produced by an electron gun) passes through scan coils and an objective lens that deflects horizontally and vertically so that the beam scans the surface of the specimen in a raster pattern. As electrons penetrate the surface, a number of interactions occur, which result in emission of electrons such as; secondary electrons (low energy electrons) and backscattered electrons (high energy electrons) [79]. The secondary electrons are those used for determining the surface morphology of a specimen. A fraction of the electrons emitted by the surface are amplified and converted into a digital camera system connected to different detectors. As the electron beam scans the surface of the sample, a topographical representation of the surface is revealed. Three types of images are produced by HRSEM: secondary and backscattered images and elemental X-ray maps. These images range in a few nanometres and can be observed in low or high vacuum. The basic operating principles of HRSEM are represented on figure 3.1 below.

HRSEM has been used by many researchers to examine the morphology and microstructure of nanomaterials. In this study, HRSEM was employed to investigate the surface morphology and to obtain the elemental composition/ X-ray maps of the pristine and novel nanostructured cathode materials.

SEM images were obtained using a ZEISS ULTRA scanning electron microscope. The sample was placed on a carbon supported by alumina and sputter coated for 30 min with a gold-palladium alloy to make the samples conductive.

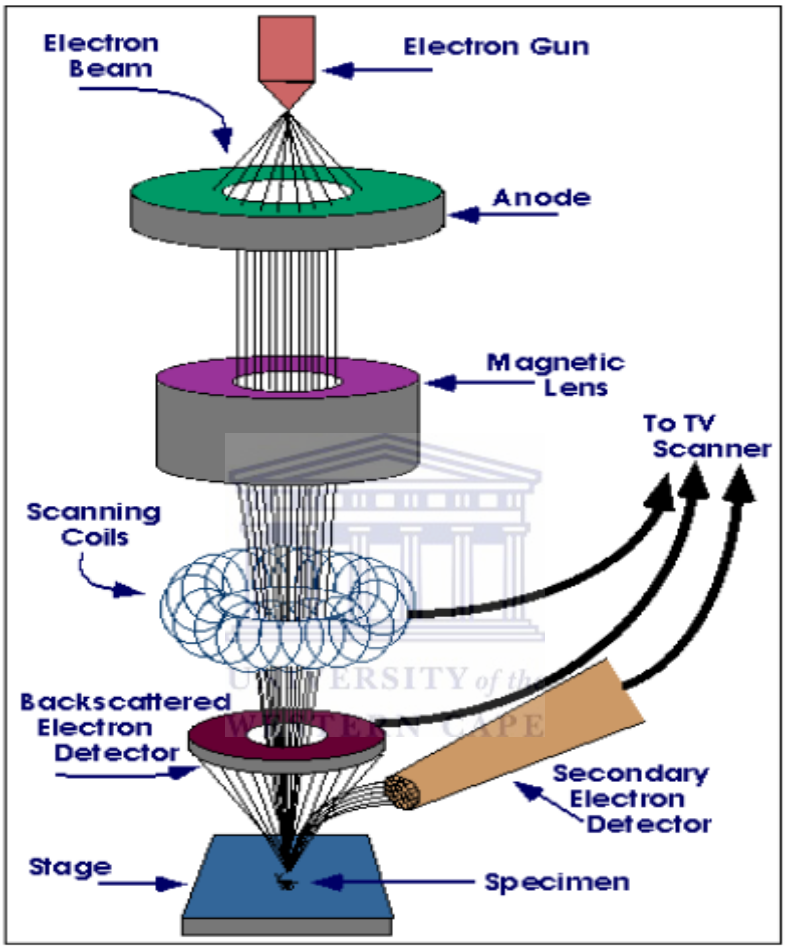

Figure 3.1: Basic operating principles of HRSEM [79].

3.3.1.1.2 High-Resolution Transmission Electron Microscopy

HRTEM is also a powerful tool used for the characterisation of materials at the nanoscale and it is indispensable for nanotechnology. Even though scientists have been examining "small particles" nowadays called nanoparticles, it was until the early 1990's that inventions of various scanning probe microscopy allowed scientists to manipulate at the nanoscale. And apparently, atom-by-atom engineering provided by the HRTEM is the state of the art for nanoscience [80]. In HRTEM, the electron beam interacts and passes through the specimen. The electron beam

is condensed by a condenser lens which controls the brightness of the beam, and the beam passes through the condenser aperture and interacts with the specimen. Electrons that did not lose energy during the electron-sample interaction are transmitted as elastically scattered electrons, forming a transmitted beam which passes an objective lens, aperture and magnifying system. A magnified image is then displayed on a flourescent screen or charge-coupled device (CCD) camera system.

HRTEM is capable of imaging at a significantly higher resolution than light microscopes owing to the small de Broglie wavelength of electrons. It offers resolution to the angstrom level and enables information about the structure and even atomic packing to be obtained with particle sizes as low as 1 nm. HRTEM has been used by many researchers for obtaining the internal structures of nanomaterials and to reveal defects in solid using electron diffraction patterns. HRTEM also allows for imaging of crystal structures; that is inter-planar spacing between planes of atoms.

In this study, HRTEM was used to obtain the internal ultra-structure, crystallinity (lattice fringes) and the elemental composition of the synthesized nanomaterials. HRTEM analysis were performed by casting a drop of the synthesized material on a copper-nickel grid and dried under a lamp to evaporate the solvent for 15 min. Analysis were performed using a Tecnai G^2F_2O X-Twin MAT 200 kV field emission TEM from FEI (Eindhovea, Netherlands).

3.3.1.2 Spectroscopic characterisation by FTIR, XRD, SS-NMR and XPS and instrumentation used

3.3.1.2.1 Fourier-Transform Infra-Red Spectroscopy

FTIR is a versatile tool for measuring the infrared spectra of solids and liquids. In principle, it uses an optical element composed of an interferometer, instead of a monochromator to allow simultaneous measurements of a complete region of wave numbers in a short time span [81]. Basically this spectroscopy requires that the sample of interest be placed onto an internal reflection element (IRE). The IR beam from the spectrometer is directed onto the element at an angle that enables the infrared light to undergo internal reflection. At each point of internal reflection, an evanescent wave is produced, from which the radiation can be absorbed by a

sample placed in direct contact with the IRE. The absorption of the infrared light which is proportional to the path length can then be measured using standard infrared detectors [82]. In this study, FTIR spectroscopy was used to confirm the functional groups present in the synthesized pristine and novel nanostructured cathode materials. FTIR spectra were obtained using a Perkin Elmer Spectrum 100 series Attenuated Total Reflection (ATR) FTIR spectrometer.

3.3.1.2.2 X-ray Diffraction

X-ray diffraction is a non-destructive analytical technique that operates at the nanoscale based on elastic scattering of X-rays from structures that have long range order (an organised structure of some sort, such as in a crystal or polymer). It can be used to identify and characterise a diverse range of materials, such as metals, minerals, polymers, catalysts, plastics, pharmaceuticals, proteins, thin-film coatings and ceramics. Crystalline materials are characterised by orderly periodic arrangements of atoms whereby the basic repeating unit (unit cell) defines the crystal. Parallel planes of atoms (crystallographic planes) intersecting the unit cell are used to define directions and distances in the crystal. These planes are identified by Miller indices. X-ray diffraction is based on constructive interference of monochromatic X-rays and a crystalline sample. These X-rays are generated by a cathode ray tube, filtered to produce monochromatic radiation and directed towards the sample. The interaction of the incident rays with the sample produces constructive interference (and a diffracted ray) when conditions satisfy Bragg's Law: $n\lambda=2d\sin\theta$ [83].

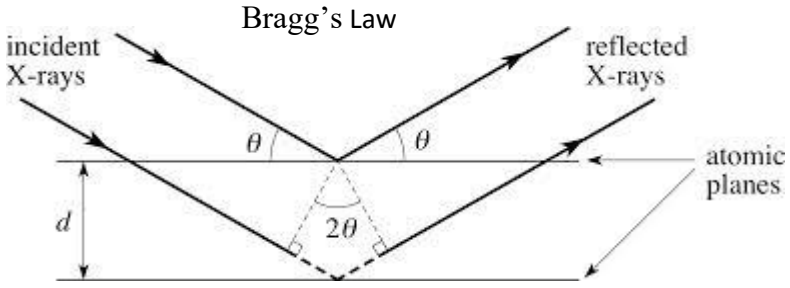

Sheme 3.2: A typical representation of Bragg's law.

Diffraction from different planes of atoms produces a diffraction pattern (recorded by a detector) which provides information about the atomic arrangement within the crystal (crystal structure). XRD has been used by many researchers to determine the phase composition of a materials, crystallite size, microstrain, unit cell lattice parameters. In this study, XRD was used to obtain the crystalline pattern, phase purity, crystallite size and lattice parameters of the synthesized nanostructured materials. XRD measurements were taken with a D8 Advanced diffractometer from BRUKER AXS using an X-ray tube with copper K-alpha radiation operated at 40 kV and 40 mA and a position sensitive detector Vantec_1 which enables fast data acquisition. Measurements were taken in the 2 theta range of 10^{o}- 80^{o} with a step size of 0.028^{o}.

3.3.1.2.3 Solid-State Nuclear Magnetic Resonance Spectroscopy

SS-NMR is a well-established and accurate technique for the characterization of the atomic environments occurring in a broad range of materials. It is widely used to probe the molecular structure and dynamics in condensed matter. The position and line shape of a NMR signal represents the local electronic structure of the nucleus, which is very sensitive to its environment and depends on the spin Hamiltonian [84]. The total interaction energy of a nucleus can be seen as the result of the sum of the all the individual contributions experienced by the nucleus. These interactions are represented in the total Hamiltonian [85].

$$H_{tot}=H_z+H_{RF}+H_{Cs}+H_D+H_J+H_Q+\mathbf{H_p}+H_{exp} \quad (3.1)$$

Where H_Z is the Zeeman interaction between the nucleus and the external field, H_{RF} is the interaction between the nucleus and the applied RF pulse, H_{Cs}, the chemical shielding defining the interaction between the nucleus and the local change in the magnetic field due to changes in electron density, H_D, the dipolar coupling trough space between two nuclei, H_J, the indirect spin coupling that defines the interaction trough bonds of the nuclei, H_Q, the electric quadrupole interaction that affects the Zeeman energy level, $\mathbf{H_P}$, the interaction with unpaired electrons. H_{exp} accounts for experimental in homogeneities and other minor sources of local fields.

Besides the more conventional applications of the NMR technique, paramagnetic phases which is the area of interest for this study, presents particular difficulties because of the presence of strong electron-nuclear interactions that broaden and shift the nuclear magnetic resonances far beyond their normal chemical range, thus complicating both the acquisition and assignment of the spectra. The major shift contribution of relevance is the Fermi contact arising from the prevalence of the low density of unpaired electrons directly at the nucleus of the NMR-observed centre ($^{6/7}$Li, ^{31}P) [86].

Paramagnetic NMR spectra when interpreted, offer a wealth of insight into the local environment and processes occurring in a wide range of technologically important materials. Areas of application include; positive electrodes for Li-ion batteries and other electrochemically active species, environmentally relevant phases such as iron oxides, oxyhydroxides, orthophosphates and silicates, paramagnetic complexes and materials for spintronics and advanced storage [86]. Most of which are paramagnetic due to the presence of open-shell cations within their lattices. In this study SS ^{7}Li-NMR was used to study the local order of the lithium nuclei (cations) in the synthesized lithium manganese orthosilicate systems, and to explore the structural and electronic properties that are responsible for the large shifts observed in these materials.

Solid-state ^{7}Li magic angle spinning (MAS) NMR spectra were recorded on a 500 MHz Bruker Avance III HD equipped with a 4mm MAS BB/1H/19F probe, operating at a ^{7}Li Larmor frequency of 194.3 MHz. One pulse and Hahn-echo experiments were conducted with scans between 200 and 20000, and 600 and 20000 respectively. In the ^{7}Li-MAS one pulse experiments, a spinning speed of 10 and 15 kHz with a sweep width of 989.5 ppm, and the delay between consecutive scans was set at 0.05s. Whereas for ^{7}Li-MAS Hahn-echo experiments, a spinning speed of 15 kHz with a sweep width of 2500 ppm, and delay time of 0.05s were used.

3.3.1.2.4 X-ray Photoelectron Spectroscopy

XPS is an important and widely used surface analytical technique in many fields of Chemistry and Physics including; microelectronics, catalysis and geochemistry. It is sensitive to all

elements except hydrogen and helium, and has a detection limit of ~ 0.1% of a monolayer. XPS is capable of determining nondestructively (in many cases), the surface composition and electronic environment of the sample under study. XPS operates based on the principle of the photoelectric effect, whereby, a sample is irradiated with x-rays producing electrons (photoelectrons) with discrete energy carrying chemical information on the surface of the analyte [87]. Photoelectrons are generated through ejection from the solid surface upon excitation of core level orbitals electrons by a photon source as shown by Equation 3.2 below.

$$A + h\nu \rightarrow A^{+*} + e^{-}(\text{photoelectron}) \qquad (3.2)$$

Where A is the neutral atom or molecule, A^{+*} is the excited ion and e^{-} is the ejected photoelectron. XPS owes its nondestructive nature to the fact that only the ejection of electrons is required for analysis. Unlike other techniques of elemental analysis, the atomic nuclei being examined remain unchanged during electron spectroscopic measurements [87]. The x-ray photoelectron spectrum is represented as a plot of the counting rate versus the binding energy of the detected photoelectrons and the spectral peaks are named after the orbital (l = 0, 1, 2, 3… denoted as s, p, d, f…) and spin ($s = \pm ½$) quantum numbers from which they exude. The total momentum of the photoelectrons ($J = l \pm s$) is also included in naming the spectral peak [87]. XPS was used in this study to investigate the surface chemistry and electronic environment of the synthesized pristine and novel Li_2MnSiO_4 nanostructured cathodes.

The XPS analyses were carried out with a PHI 5400 XPS spectrometer using a non monochromatic Al K_α X-ray source (15 kV, 300 W) and hemispherical sector analyzer. The instrument work function was calibrated to give a binding energy (BE) of 83.96 eV for the Au $4f_{7/2}$ line for metallic gold and the spectrometer dispersion was adjusted to give a BE of 932.67 eV for the Cu $2p_{3/2}$ line of metallic copper. Survey scan analyses were carried out with pass energy of 178.95 eV and scan rate of. 2.5 eV/s. High resolution analyses were carried out with pass energy of 44.75 eV and scan rate of 0.625 eV/s. Charge correction was done by referencing to the C-C peak at 284.7 eV. Spectra were analyzed using XPS PEAK 4.1 software. A Shirley background was used and the powders were mounted on adhesive vacuum carbon tape.

3.3.2 Electrochemical Characterisation techniques and instrumentation used

Electro-analysis to study the electron transfer processes, kinetic and thermodynamic aspects, and oxidation-reduction (redox) behaviour of the electro-active species present in the pristine and novel cathode materials were performed using cyclic voltammetry, square wave voltammetry and electrochemical impedance spectroscopy.

3.3.2.1 Cyclic Voltammetry (CV)

CV belongs to the category of linear sweep voltammetric experiments. It is the most useful technique for the determination of the redox properties and electrochemical kinetics of a given species at the electrode surface. CV is based on perturbing the initial zero-current condition of an electrochemical cell by imposing a change in the potential of the working electrode and observing the outcome of the generated current as a function of time. The applied potential is varied in both the forward and reversed directions at a certain scan rate. That is, the applied potential is varied from an initial point E_i to a final point E_f at a constant scan rate (single sweep voltammetry). Once the value of the E_f is reached, the direction of the scan rate can be reversed, maintaining the same scan rate and the potential brought back to the initial value (cyclic voltammetry) [88]. The concentration of the electro-active species is directly proportional to the observed current. Different redox systems can be obtained depending on the outcome of the diagnostic test. These include; reversible, quasi-reversible and irreversible.

An electrode process is defined as electrochemically reversible when the rate of the electron transfer process is higher than the rate of the mass transport. Figure 3.2 below represents a typical cyclic voltammograms of an electrochemically reversible process.

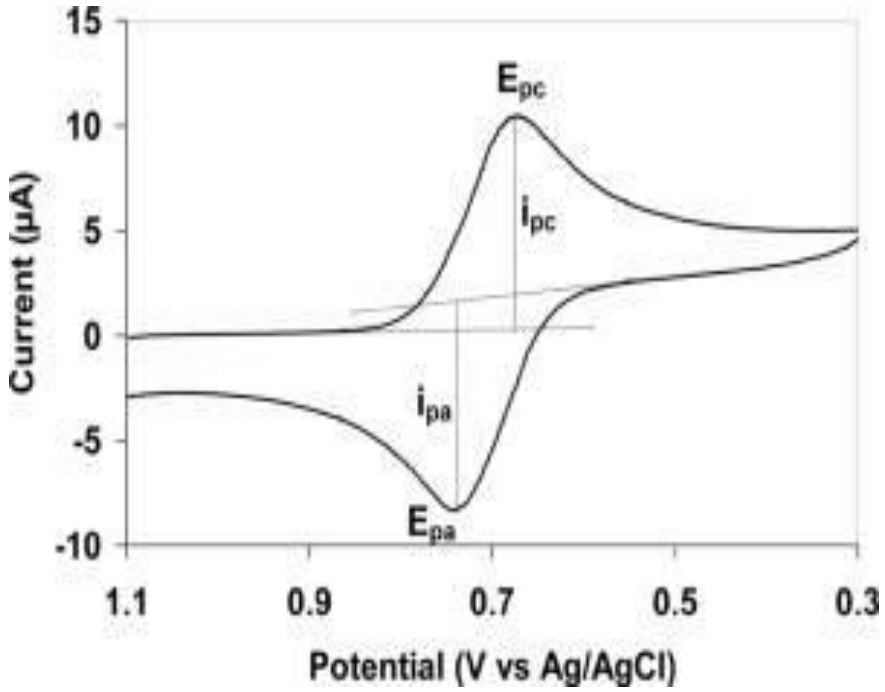

Figure 3.2: A typical cyclic voltammogram for an electrochemically reversible system.

From the cyclic voltammogram above, key parameters such as the magnitude of the anodic peak current (I_{pa}), cathodic peak current (I_{pc}) and their corresponding potential peak values E_{pa} and E_{pc} can be obtained. These parameters can further shed more light on the reversibility and electron transfer kinetics of the system.

When the scan of the potential reaches a value suitable for the reduction of the anodic species, the concentration of the anodic specie at the electrode surface begins to decrease with respect to that present in the bulk solution. This implies that a concentration gradient becomes established and according to Fick's law, a current begins to flow. The peak current for a reversible system is given by the Randles-Sevcik equation [88]:

$$I_p = 2.69 \times 10^5 n^{3/2} A D_0^{1/2} C_0 \nu^{1/2} \quad (3.3)$$

where I_p is the forward peak current in amperes (A); n is the number of electrons exchanged per molecule of the anodic species; A is the area of the electrode (cm^2); D_0, the diffusion coefficient ($cm^2\ s^{-1}$); C_o, concentration ($mol\ cm^{-3}$) and ν, the scan rate ($V\ s^{-1}$).

The peak-to-peak separation (ΔE_p) in an electrochemically reversible process which is the separation between the anodic and cathodic peak potentials is given by

$$\Delta E_p = E_{pa} - E_{pc} = \frac{59}{n} \quad (3.4)$$

Also, the formal potential (E°) is usually obtained from the average of the peak potentials, that is;

$$E^\circ = \frac{E_{pa} + E_{pc}}{2} \quad (3.5)$$

For an electrochemically irreversible process, the rate of electron transfer is lower than that of the mass transport, the peak potentials depend on the scan rate and gradually shift from the formal potential as the scan rate increases [88]. The peak current for an irreversible process is given by

$$I_p = 2.69 \times 10^5 \alpha^{1/2} n^{3/2} A D_0^{1/2} C_0 \nu^{1/2} \quad (3.6)$$

where I_p is the forward peak current in amperes (A); α, is the transfer coefficient; n, the number of electrons exchanged per molecule of the anodic species; A, the area of the electrode (cm^2); D_0, the diffusion coefficient ($cm^2\ s^{-1}$); Co, concentration (mol cm^{-3}) and ν, the scan rate (V s^{-1}).

For a quasi-reversible system, the electron transfer processes behave reversibly at lower scan rates and irreversibly at higher scan rates, these processes occur at the transition zone between reversible and irreversible behaviour. A quasi-reversible process occurs when the rate of the electron transfer is of the same order of magnitude as the mass transport [88].

3.3.2.2 Square Wave Voltammetry (SWV)

SWV is a pulse voltammetric technique which offers high sensitivity, and a lower detection limit compared to the linear sweep voltammetric techniques. SWV combines a large square wave modulation with a stair case waveform and describes the current response in terms of a normalized current function which is more accessible at higher scan rates. The peak-shaped voltammograms obtained display excellent sensitivity. For a simple reversible electrochemical process, the current function depends only on the potential sequence applied to the electrode and is independent of time. The peak height is directly proportional to the concentration of the electro-active species and the peak current is given by equation 3.7 below [89].

$$I_p = \left[nFAD^{1/2}C^b/\sqrt{\pi t_p}\right] \varphi\ (\Delta E_s, E_{SW}) \qquad (3.7)$$

Where I_p is the peak current measured on each pulse; n is the number of electrons transferred; F is the Faraday constant; A is the area of the electrode; D is the analyte diffusion coefficient; C^b is the bulk concentration of the analyte; t_p is the pulse width (half the staircase period); Ψ is the dimensionless current function, which depends on the step height (E_s) and the square wave amplitude E_{SW}. When the normalized current function is plotted against the normalized potential, n (E - $E_{1/2}$), the resulting voltammogram is independent of the pulse width and concentration of the analyte as represented by Figure 3.3 below.

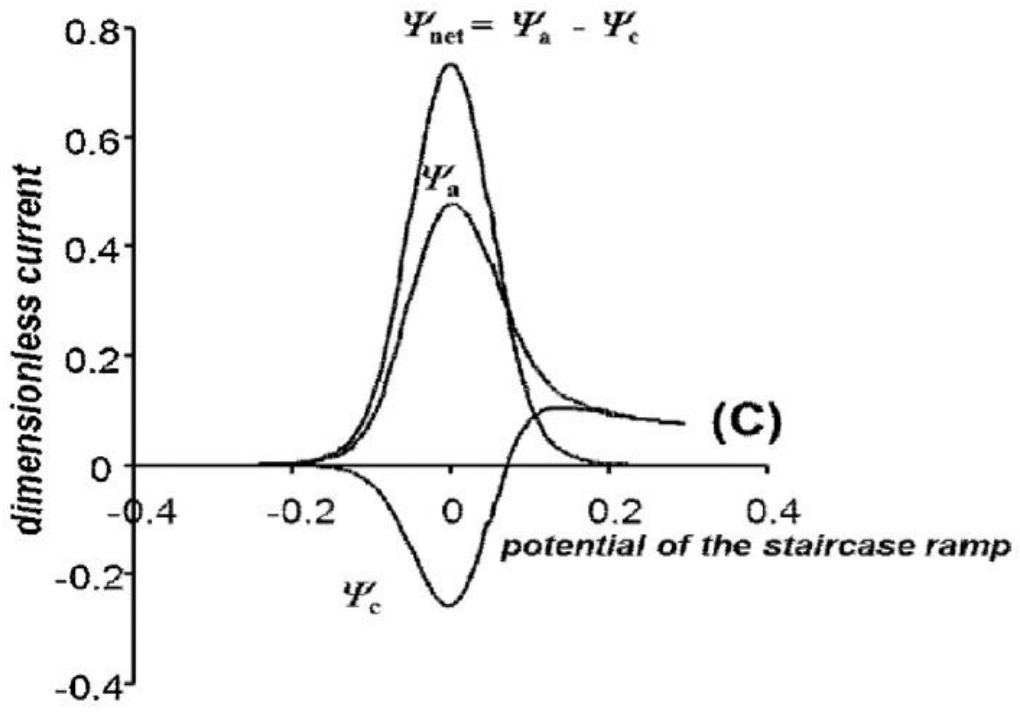

Figure 3.3: A typical square wave voltammogram consisting of a forward (anodic, Ψ_a) backward (cathodic, Ψ_c) and the net current (Ψ_{net}).

Cyclic voltammetric and square wave voltammetric experiments were carried out using a BAS Epsilon integrated and automated electrochemical work station from Bio Analytical systems (BSA) Lafayette, USA. All voltammograms were recorded with a computer interfaced to the Epsilon electrochemical work station. A 10 mL electrochemical cell with the conventional three electrode set up was used. The glassy carbon electrode was used as the working electrode, the platinum wire as the counter and the Ag/AgCl stored in 3 M NaCl was used as the reference electrode.

3.3.2.3 Electrochemical Impedance Spectroscopy

EIS is a technique used to characterize electrode processes and complex interfaces. It is based on applying an alternating current (AC), potential (E) of a small amplitude (perturbation), and obtaining an AC current signal (I) in which the impedance (Z) can be obtained [90]. Where:

$$E(t) = E_0 \cos\ (\omega + t) \qquad (3.8)$$

$$I(t) = I_0 \cos(\omega t - \varphi) \quad (3.9)$$

$$Z = {}^{E(t)}\!/_{I(t)} \quad (3.10)$$

EIS measurements are carried out at different AC frequencies with a typical frequency range of 0.5 Hz to 100 kHz. These analyses allow for the characterisation of the double layer interface of the electrodes and the physicochemical processes at various time constants, simplifying electron transfer at high frequency and mass transfer at low frequency. Results obtained from EIS are usually fitted using equivalent circuits of resistors and capacitors such as the Randles circuit model [90]. EIS data is either represented as the Nyquist plot; which is the plot of the real impedance (Z_{Re}) versus the imaginary impedance (Z_{Im}) or the Bode plot; where the modulus of the impedance (log /Z/) and the phase angle Ψ between the AC potential and the AC current as a function of the frequency (log ω) are plotted [90]. The Nyquist plot (figure 3.5 below) provides visual insights into the system dynamics at the electrochemical interface. The plot consists of a semicircle at high frequency which describes the electron transfer process at the electrode interface (charge transfer resistance) and a linear region at lower frequencies known as the Warburg impedance which arises from mass transfer limitations and can be used to calculate apparent diffusion coefficients. The Bode plot (Figure 3.6 below) shows frequency independent plots which represent the behaviour of resistive, capacitive or diffusive processes [90].

EIS is a versatile tool used to probe the interfacial properties in batteries, fuel cells, semiconductor electrodes, polymers and coatings. In this study, EIS was employed to explore the electron transfer kinetics/dynamics, and to establish the diffusive processes occurring at the electrode/electrolyte interfaces of the pristine Li_2MnSiO_4 and the novel Li_2MnSiO_4/Al_2O_3 cathode materials. EIS measurements were recorded using the CH Instruments, Inc Electrochemical work station, 600 E Potentiostat from USA. A conventional three electrode system as used in voltammetric studies was also employed for these measurements.

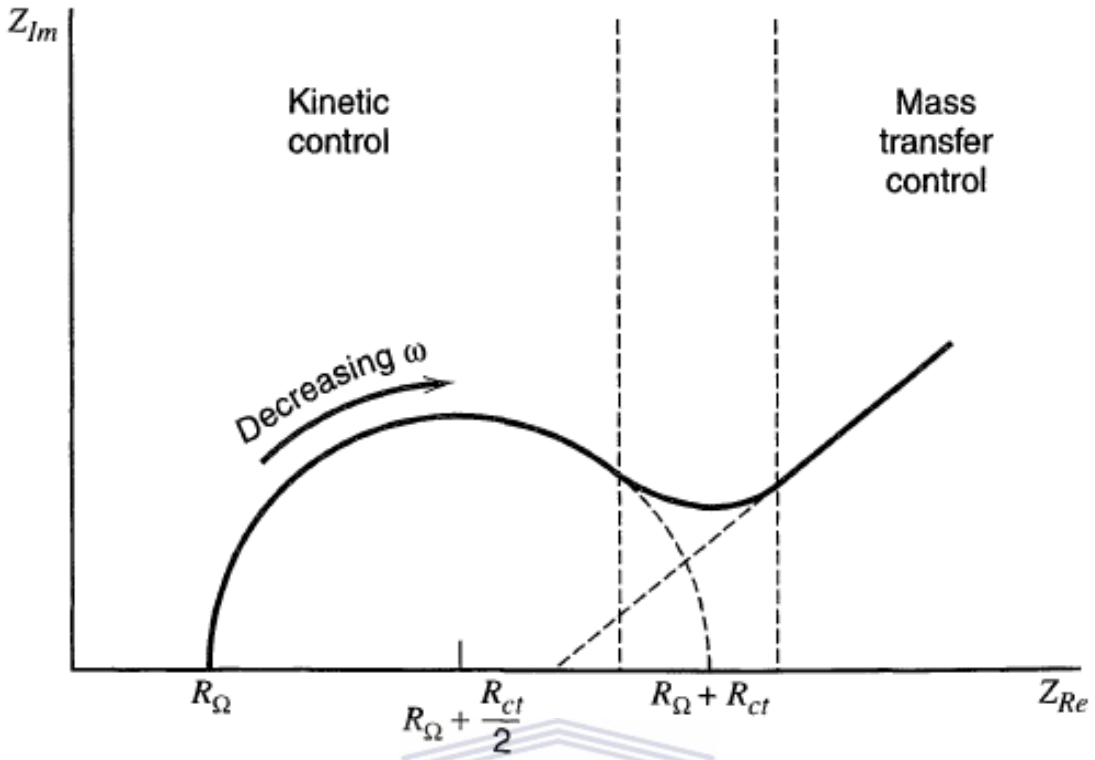

Figure 3.4: A typical Nyquist plot.

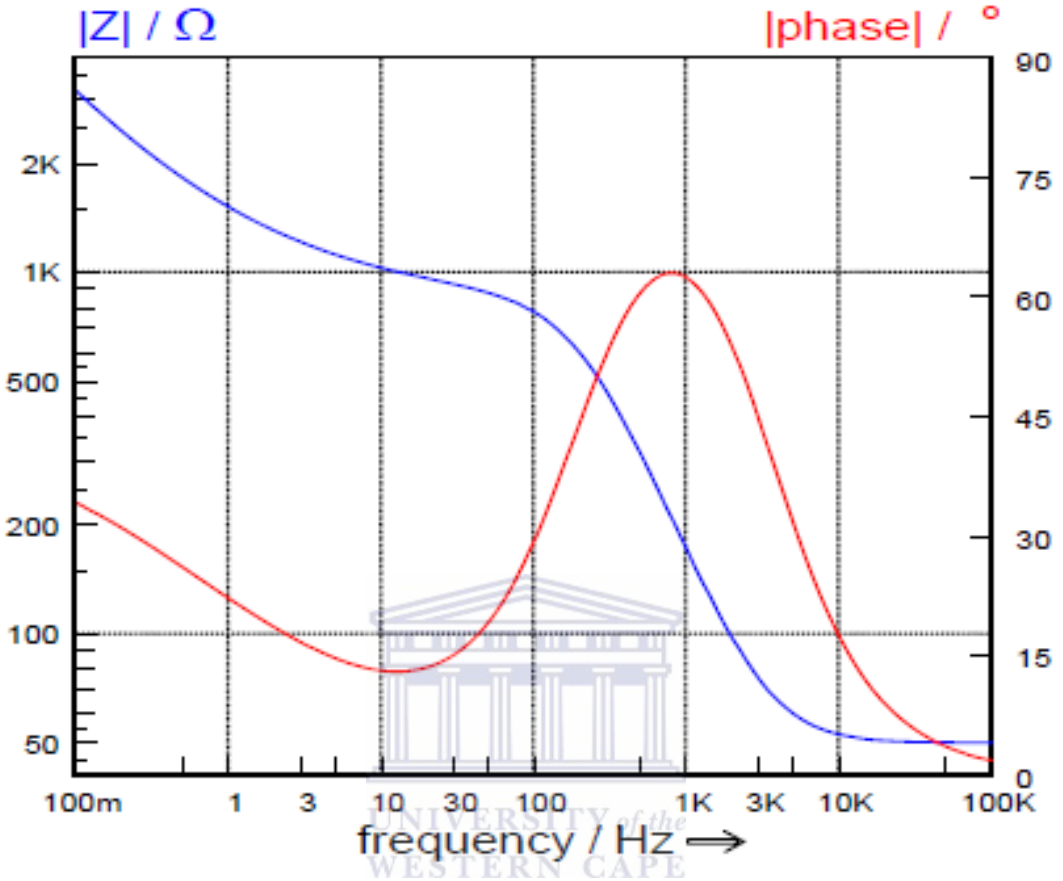

Figure 3.5: A typical Bode plot.

CHAPTER 4

Chapter Overview

This chapter discusses the characterisation of nanostructured pristine Li_2MnSiO_4 and novel Li_2MnSiO_4/Al_2O_3 cathode materials by microscopic (HRSEM and HRTEM), and spectroscopic (FTIR, XRD, SS-NMR, XPS) techniques. It further discusses the electro-analysis of these cathode materials by analytical techniques such as CV, SWV and EIS.

4.0 RESULTS AND DISCUSSION

4.1 Microscopic Techniques

4.1.1 High-Resolution Scanning Electron Microscopic Studies

HRSEM was used to obtain the surface morphology, particle size distribution and elemental composition/distribution of the synthesized pristine Li_2MnSiO_4 and novel Li_2MnSiO_4/Al_2O_3 nanostructured cathode materials. The conditions for obtaining the HRSEM images were discussed in chapter 3. Figure 4.1 below shows the HRSEM image of pristine Li_2MnSiO_4 cathode material. The nanoparticles consist of roughly uniform aggregated spherical morphologies with particle sizes in the range of 21- 90 nm and an average diameter of 53 nm, with a standard deviation of 18.5 nm. The particle sizes were calculated using a Java-based image processing program known as “ImageJ”. The diameter of each primary particle was defined as the length of the line which bisected the image of the particle and was fixed for all measurements and the values were analyzed numerically.

X-ray maps were obtained to determine the elemental distribution of the pristine Li_2MnSiO_4 cathode (Mn, Si and O). Figure 4.2 below represents the electron image (a) obtained by bombarding the sample with a high energy source in order to eject all electrons present in the sample, (b) is the layered image showing elemental distribution and (c), (d) and (e) are the corresponding oxygen, silicon and manganese maps.

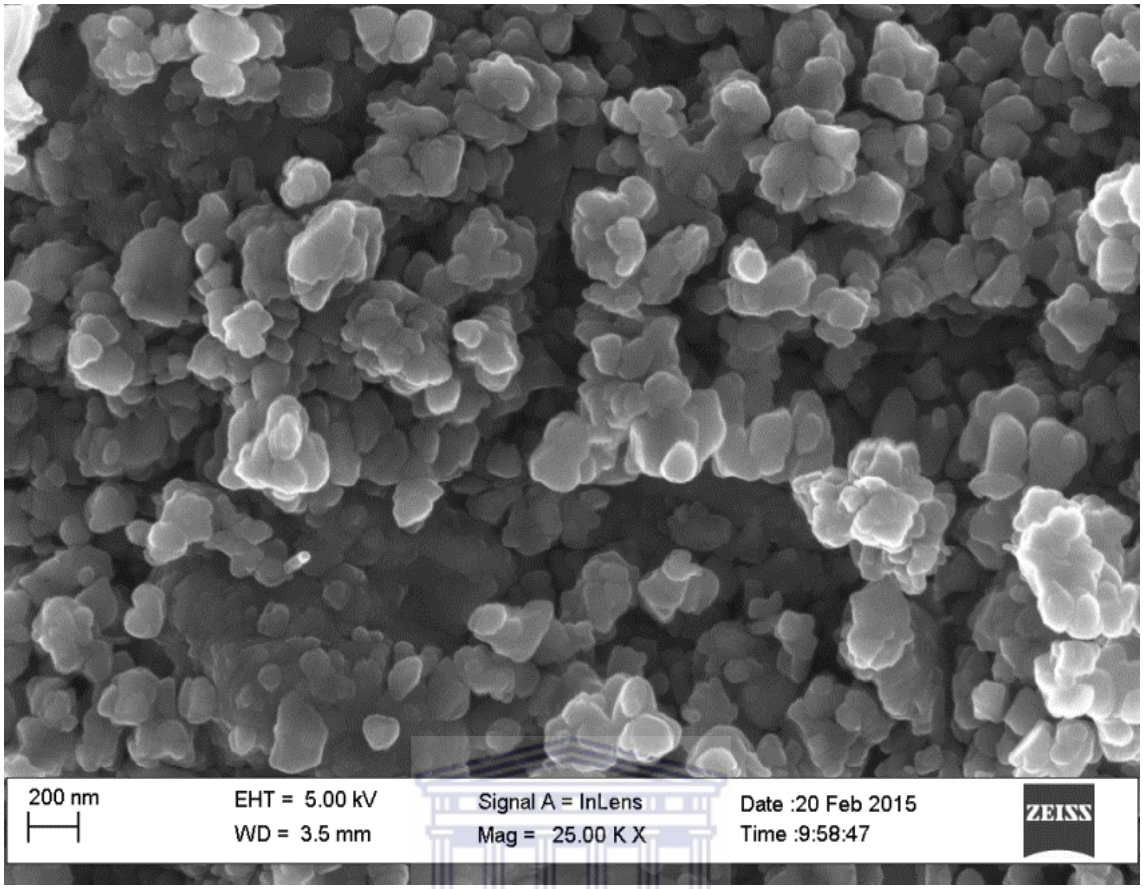

Figure 4.1: HRSEM image of pristine Li_2MnSiO_4 cathode material at the scale view of 200 nm.

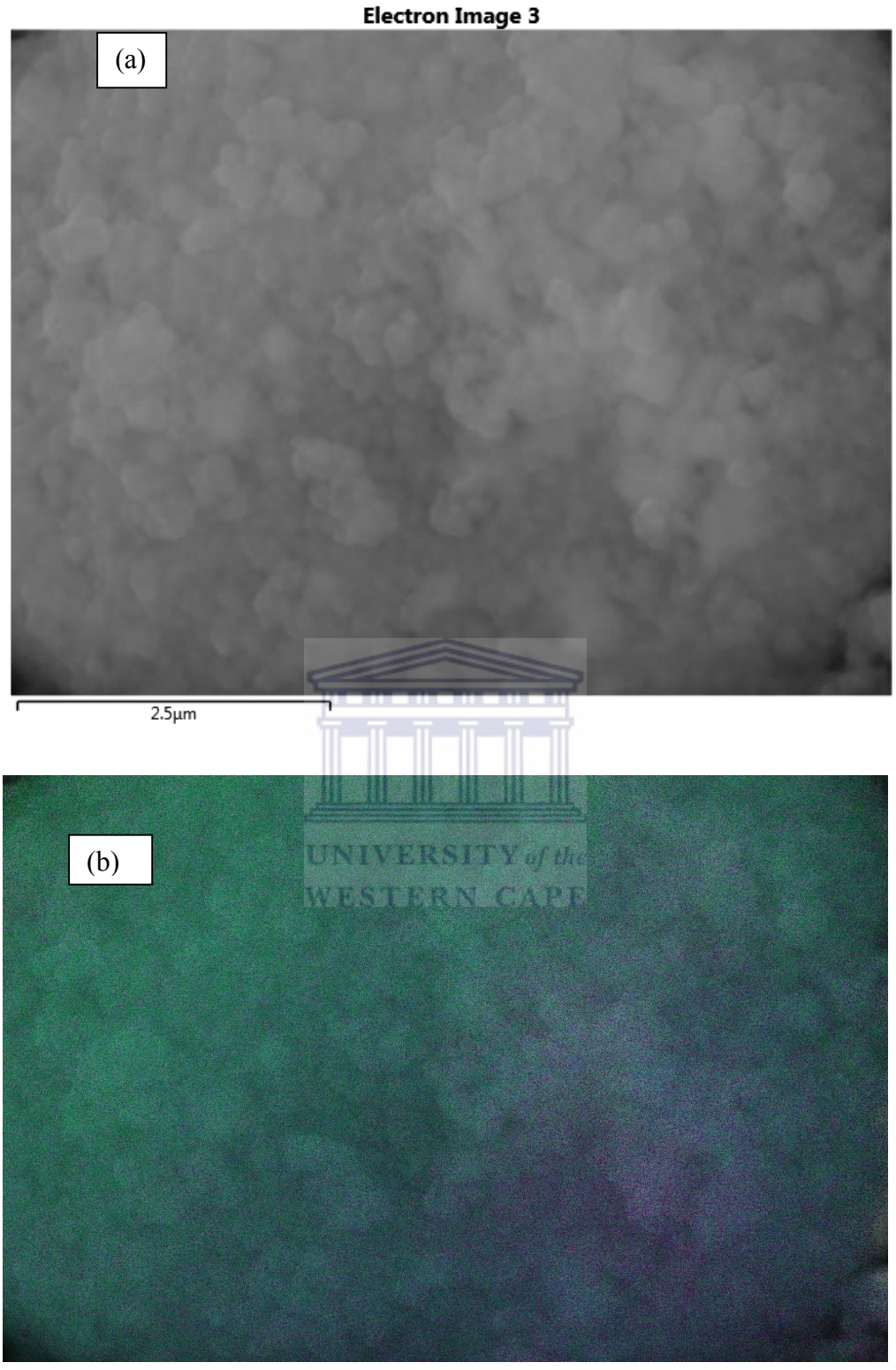

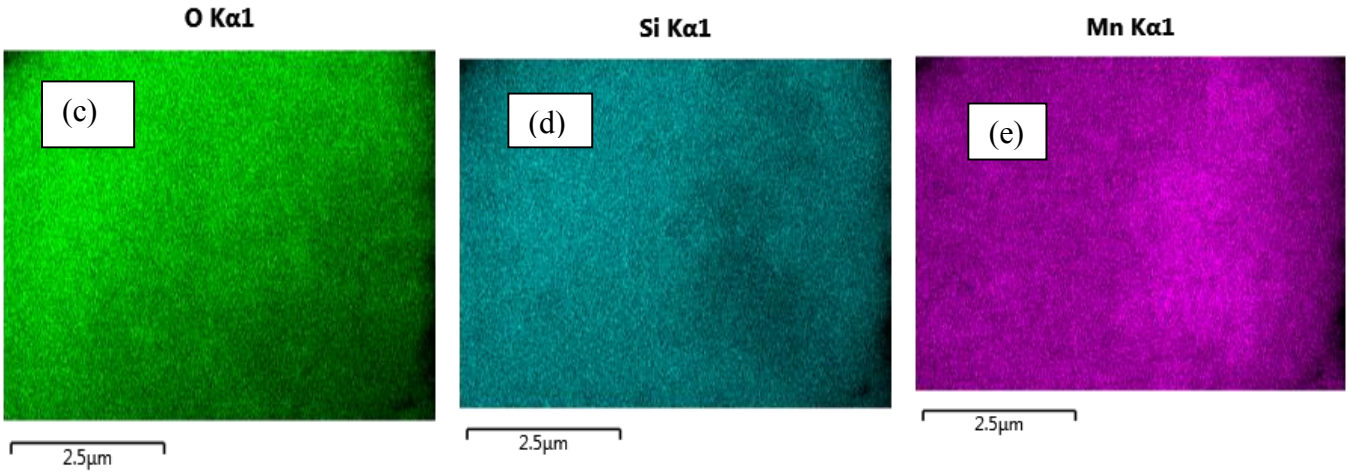

Figure 4.2: Elemental distribution of pristine Li_2MnSiO_4 cathode material; (a), Electron image, (b), layered image, (c), (d), and (e), the corresponding X-ray maps for O, Si, and Mn.

Figure 4.3 below shows the EDX spectra of the pristine Li_2MnSiO_4 cathode material confirming elemental composition. All expected elements are observed, with gold and palladium coming from the conductive alloy coated on the nanoparticle surface during the HRSEM analysis and carbon coming from the carbon black adhesive used on the sample holders during the analysis.

From the HRSEM micrograph of the novel Li_2MnSiO_4/Al_2O_3 cathode material (Figure 4.4 below), it can be observed that the morphology of the particles of the pristine and novel cathode materials are very similar, which indicates that the pristine cathode material approximately retains its uniform spherical morphology after addition of the Al_2O_3 precursor.

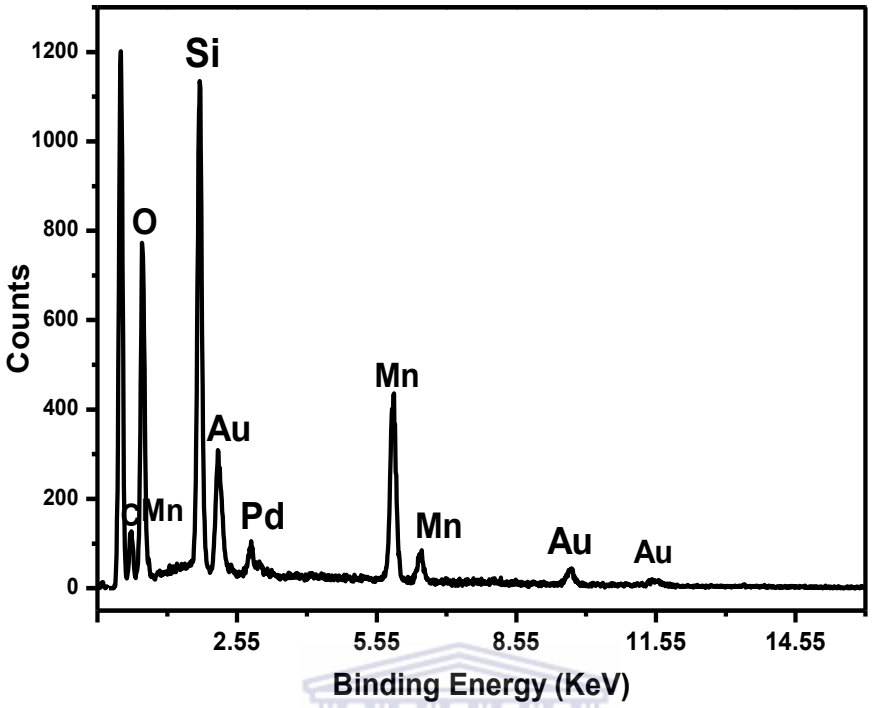

Figure 4.3: EDX spectra of pristine Li_2MnSiO_4 nanoparticles obtained from HRSEM.

Table 4.1: Elements and their corresponding weight percentages obtained from the EDX of the pristine cathode material

Element	Weight %
C	8.94
O	41.03
Si	16.11
Mn	19.75
Pd	3.13
Au	11.04

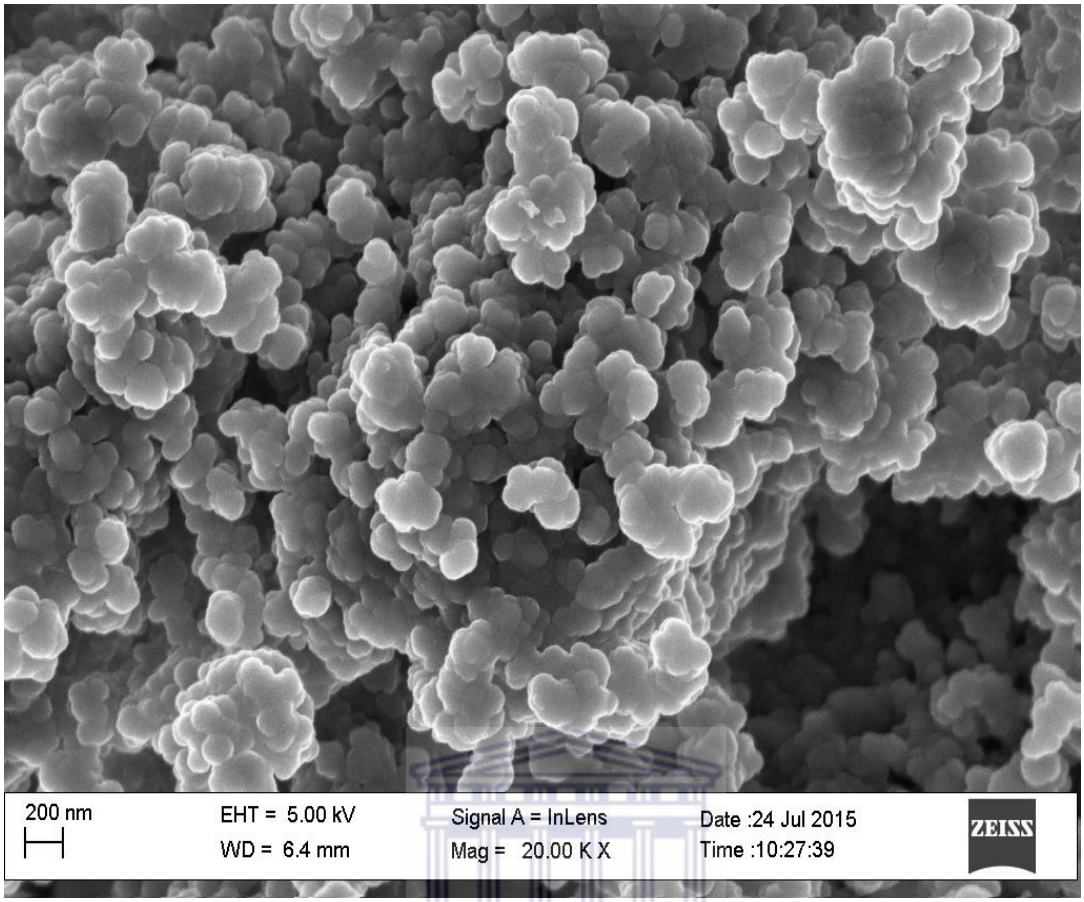

Figure 4.4: HRSEM image of novel Li_2MnSiO_4/Al_2O_3 cathode material at the scale view of 200 nm.

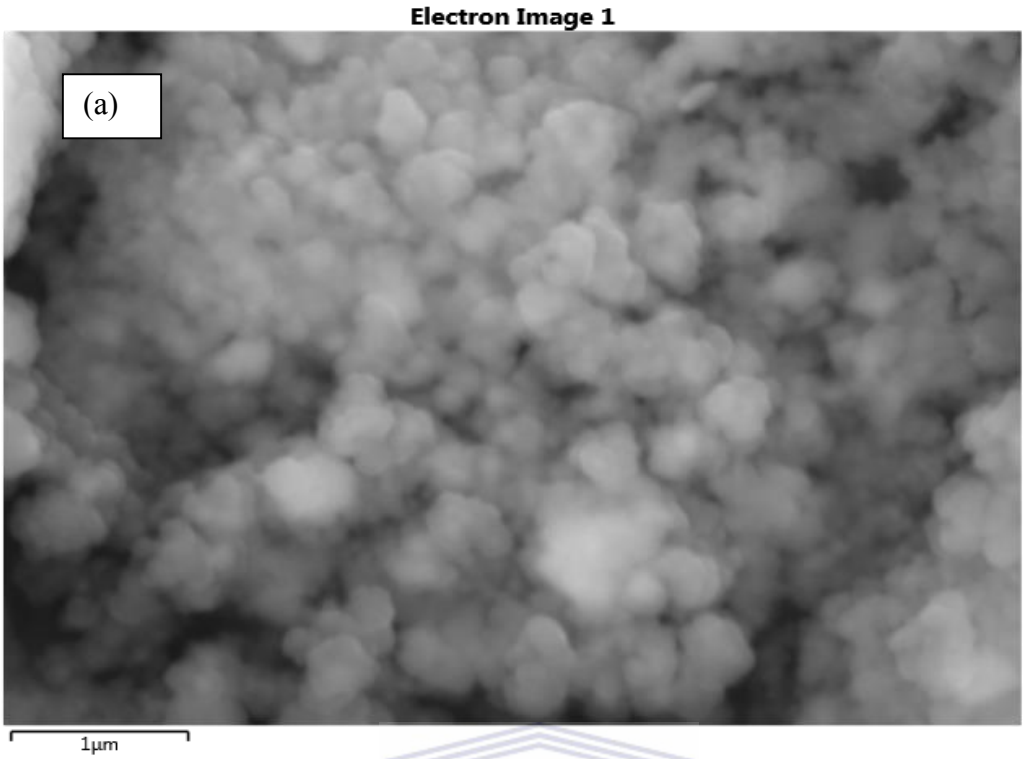

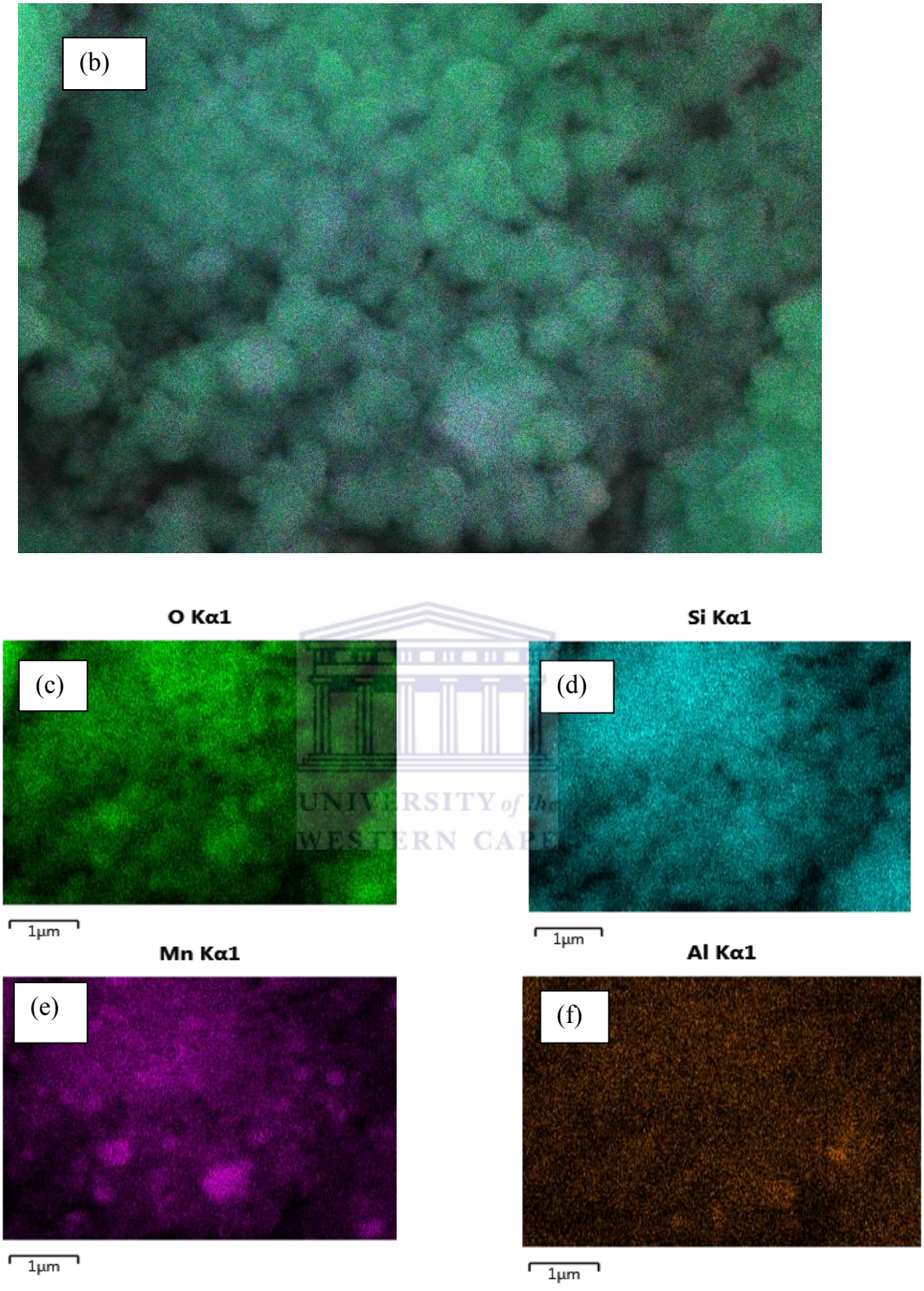

Figure 4.5: Elemental distribution of novel Li_2MnSiO_4/Al_2O_3 cathode material: (a), Electron image, (b), layered image and (c), (d), (e), (f), the corresponding x-rays maps for O, Si, Mn, and Al.

The elemental distribution maps for the novel cathode material show an evenly distribution of the particles of the constituent elements (O, Si, Mn and Al) over the enitire sample. This uniform distribution of elements is expected to provide fast removal and insertion of Li^+ ions from and into the novel nanostructured (Li_2MnSiO_4/Al_2O_3) crystalline structure [91]. Figure 4.6 below shows the EDX spectra of novel nanostructured Li_2MnSiO_4/Al_2O_3. All elements are represented with an increase in the oxygen peak as compared to the pristine cathode material, and the presence of an aluminium peak, though minor due to the amount of the aluminium oxide content present (0.84 weight %). Thus indicating complete coverage of the pristine material with an aluminiun nanofilm.

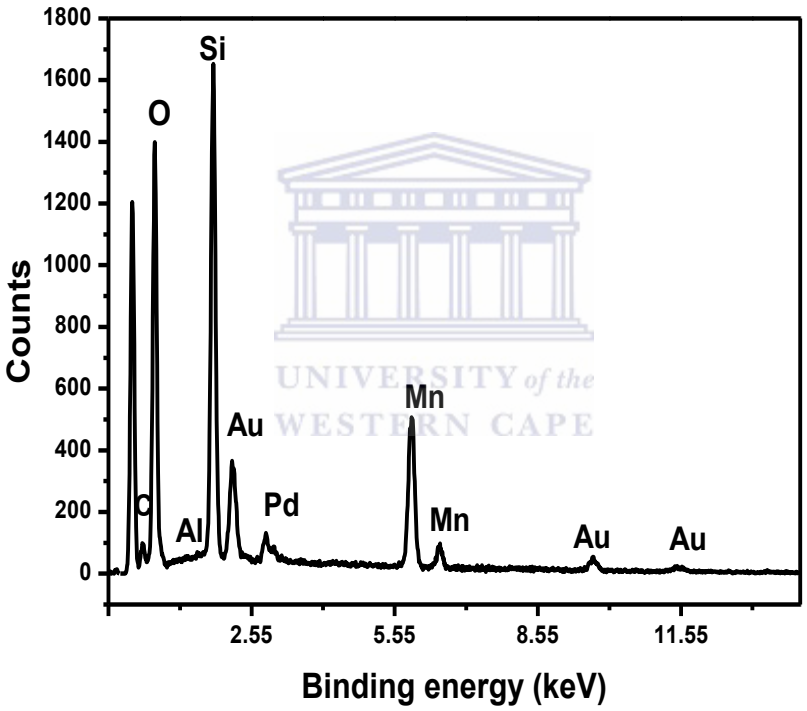

Figure 4.6: EDX spectra of novel Li_2MnSiO_4/Al_2O3 cathode material obtained from HRSEM.

Table 4.2: Elements and their corresponding weight % obtained from the EDX of the novel nanostructured cathode material

Element	Weight %
C	7.11
O	53.87
Al	0.83
Si	16.63
Mn	15.72
Pd	2.13
Au	3.71

4.1.2 High-Resolution Transmission Electron Microscopic Studies

HRTEM was used to obtain the internal ultra-structure, crystallinity (observed from the lattice fringes) and further confirming the elemental composition of the pristine and novel nanostructured cathode materials. Figures 4.7 (a-d) below represents the HRTEM micrographs with the lattice fringes of the pristine and novel nanostructured cathode materials. The particles consist of spherical morphologies which are consistent with the results obtained from HRSEM studies.

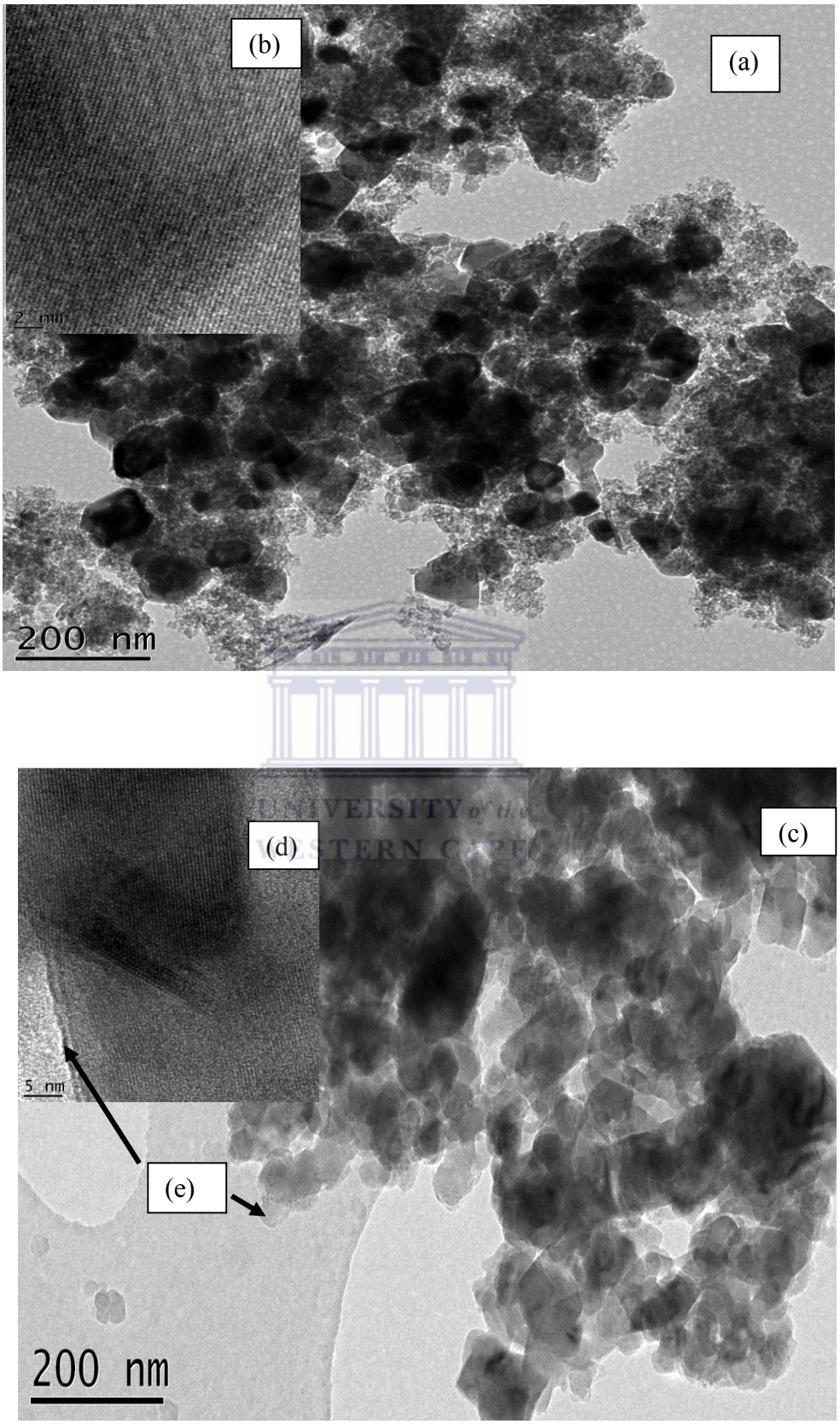

Figure 4.7: HRTEM micrographs of the pristine Li_2MnSiO_4 (a) and novel nanostructured Li_2MnSiO_4/Al_2O_3 (b) cathode materials at the scale view of 200 nm.

The lattice fringes are represented as inserts on image (a) and (b) above, and give clear information on the crystallinity of the nanostructured cathode materials. The very flawless lattice fringes show that both the pristine and novel nanostructured cathode materials possess good crystallinity. A nano-amorphous layer (e) is observed on the lattice fringes of the novel nanostructured cathode material, thus further confirming the presence of an alumina nanofilm in Li_2MnSiO_4/Al_2O_3 cathode material. The EDX spectra of pristine Li_2MnSiO_4 and novel Li_2MnSiO_4/Al_2O_3 are shown by Figures 4.8 and 4.9 below. All expected elements are observed, with copper coming from the grid used for the analysis and carbon from the carbon black adhesive used on the sample holders. No other impurity elements were observed, indicating the purity of the materials.

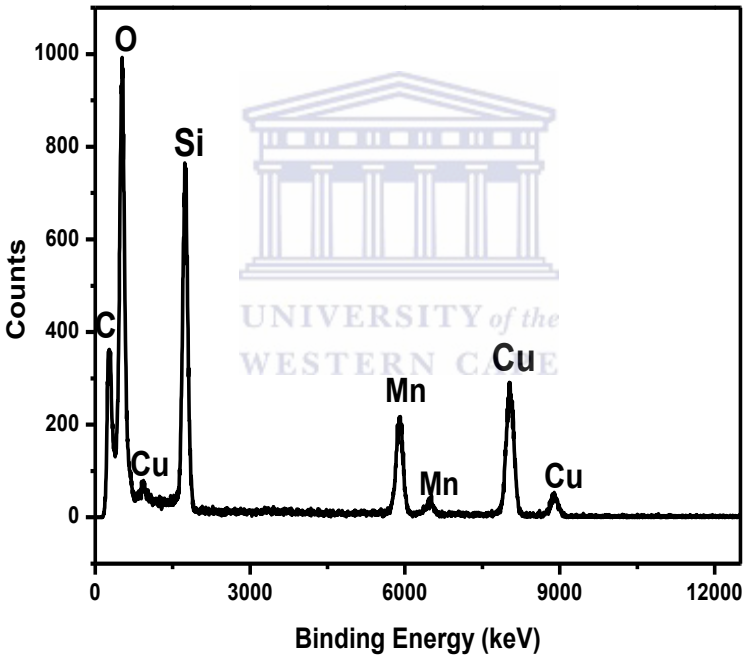

Figure 4.8: EDX spectra of pristine Li_2MnSiO_4 cathode material obtained from HRTEM.

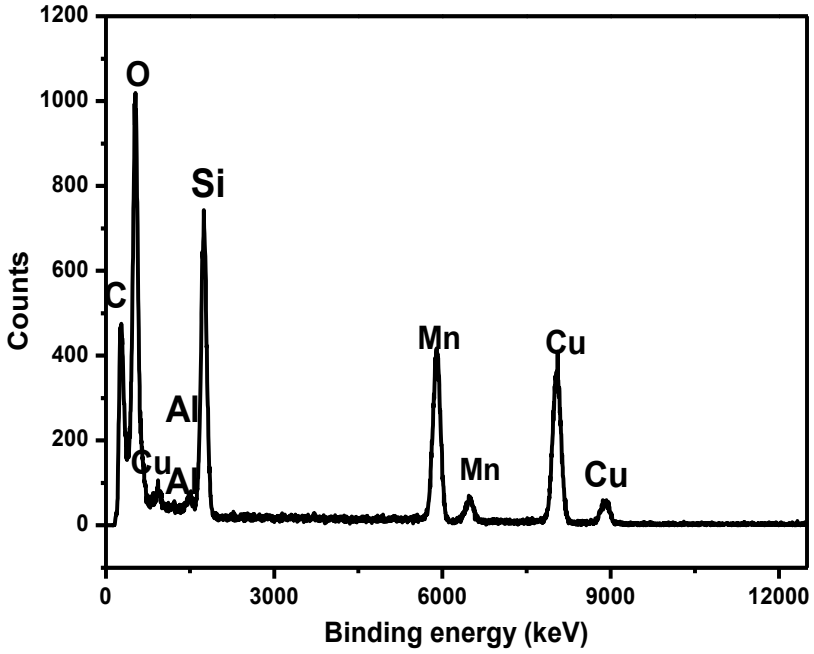

Figure 4.9: EDX Spectra of Novel nanostructured Li_2MnSiO_4/Al_2O_3 obtained from HRTEM.

4.2 Spectroscopic Techniques

4.2.1 Fourier Transform Infra-Red Spectroscopic Studies

FTIR spectroscopy was used to evaluate the functional groups present in the as-prepared pristine and novel cathode materials. The conditions for the FTIR analysis were discussed in section 3.3.1.2.1 above. Figure 4.10 below represents the FTIR spectra of alumina nanoparticles, the pristine and novel cathode materials. Bands corresponding to the internal vibration of the silicate anions according to previous work by Xie *et al.*, resonate in the range of 400-2400 cm^{-1}[92]. Collected spectra are presented in the region 400-2000 cm^{-1} and supplementary evidence for the structures of the synthesized materials is offered by the spectra. The main absorption features at 1006 cm^{-1} and around 489 cm^{-1} can be assigned to the asymmetric and symmetric vibrations of the Si-O-Si bonds in the silicate tetrahedral (SiO_4^{4-}) [93]. The distinct and sharp band at 852 cm^{-1} can be assigned to the vibration of the Si-O-Mn linkage, thus confirming the complete incorporation of Mn ions into the Si-O framework. The bands at 1071 cm^{-1} can be assigned to the vibration of the Al-O-Al bonds in and from Al_2O_3

nanoparticles, and the band at 1654 cm-1 can be perhaps apportioned to the adsorption of water (H-O-H) molecules on the surface of the Al_2O_3 nanoparticles [94].

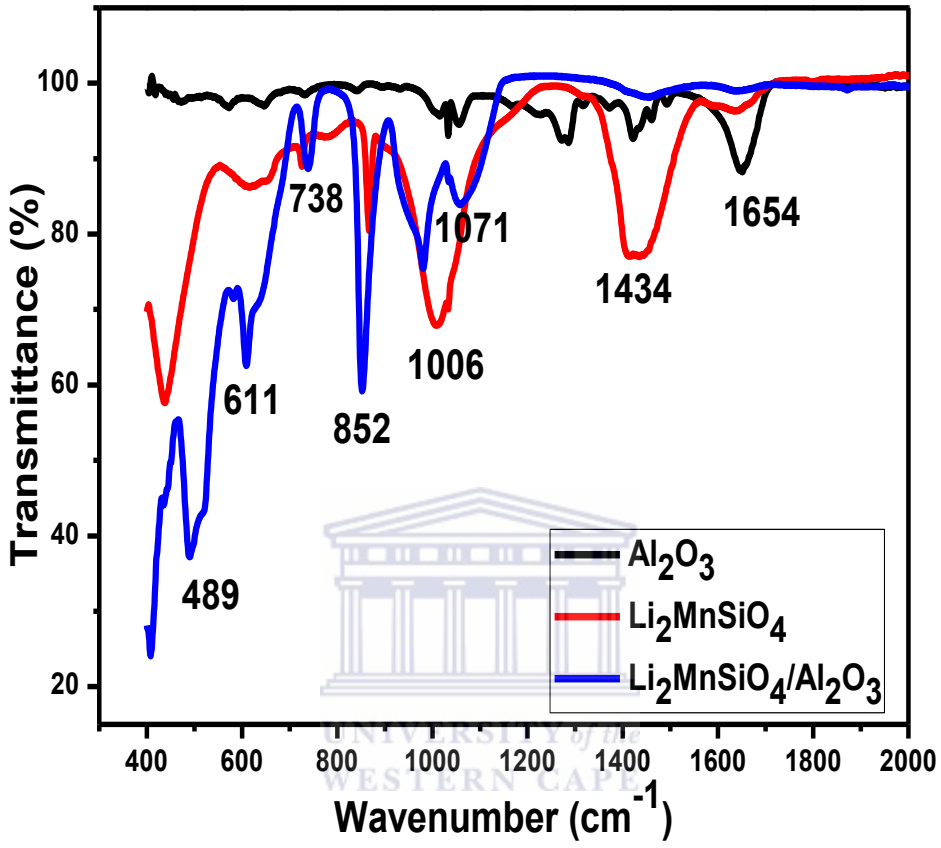

Figure 4.10: FTIR spectra of Al_2O_3 nanoparticles, Pristine (Li_2MnSiO_4) and novel (Li_2MnSiO_4/Al_2O_3) nanostructured cathode materials.

4.2.2 X-ray Diffraction Studies

XRD was used to ascertain the crystal structure, phase purity and the average crystallite size of the synthesized pristine and novel nanostructured Li_2MnSiO_4 cathode materials. Figure 4.11 below shows the XRD pattern of the pristine Li_2MnSiO_4 and the novel Li_2MnSiO_4/Al_2O_3 cathode materials taken at a 2θ range of 10 - 90°. The sharp intense peaks indicate the crystalline nature of the materials. All the samples showed similar main peaks (Bragg positions); 010, 011, 210, 002, 120, 211, 022 and 023 at the 2θ values of 18.77, 26.96, 33.11, 36.29, 38.57, 44.03, 51.76, and 64.23° respectively. Both samples can be indexed on the basis of the orthorhombic Li_2MnSiO_4 phase with the $Pmn2_1$ space group which is predicted to be iso-structural with the

low temperature Li_3PO_4 phase. This phase is analogous to the Li_2FeSiO_4 structure, and consists of a distorted hexagonal pattern of oxygen ions with half of the tetrahedral sites occupied by Li, Mn and Si [15]. The orthorhombic $Pmn2_1$ phase provides the simplest migratory pathway for Li-ions due to the high symmetry and symmetrical equivalence of all its Li sites in the unit cell, thus will lead to high electrochemical reversibility and overall performance [54]. Compared to the XRD pattern of the pristine Li_2MnSiO_4, the XRD pattern of the novel Li_2MnSiO_4/Al_2O_3 cathode material appears to be weaker with minor and overlapping peaks at 39.24 and 51.32° corresponding to the alpha alumina (α-Al_2O_3) nanoparticles phase. This can be indicative of the fact that, the presence of the alumina nanofilm on the surface of the Li_2MnSiO_4 nanoparticles prevented the growth of the pristine nanoparticle grains leading to a decrease in particle size as also observed in morphological studies.

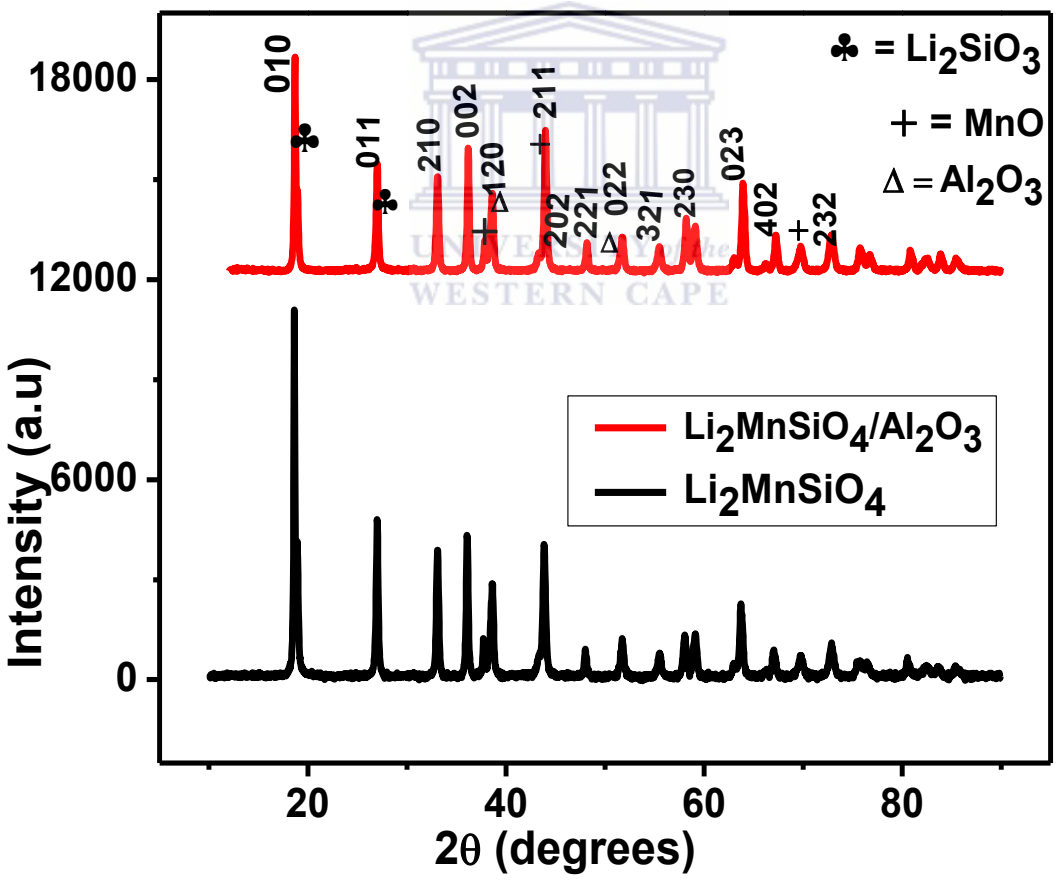

Figure 4.11: XRD patterns of pristine Li_2MnSiO_4 and novel Li_2MnSiO_4/Al_2O_3 cathode materials.

In addition to the main Bragg peaks, five other unremarkable peaks at 19.47, 27.43, 37.88, 44.04, and 69.97° can be identified in the XRD pattern of the pristine and novel cathode

materials, which can be ascribed to the Li_2SiO_3 and MnO impurities. These results are consistent with those obtained from previous reports by Aravindan *et al* and Liu *et al.,* [95-96], and a recent review [15], who reported that the preparation of a 100 % phase pure Li_2MnSiO_4 cathode material is a very complicated one and impurity phases like MnO and Li_2SiO_3 are unavoidable in the orthorhombic $Pmn2_1$ polymorph.

The average crystallite size can be calculated from the (210) Bragg peak, using Scherrer's formula:

$$D = {}^{K\lambda}/_{\beta Cos\theta} \qquad (4.1)$$

Where *D* is the mean crystallite size, *K* is the shape factor constant (0.89), λ is the wavelength of the X-rays, β is the full width at half maximum (FWHM) of the (210) Bragg peak, and θ is the angle of reflection of the (210) peak. The lattice parameters were calculated using the equation:

$$a_0 = d_{hkl}\,(h^2 + k^2 + l^2)^{1/2} \qquad (4.2)$$

Where *h*, *k* and *l* are the miller indices of the crystal plane and *d* is the inter-planar spacing determined using Bragg's equation:

$$d_{hkl} = {}^{\lambda}/_{2Sin\theta} \qquad (4.3)$$

Table 4.3: Crystallographic parameters calculated from the XRD pattern of the pristine and novel cathode materials

Parameter	Pristine Li_2MnSiO_4	Novel Li_2MnSiO_4/Al_2O_3
Average crystallite Size D, (nm)	58.415	51.128
Inter-planar spacing d_{hkl}, (nm)	2.719	2.631
Lattice constant a_0, (nm)	6.079	5.883

Table 4.3 above summarizes the values obtained for the average crystallite size, d-spacing and the lattice parameter (a_0) for the pristine Li_2MnSiO_4 and the novel Li_2MnSiO_4/Al_2O_3 cathode materials. The values for the average crystallite sizes for these materials (58.4 nm for the pristine and 51.1 nm for the novel cathode material) are in the same range with average sizes obtained from microscopic studies (HRSEM and HRTEM). Moreover, the value for the lattice constant a_0 (6.079 nm for the pristine and 5.883 nm for the novel cathode material), is also in agreement with results reported by Liu *et al*., and Arroyo-deDompablo *et al*., [97-98].

4.2.3 Solid-state Nuclear Magnetic Resonance Spectroscopic Studies

SS-NMR was used to study the local environment of lithium nuclei in the synthesized materials and to explore their structural and electronic anisotropies. The conditions for these analyses were explained in sub section 3.3.1.2.3 above. Figure 4.12 below represents the NMR spectra of the pristine and novel nanostructured cathode materials. Both spectra are dominated by the interaction of the lithium nuclei with the paramagnetic centers. That is, interaction of the lithium nuclei with magnetic moments of the unpaired electron spins [99]. The unpaired electrons of the tetrahedrally- coordinated high-spin Mn^{2+} ions in $Li_2Mn^{2+}SiO_4$ with a d^5 electronic configuration, are present in the $eg^2t_2g^3$ configuration, giving rise to an isotropic contribution known as the Fermi-contact shift which results in the isotropic peaks [100]. In addition, the spin-dipolar interaction between the lithium nuclei and the unpaired electrons of the transition metal ions generate a strong dipolar coupling which leads to the broad spinning sidebands. The isotropic peaks were identified by varying the MAS spinning speed rate. The ^{7}Li-NMR spectrum of the pristine cathode material is characterized by three isotropic peaks at ~310.7, 0.8 and – 306.2 ppm. The isotropic peak at ~310.67 and -306.21 ppm arises from the majority $Pmn2_1$ polymorph, based on literature assignments. Two chemical bonds are present

between the paramagnetic center and the lithium nuclei; the Li-O-Mn, considered predominantly ionic and the Si-O-Mn, regarded as predominantly covalent. The peak at ~0.8 ppm ascends from the ionic character of the lithium nuclei and a contribution from the diamagnetic Li_2SiO_3 impurity observed in XRD studies. These values are slightly shifted in the spectrum of the novel cathode material (~310. 7 and -307.5 ppm, ~0.0 ppm) due to the presence of the alumina thin film which considerably alters its chemical environment. This is due to the fact that, addition of the Al_2O_3 thin film likely induces covalently bonded Al-O-Si species which will enhance both local-order and long-order fluctuations leading to slight deshielding around the lithium nuclei and a shift to higher frequencies.

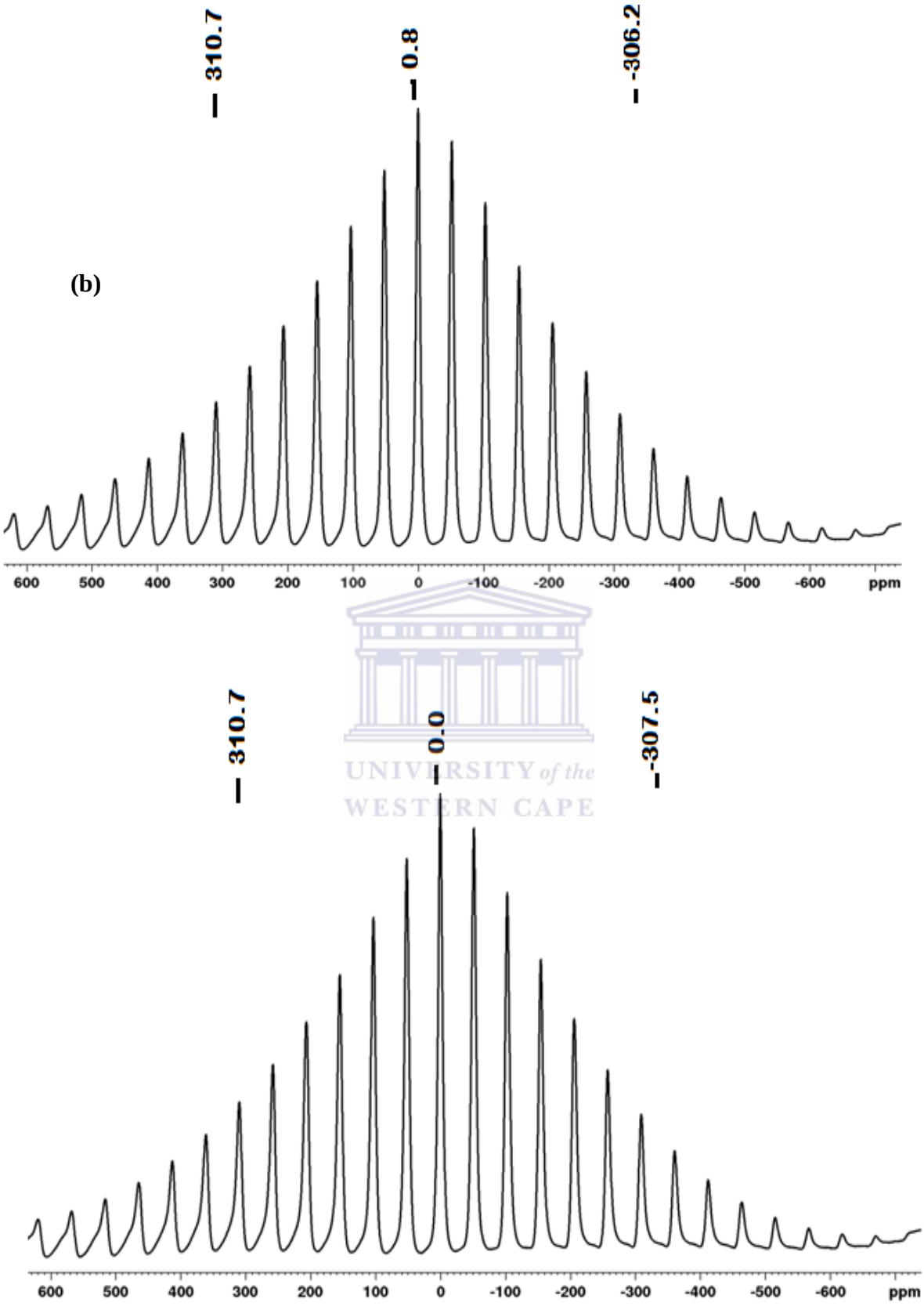

Figure 4.12: ^{7}Li MAS NMR spectra of pristine Li_2MnSiO_4 (a) and the novel Li_2MnSiO_4/Al_2O_3 (b) cathode materials at a MAS spinning speed of 10 kHz.

4.2.4 X-ray Photoelectron Spectroscopic Studies

XPS was used to carefully investigate the composition, purity and surface electronic states of the synthesized materials. The conditions for these analyses were explained in sub section 3.3.3.2.4 above. Figure 4.13 and 4. 14 below display the XPS full spectra of the pristine Li_2MnSiO_4 and the novel Li_2MnSiO_4/Al_2O_3 cathode materials respectively. All expected elements were observed especially lithium which cannot be detected by any other characterization technique due to the low binding energy of its electrons. No other impurity peaks were observed, thus indicating the high purity of the samples.

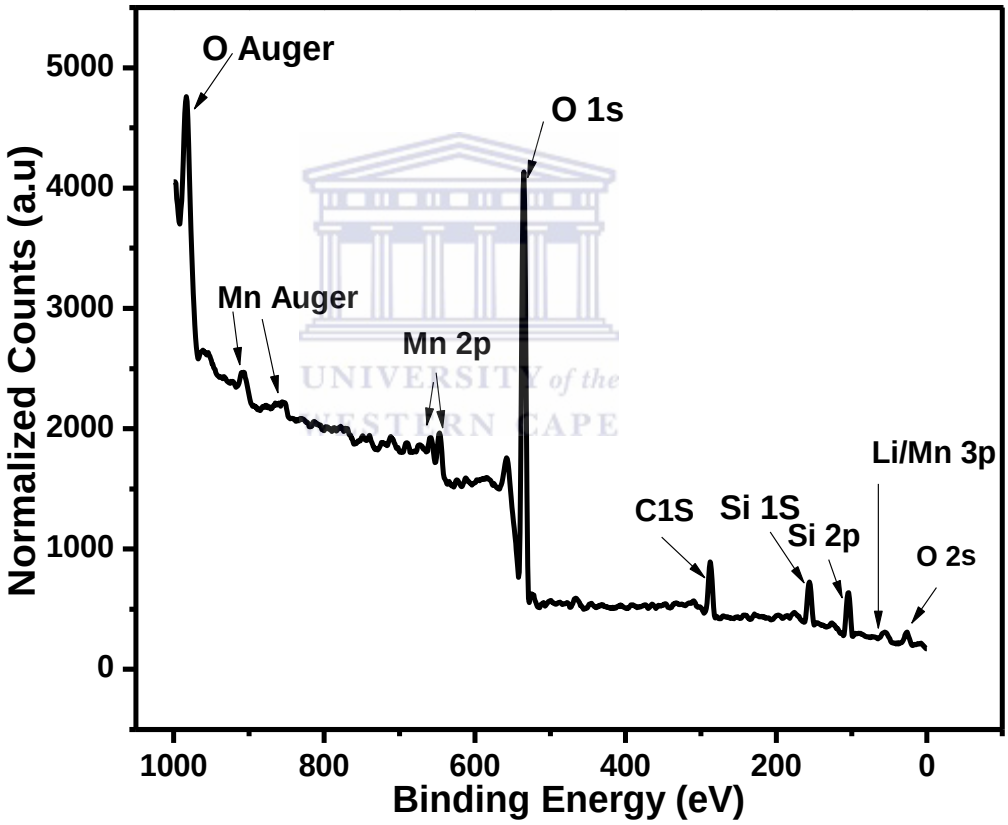

Figure 4.13: XPS full spectrum of the pristine Li_2MnSiO_4 cathode material showing all elements present in the sample.

The carbon (C1S) peak observed in the spectrum above comes from the carbon energy source used to mount the samples during analysis.

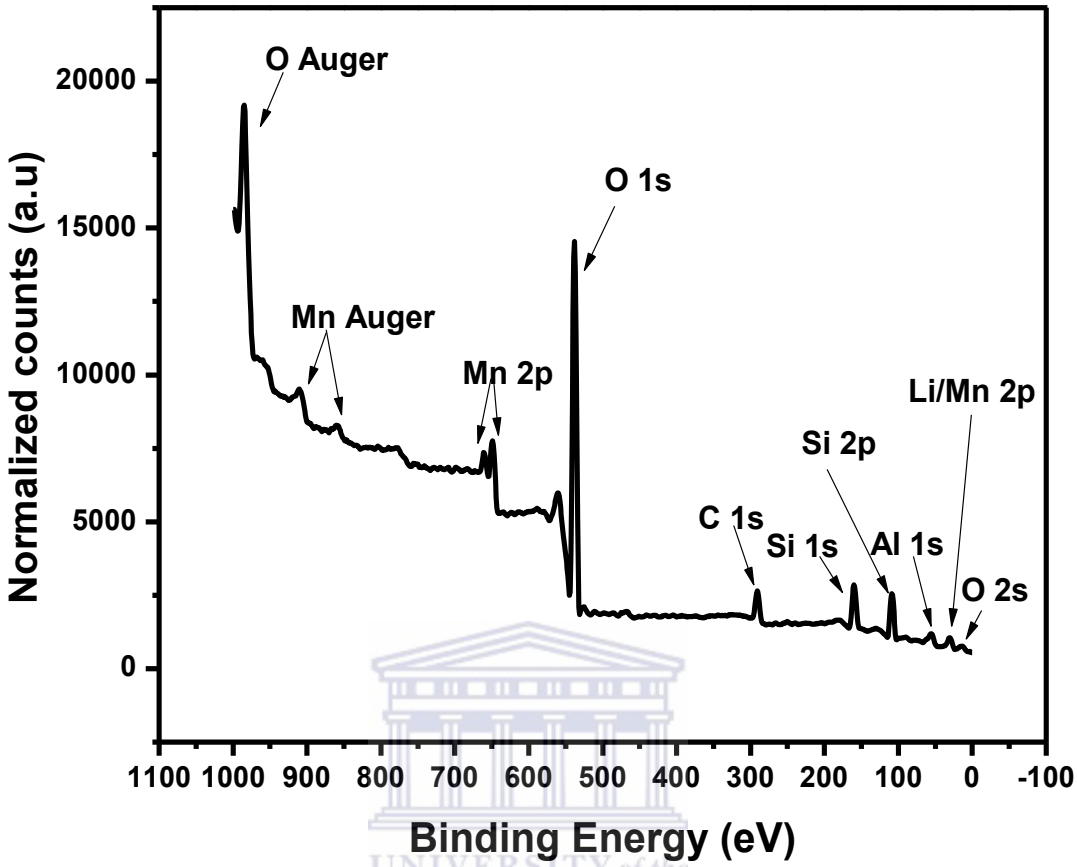

Figure 4.14: XPS full spectrum of the novel Li_2MnSiO_4/Al_2O_3 cathode material showing the composition of the sample.

(a)

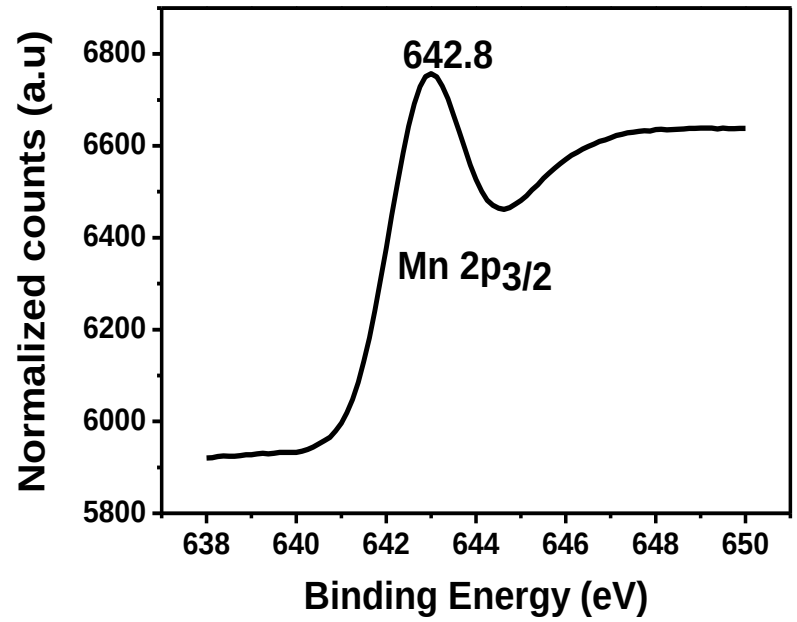

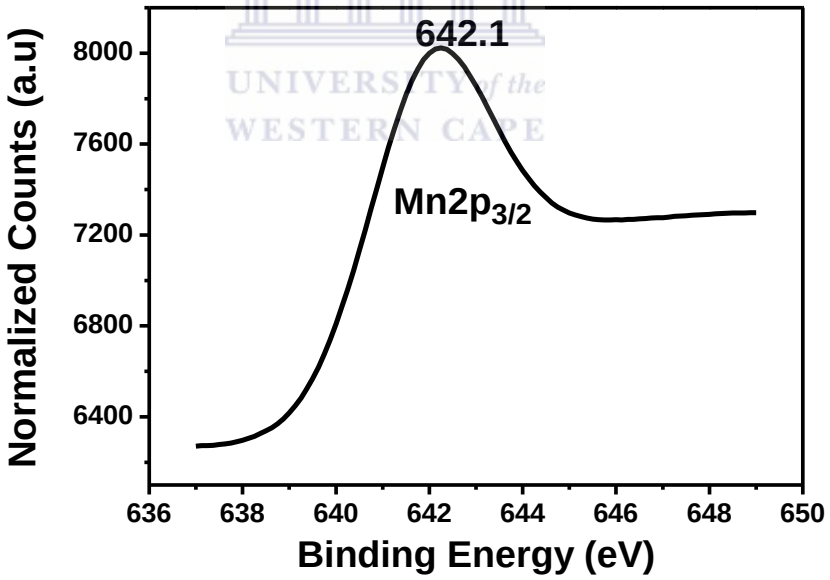

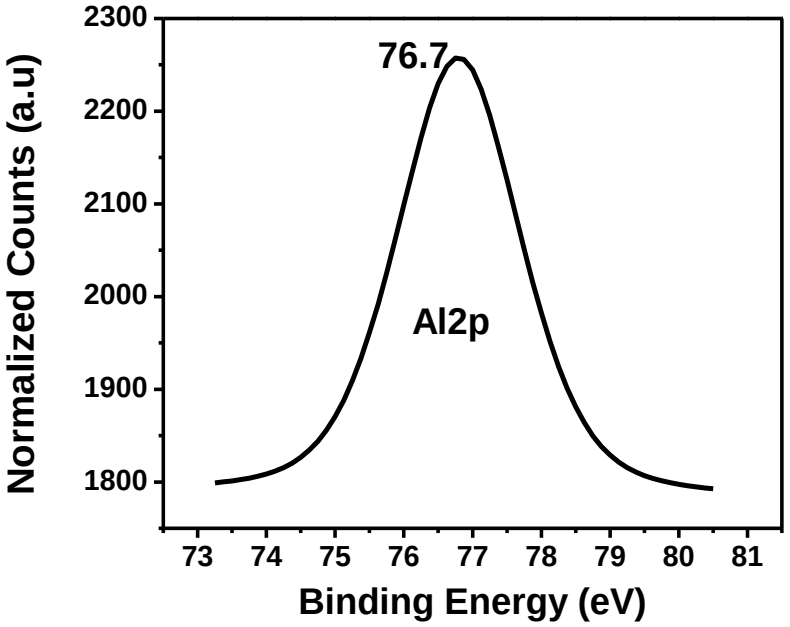

Figure 4.15: Fitted XPS spectra of Mn2p **(a)** Pristine $Li_2MnSiO4$, **(b)** Novel Li_2MnSiO_4/Al_2O_3 and Al2p spectrum **(c)** in the novel Li_2MnSiO_4/Al_2O_3 cathode material.

From the binding energy and intensity of the photoelectron peak, the elemental identity, chemical state and the quantity of detected element can be determined. The Mn2p spectrum in the pristine and the novel cathode material show binding energies of 642.8 and 642.1 eV ($Mn2p_{3/2}$), which are consistent with that of Mn^{2+}, confirming that the divalent state of manganese is present in our synthesized materials [101-102].The binding energy (76.7 eV) of the Al2p XPS spectrum in the novel cathode material is also in line with that of Al^{3+} in Al_2O_3, indicating that an alumina thin film was successfully coated on the surface of the pristine Li_2MnSiO_4 nanoparticles [103-104].

4.3 Electrochemical Techniques

4.3.1 Cyclic Voltammetric Studies

CV studies were conducted on the synthesized materials to determine the electron transfer processes, redox behavior of the electro-active species and their kinetic and thermodynamic

facets. Figure 4.16 below shows a comparative cyclic voltammetric plot of the bare glassy carbon electrode (GCE) and the pristine Li_2MnSiO_4 cathode material on the surface of the GCE in 1 M $LiNO_3$ electrolyte, at a potential window of -800 mV to 800 mV.

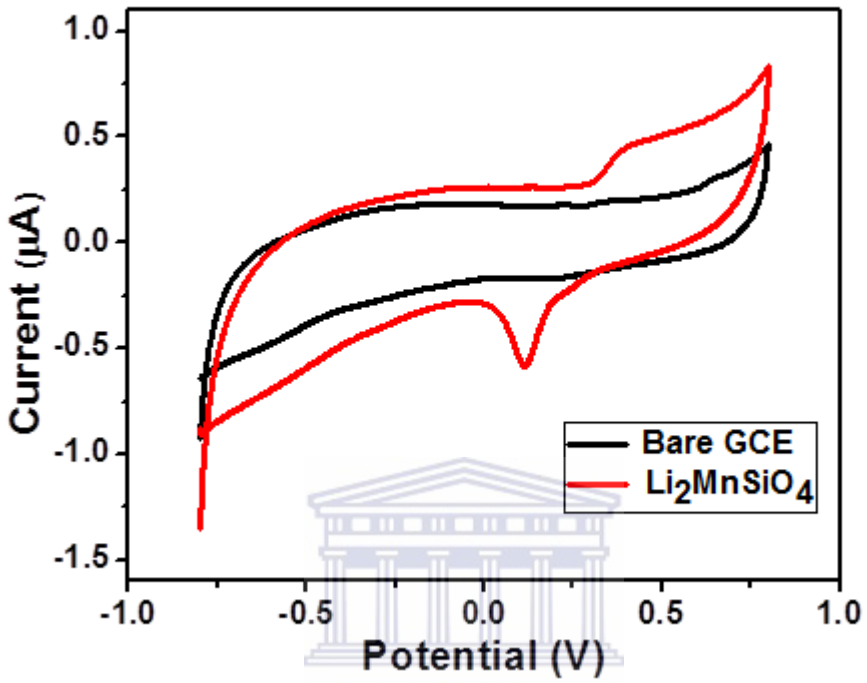

Fig 4.16: Cyclic voltammograms of the bare GCE and Li_2MnSiO_4/GCE in 1 M $LiNO_3$ at a scan rate of 10 mV/s.

From figure 4.16 above, it can be observed that the bare GCE shows no electro-activity in 1 M $LiNO_3$ whereas Li_2MnSiO_4 cathode material shows a prominent redox couple (Mn^{2+}/Mn^{3+}) with the anodic peak potential (E_{pa}) at 427 mV and the cathodic peak potential (E_{pc}) at 116 mV.

Figure 4.17 below shows the comparative cyclic voltammograms of the pristine Li_2MnSiO_4 and novel Li_2MnSiO_4/Al_2O_3 cathode materials swept at a potential window of -800 mV to 800 mV in 1M $LiNO_3$ at a scan rate of 10 mV/s.

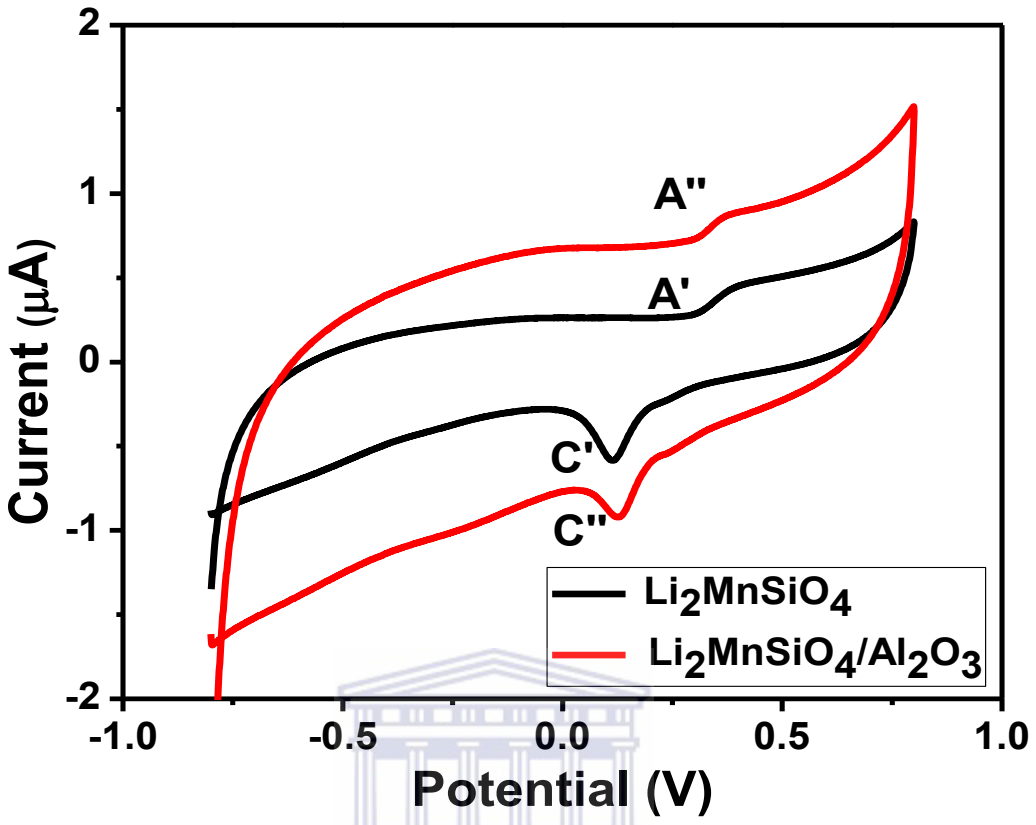

Figure 4.17: Cyclic voltammograms of the pristine Li_2MnSiO_4/GCE and Novel Li_2MnSiO_4/Al_2O_3/GCE cathode materials in 1 M $LiNO_3$ at a scan rate of 10 mV/s.

The CV profiles of the pristine Li_2MnSiO_4 and the novel Li_2MnSiO_4/Al_2O_3 cathode materials consist of a pair of well-defined redox peaks (*A*', *A*'' and *C*', *C*''), which correspond to the removal of Li^+ ions from the orthosilicate sub-lattice and subsequent oxidation of Mn^{2+} to Mn^{3+} (*A*' and *A*'') and the insertion of Li^+ ions into the $LiMnSiO_4$ framework with the associated reduction of Mn^{3+} to Mn^{2+} ions (*C*' and *C*''). The redox processes are represented by Equations 4.4 and 4.5 below.

From table 4.2 below, the observed increase in the peak current values (I_{pa} and I_{pc}) and the decrease in the peak-to-peak separation (ΔE_p) for the novel cathode material compared to the pristine material depicts a better electrochemical cyclic performance of the novel cathode material. This can be explained by the fact that, addition of the alumina nanofilm reduced the

diffusion pathway of electrons and stabilized the structural instability of the pristine cathode material by improving the packing density of the particles which lead to a faster and better electrochemical reversibility of the novel cathode material [95].

$$Anodic\ half\ reaction\ (A):\ Li_2Mn^{2+}SiO_4 \rightarrow LiMn^{3+}SiO_4 + Li^+ + e^- \quad (4.4)$$

$$Cathodic\ half\ reaction\ (B):\ LiMn^{3+}SiO_4 + Li^+ + e^- \rightarrow Li_2Mn^{2+}SiO_4 \quad (4.5)$$

Table 4.4: Redox parameters obtained from the cyclic voltammograms of the pristine and novel cathode materials

Electrode material	E_{pa} (mV)	E_{pc} (mV)	I_{pa} (µA)	I_{pc} (µA)	ΔE_p (mV)	E^o (mV)
Pristine $Li_2MnSiO4$	427	116	0.489	-0.588	311	271.5
Novel Li_2MnSiO_4/Al_2O_3	402	129	0.931	-0.912	273	265.5

The specific charge and discharge capacities of the pristine and novel cathode materials were calculated using the cyclic voltammograms of these electrode materials at a much lower scan rate (1 mVs^{-1}) due to the redox behavior of the materials. The following approach was adopted for these calculations.

$$\text{Specific Capacity (mAh/g)} = {}^{\text{Charge (Q)}}/_{\text{Active mass of the electrode material}}\, X\ 1000 \quad (4.4)$$

Where;

$$Q\ (Ah) = \frac{\text{Area (AV)}}{\text{Scan rate } (Vs^{-1})}\ \text{x}\ \frac{1\ \text{h}}{3600\ \text{s}} \quad (4.5)$$

The area (AV) is obtained by integrating the oxidative current-potential curve/peak when calculating the charge capacity and the reductive current-potential curve/peak in the case of the discharge capacity for both materials. The active mass used for the electrodes was 7.5 x 10^{-5} g. Therefore, the charge capacity for the novel cathode material was calculated as follows:

$$\mathrm{Q_{charge}} = \frac{5.638\times10^{-5}\mathrm{AV}}{0.001\mathrm{Vs^{-1}}} \times \frac{1\ \mathrm{h}}{3600\ \mathrm{s}} \tag{4.6}$$

$$Q_{charge} = 1.566 \times 10^{-5} Ah$$

$$Specific\ capacity_{charge} = \frac{1.566\times10^{-5}\ Ah}{7.5\times10^{-5}\ g} \times 1000 \tag{4.7}$$

$$Specific\ capacity_{charge} = 208.8\ mAh/g$$

Table 4.5 below shows the specific charge and discharge capacities for the pristine and novel cathode materials calculated according to the procedure illustrated above, with their Coulombic efficiencies and capacity loss. Compared to the pristine material, the novel cathode material exhibits a much higher charge and discharge capacity of ~209 mAh/g and 159 mAh/g respectively. These capacity values show that about 1.2 mol of lithium is being extracted from the Li_2MnSiO_4 crystalline structure in the novel cathode upon the oxidation of Mn^{2+} to Mn^{3+} and almost 0.96 mol of lithium is inserted back into the structure as Mn^{3+} ions are being reduced to the divalent state Mn^{2+}, giving rise to a relatively good efficiency and capacity retention, hence confirming the improved electrochemical performance of the novel cathode material over the pristine material. These capacity values are consistent with those obtained by Zhu and Zhang *et al*., [63, 105].

Table 4.5: Charge and discharge capacity values for the pristine and novel cathode materials with their percentage capacity loss and Coulombic efficiencies

Cathode material	Charge capacity (mAh/g)	Discharge capacity (mAh/g)	Coulombic Efficiency (%)	Capacity loss (%)
Pristine Li_2MnSiO_4	107	68	64	36
Novel Li_2MnSiO_4/Al_2O_3	209	159	76	24

The Coulombic efficiency (%) values were calculated using the following formula:

$$\frac{\text{Discharge capacity}}{\text{Charge Capacity}} \times 100\ \%$$

Figure 4.18 below presents the effect of scan rate on the electrochemical reversibility of the novel Li_2MnSiO_4/Al_2O_3 cathode material. It can be observed that the electrochemical process demonstrated by the novel cathode is quasi-reversible, since at lower scan rates, the electrode behaves as a reversible system while at higher scan rates; it behaves as an irreversible system. That is, at lower scan rates, the peak potentials do not depend on the scan rates, whereas at higher scan rates, the peak potentials shift with an increase in the scan rate.

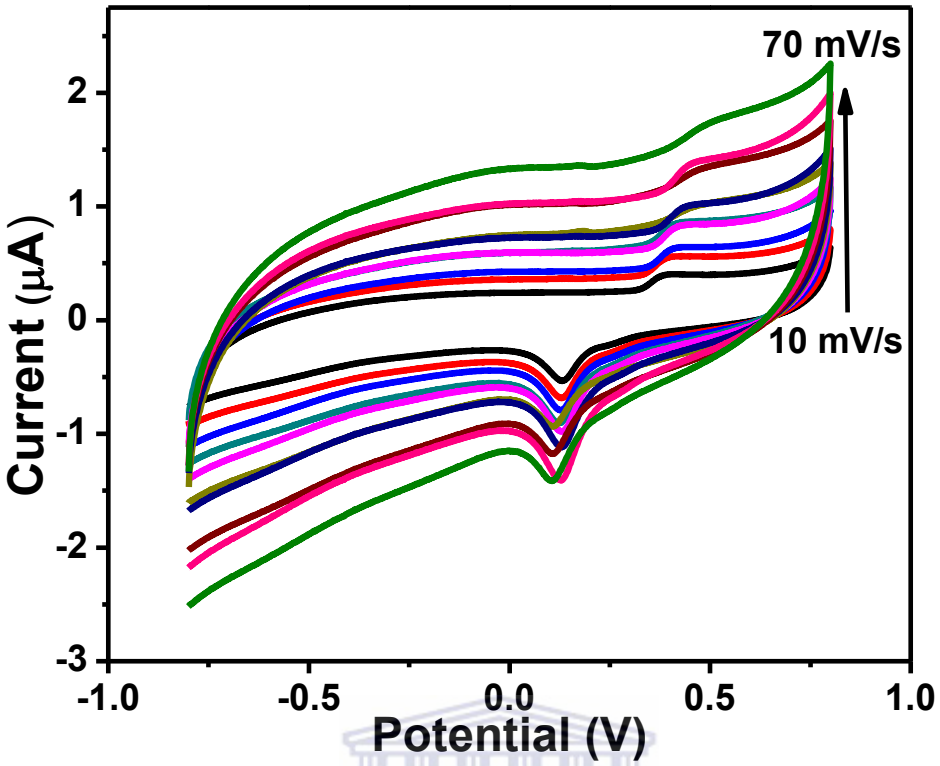

Figure 4.18: Effect of scan rate on the electrochemical cycling behavior of the novel Li_2MnSiO_4/Al_2O_3 cathode material.

The relationship between the peak current and the scan rate was further investigated for the pristine Li_2MnSiO_4 and novel Li_2MnSiO_4/Al_2O_3 cathode materials and are represented by Figures 4.19 and 4.20 below. It was discovered that the peak current displayed a linear relationship with the square root of the scan rate, and this further confirms the fact that the peak current is directly proportional to the concentration of the ions in the bulk of the material as presented by the Randles-Sevcik equation (Equation 3.3 under sub-section 3.3.2.1 above). This implies that the electrochemical process occurring at the surface of these electrodes is diffusion controlled. The diffusion coefficient of Li^+ ions calculated using the Randles Sevcik equation for the pristine Li_2MnSiO_4 and novel Li_2MnSiO_4/Al_2O_3 electrode materials were 6.79 x 10^{-7} cm^2s^{-1} and 3.06 x 10^{-6} cm^2s^{-1} respectively. The diffusion coefficient for the novel cathode material is one order of magnitude higher than that of the pristine material and fairly higher than some values reported in literature (~10^{-16}) [65, 95]. This improvement in the diffusion coefficient is mainly due to the shorter diffusion path in the novel Li_2MnSiO_4/Al_2O_3 nanoparticles which is very beneficial in enhancing the diffusion rate of lithium ions through

the bulk of the electrode material and improving the overall electrochemical performance of the cathode material even at high rate [63].

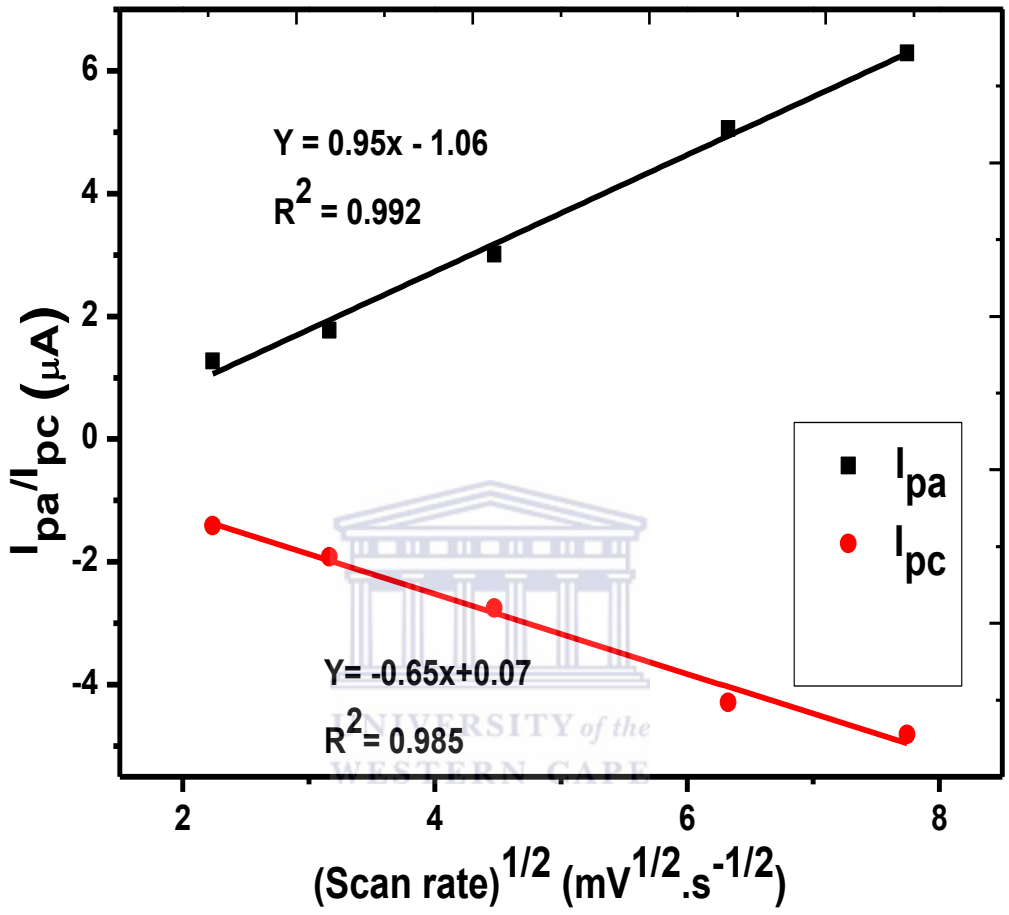

Figure 4.19: Linear relationship between the peak current (I_{pa} and I_{pc}) versus the square root of the potential scan rate of the novel Li_2MnSiO_4 cathode material.

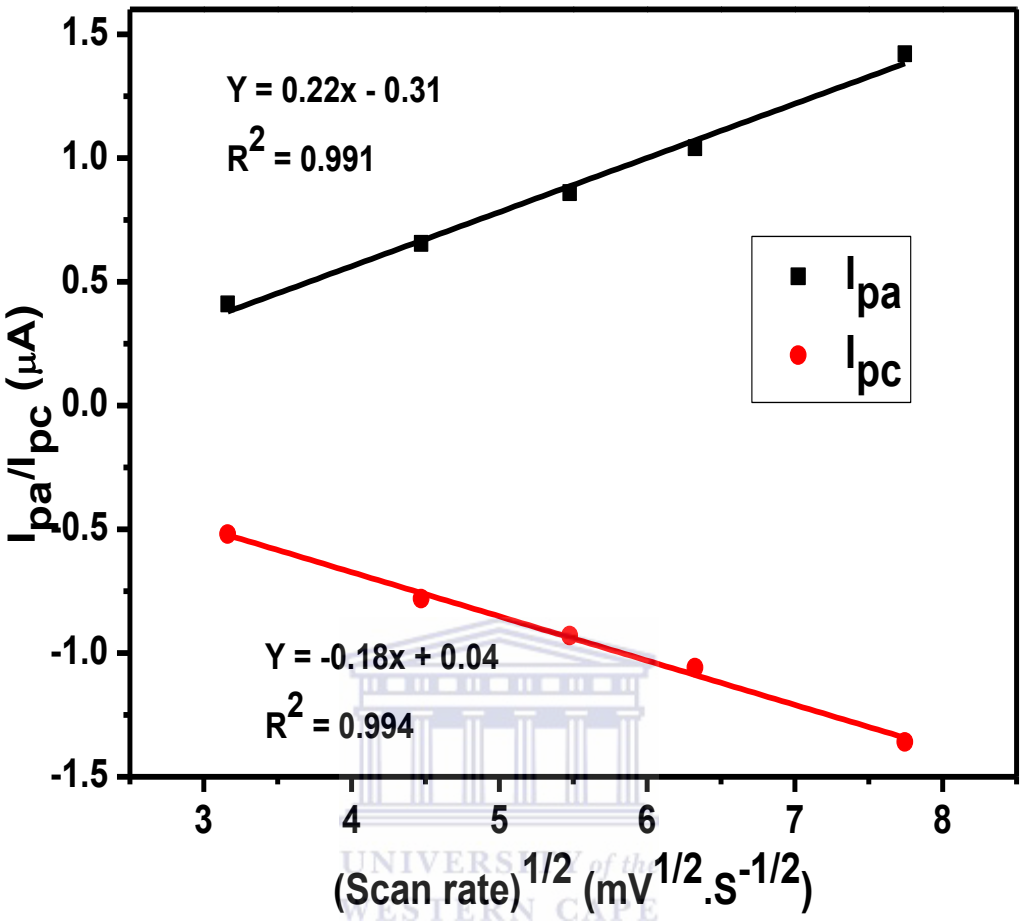

Figure 4.20: Linear relationship between the peak current (I_{pa} and I_{pc}) versus the square root of the potential scan rate of the novel Li_2MnSiO_4/Al_2O_3 cathode material.

2.1.1 Square wave Voltammetric investigation

SWV was used to confirm the pair of redox peaks obtained from cyclic voltammetry. Figures 4.21 and 4.22 below represent the oxidative and reductive SWV profiles of the novel cathode material swept at a potential window of -800 mV to 800 mV at a scan rate of 24 mV/s. Due to the high sensitivity and lower detection limit of SWV, the redox peaks appear with much higher intensities as compared to CV, with the anodic peak (forward scan) occuring at ~402 mV and the cathodic peak (reverse scan) occuring at ~143 mV.

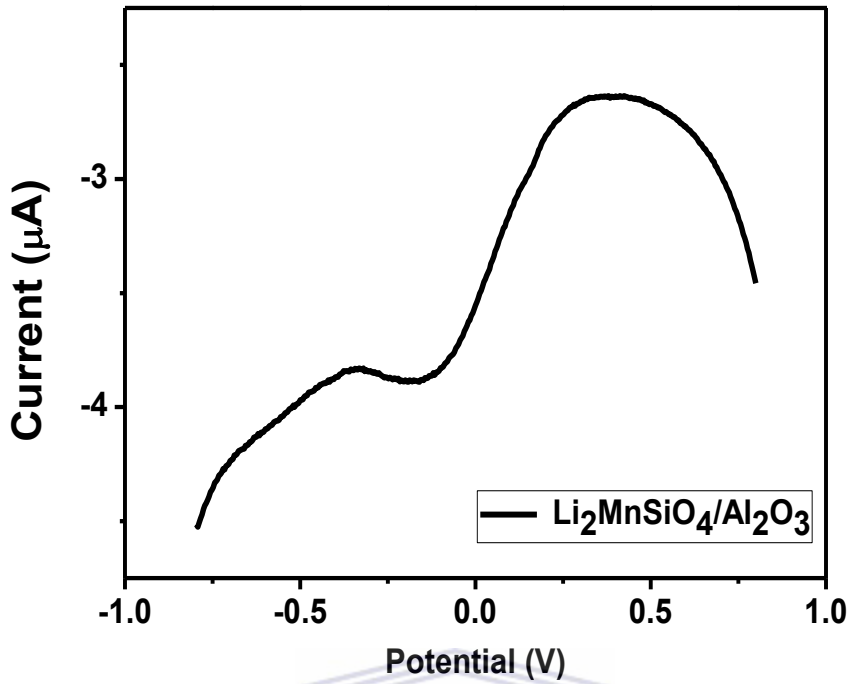

Figure 4.21: Anodic Square wave voltammogram (forward scan) of the novel Li_2MnSiO_4/Al_2O_3 in 1 M $LiNO_3$ at a scan rate of 24 mVs^{-1}.

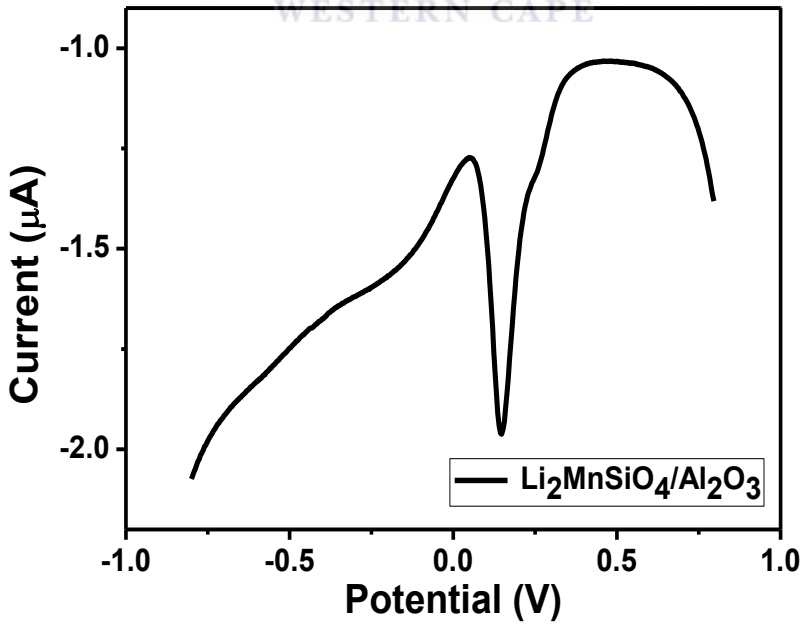

Figure 4.22: Cathodic Square wave voltammogram (reverse scan) of the novel Li_2MnSiO_4/Al_2O_3 in 1 M $LiNO_3$ at a scan rate of 24 mVs^{-1}.

2.1.2 Electrochemical Impedance Spectroscopic Studies

EIS was used to investigate the electrical resistance and diffusion processes occurring at the electrochemical interfaces of the pristine Li_2MnSiO_4 and novel Li_2MnSiO_4/Al_2O_3 electrodes. Figure 4.23 below present the Nyquist plot, while Figures 4.24 and 4.25 show the Bode plots for the bare GCE, the pristine Li_2MnSiO_4 and the novel Li_2MnSiO_4/Al_2O_3 materials. The Nyquist plots consist of a small semicircle which describes the electron transfer limiting process and a linear part which provides information about the diffusion controlled processes. The Bode plots give information on the conductivity and reactivity of the Li_2MnSiO_4 cathode materials from the value of the log of the total impedance and the log frequency maxima of the phase angle plot respectively. The Randles circuit (Figure 4.26) which is a commonly used equivalent circuit for EIS data fitting was used to fit the data obtained for the above materials.

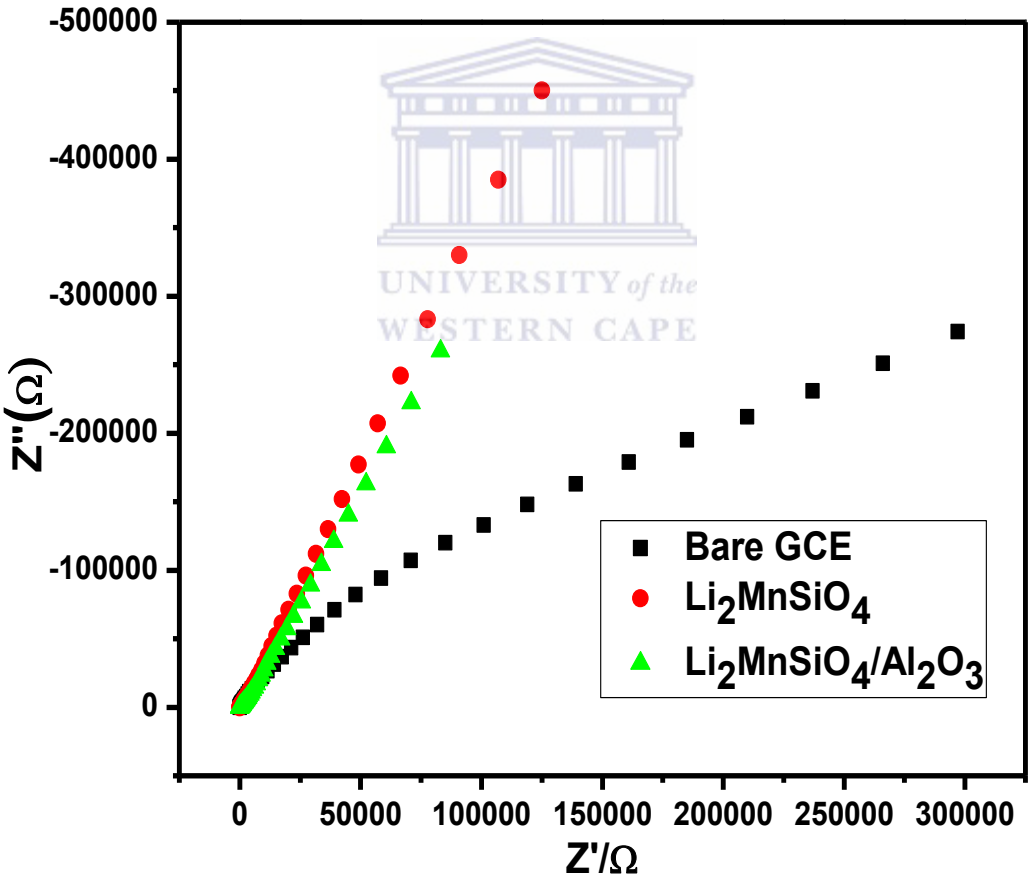

Figure 4.23: Nyquist plots for the bare GCE, the pristine Li_2MnSiO_4 and the novel Li_2MnSiO_4/Al_2O_3 cathode materials obtained at a frequency range of 0.1 Hz – 100 kHz in 1M $LiNO_3$.

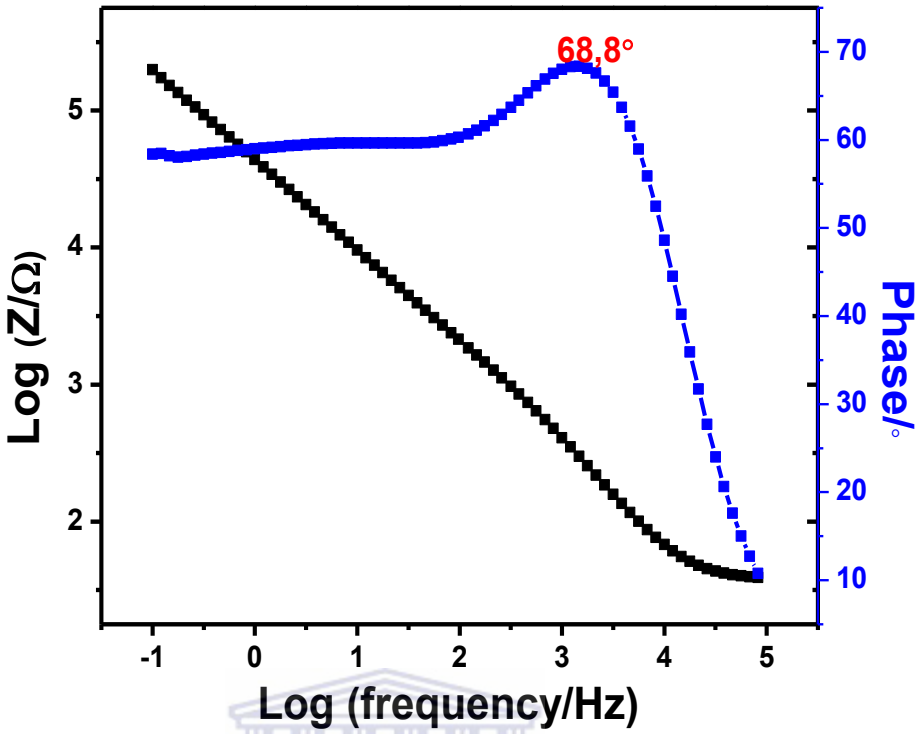

Figure 4.24: Bode plot for the pristine Li_2MnSiO_4 cathode material obtained at a formal potential of 272 mV in 1M $LiNO_3$.

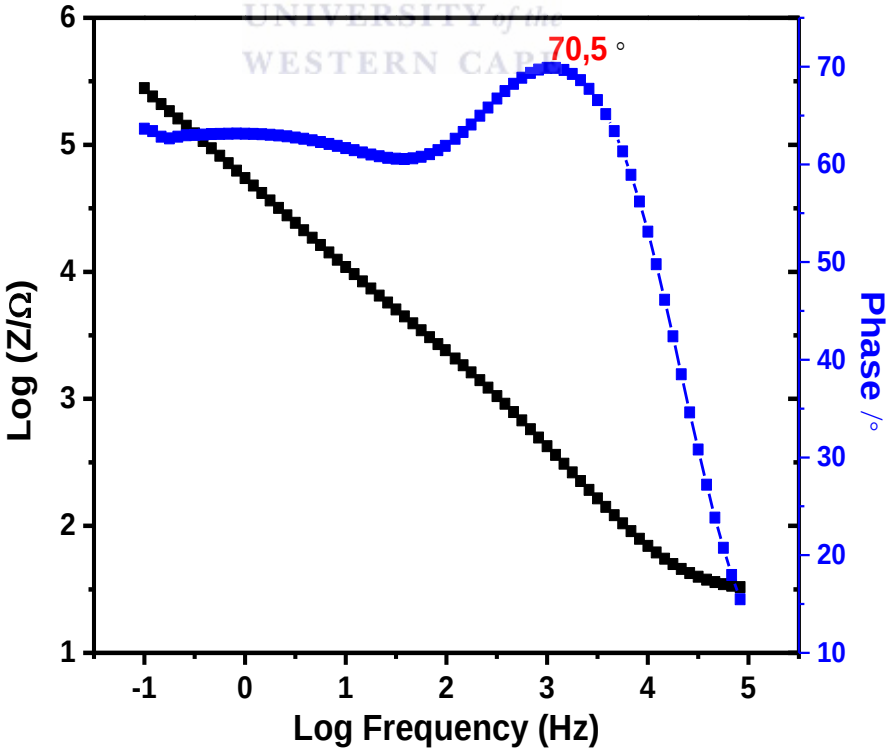

Figure 4.25: Bode Plot for the novel Li_2MnSiO_4/Al_2O_3 cathode material obtained at a formal potential of 266 mV in 1 M $LiNO_3$.

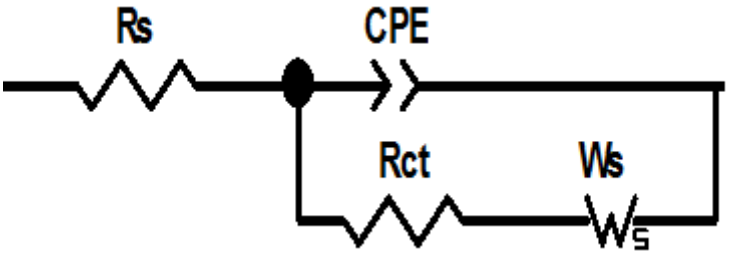

Figure 4.26: The Randles equivalent circuit model.

From Figure 4.26 above, R_s represents the solution resistance to the flow of electrons, R_{ct}, the charge transfer resistance formed by the kinetically-controlled electrochemical reaction occurring at the surface of the Li_2MnSiO_4 electrodes when in contact with the electrolyte. *CPE* is the constant phase element (double layer capacitance) generated by non-uniform current distributions when ions from the electrolyte solution adsorb onto the electrode surface and W_s is the Warburg impedance component arising from ion diffusion quotients.

The following kinetic parameters (Table 4.6 below) were obtained from fitting the EIS plots of the bare GCE, the pristine Li_2MnSiO_4 and the novel Li_2MnSiO_4/Al_2O_3 electrodes.

Table 4.6: Kinetic parameters obtained from the EIS Plots of the different electrodes used

Electrode	***Rs*** **(Ω)**	***CPE*** **(μ F)**	***Rct*** **(Ω)**	***Ws*** **($Ω/s^{-1/2}$)**
Bare GCE	23,30	0,904	1752	0,410
Pristine Li_2MnSiO_4	35,66	0,926	1549	0,620
Novel Li_2MnSiO_4/Al_2O_3	25,79	0,935	1389	0,639

From the frequency at the maximum imaginary impedance of the semi-circle ω_{max}, important kinetic parameters of the electron transfer process such as time constant (τ); the exchange current I_0, which is a measure of the rate of charge exchange between the oxidized and reduced

species at equilibrium potential with no net overall change; the heterogeneous rate constant of electron transfer (K_{et}); the apparent or approximate diffusion coefficient of lithium ions (D_{app}) and the Nernst diffusion layer thickness (X_D) can be calculated according to the following equations [38].

$$\omega_{max} = \frac{1}{R_{ct}C_{dl}} \quad (4.8)$$

$$\tau = \frac{1}{\omega_{max}} \quad (4.9)$$

$$I_0 = \frac{RT}{nFR_{ct}} \quad (4.10)$$

$$K_{et} = \frac{I_0}{nFAC_0} \quad (4.11)$$

$$\sigma = (R_s + R_{ct})\omega^{1/2} \quad (4.12)$$

$$D_{app} = \frac{2(RT)^2}{(\sigma n^2 F^2 AC_0)^2} \quad (4.13)$$

$$X_D = \frac{K_{et}}{D_{app}} \quad (4.14)$$

Where: C_{dl} is the double layer capacitance (*CPE*); R is the molar gas constant = 8.314 J mol^{-1}k^{-1}; T is the room temperature = 293 K; n is the number of electrons exchanged; F is the Faraday's constant = 96486 c mol^{-1}; A is the area of the GCE = 0.071 cm^2 and C_0 is the concentration of lithium ions in Li_2MnSiO_4 (mol cm^{-3}). The values obtained are presented in Table 4.7 below.

Table 4.7: Kinetic parameters of the pristine Li_2MnSiO_4 and novel Li_2MnSiO_4/Al_2O_3 calculated from EIS data obtained at 298 K

Cathode material	τ (s rad^{-1})	I_0 (A)	σ (Ω s$^{-1/2}$)	K_{et} (cm s^{-1})	D_{app} (cm^{2}s^{-1})	X_D (cm)
Pristine Li_2MnSiO_4	1584.5	1.63 x 10^{-5}	39.8	1.0 x 10^{-9}	6.69 x 10^{-15}	6.69 x 10^{-6}
Novel Li_2MnSiO_4/Al_2O_3	1414.4	1.82 x 10^{-5}	37.6	1.0 x 10^{-8}	6.01 x 10^{-12}	6.01 x 10^{-4}

It is evident from the values of these kinetic parameters that a faster electrochemical process occurs in the novel cathode material when compared to the pristine material. That is; the apparent diffusion coefficient of the novel cathode material (6.01 x 10^{-12} cm^2 s^{-1}) is of three orders of magnitude higher than that of the pristine material (6.69 x 10^{-15}cm^{2}s^{-1}). These values follow the same trend as the diffusion coefficient values calculated from CV plots, but their values are fairly different from the results obtained from CV studies because it is an approximate/ apparent value. The reduced value of the charge transfer resistance of the novel Li_2MnSiO_4/Al_2O_3 cathode material (1389 Ω) compared to that of the pristine material (1549 Ω) coupled with the enhancement of the conductivity of the novel cathode material revealed by the Bode plot further confirms it improved electrochemical performance. This improved performance can be attributed to the alumina surface coating which stabilized the interface between the electrode and electrolyte and possibly decreased the surface compliance towards undesired electrode-electrolyte or side reactions [106].

CHAPTER 5

3.0 Conclusion and recommendations

3.1 Conclusion

Lithium transition metal orthosilicates have recently attracted great attention as one of the most promising candidates for next generation cathode materials for lithium-ion batteries due to their numerous appealing properties. In this study, pristine Li_2MnSiO_4 cathode material and a novel high energy density nanostructured Li_2MnSiO_4 based cathode material has been designed through a versatile hydrothermal pathway with subsequent calcinations steps, coupled with investigating the usefulness of alumina nanoparticles as a surface coating. To the best of our knowledge, no such extensive studies have been devoted to the surface modification of Li_2MnSiO_4 cathode material. The synthesized materials were characterized microscopically using HRSEM and HRTEM. These investigations revealed roughly uniform aggregated spherical nanoparticles with particle sizes in the range of 21-90 nm with average diameters of 53 nm for the pristine Li_2MnSiO_4 cathode material. The novel Li_2MnSiO_4/Al_2O_3 cathode material showed a decrease in particle size due to the alumina surface coating which prevented particle growth during the calcination step. This particle size range is of great importance for electrode materials in lithium-ion battery technology due their large surface areas which offer enhanced surface contact between the electrode and electrolyte and reduced diffusion length of lithium ions due to their nanodimensions, and thus will offer better electrochemical performance. X-ray maps obtained from HRSEM for elemental composition and distribution showed an even distribution of the constituent elements which will facilitate the removal and insertion of Li^+ ions from and into the orthosilicate cathode materials. FTIR studies conducted on the pristine Li_2MnSiO_4 and novel Li_2MnSiO_4/Al_2O_3 showed the vibration of the Si-O-Mn linkage, hence confirming the complete incorporation of Mn ions into the Si-O framework. XRD studies conducted on these materials showed crystalline patterns with minor phases of Al_2O_3 for the novel cathode. These crystalline patterns could be indexed to the orthorhombic $Pmn2_1$ space group which was further confirmed by the use of ^7Li Magic Angle Spinning NMR. The orthorhombic $Pmn2_1$ phase provides the simplest migratory pathway for Li-ions due to the high symmetrical equivalence of all Li sites in the unit cell, thus leading to high electrochemical reversibility and an enhancement in the overall performance of the cathode materials. The surface chemistry of the pristine and novel cathode materials probed by XPS

revealed all elements present especially lithium which could not be detected by EDX in HRSEM and HRTEM. The novel Li_2MnSiO_4/Al_2O_3 cathode material demonstrated superior electrochemical performance over the pristine Li_2MnSiO_4 material as evidenced by CV and EIS studies. The diffusion coefficient of the novel Li_2MnSiO_4/Al_2O_3 cathode material calculated from CV and EIS studies was one to three orders of magnitude higher than that of the pristine material, revealing a faster electrochemical process occurring in the novel cathode material during the removal and insertion of Li^+ ions from and into the material. These values were even higher than some values reported in literature. Charge/discharge capacity values calculated from the cyclic voltammetric profiles of the novel and pristine cathode materials showed a higher charge and discharge capacity of 209 mAh/g and 107 mAh/g for the novel cathode material compared to 159 mAh/g and 68 mAh/g for the pristine material, with a Coulombic efficiency of 76% compared to 64% for the pristine material. EIS studies also confirmed a reduced charge transfer resistance for the novel cathode material relative to the pristine. These results demonstrate that the novel Li_2MnSiO_4/Al_2O_3 cathode material possesses good structural and electrochemical reaction kinetics/dynamics over the pristine material. This can be attributed to the alumina nanoparticle surface coating which reduced the structural instability pertinent to the pristine Li_2MnSiO_4 cathode material and possibly decreased surface compliance towards undesired electrode-electrolyte reactions. The results obtained in this study suggest that Li_2MnSiO_4/Al_2O_3 possesses good structural and electrochemical performance for possible application in next generation lithium-ion batteries.

3.2 Recommendations

For future work on the study, the fabrication of coin cells using the synthesized materials to obtain their actual capacity profiles at different battery C-rates is absolutely necessary. Varying the surface coating ratio to obtain optimal performance and further verifying the effect of calcination temperature and time on the particle sizes of the synthesized materials will be carried out. Further CV experiments will also be conducted to investigate the cycleability and stability of the electrodes.

References

1. M. Armand, and J.M. Tarascon, *Building better batteries.* Nature, 2008. **451**(7179): p. 652-657.
2. N.S. Lewis, and D.G. Nocera, *Powering the planet: Chemical challenges in solar energy utilization.* Proceedings of the National Academy of Sciences, 2006. **103**(43): p. 15729-15735.
3. X.-P. Gao, and H.-X. Yang, *Multi-electron reaction materials for high energy density batteries.* Energy & Environmental Science, 2010. **3**(2): p. 174-189.
4. Fritz Beck, P.R., *Rechargeable batteries with aqueous electrolytes.* Electrochimica Acta, 2000. **45**: p. 2467–2482.
5. A. Väyrynen, and J. Salminen, *Lithium ion battery production.* The Journal of Chemical Thermodynamics, 2012. **46**(0): p. 80-85.
6. F. Cheng., et al., *Functional Materials for Rechargeable Batteries.* Advanced Materials, 2011. **23**(15): p. 1695-1715.
7. M.-K. Song., et al., *Nanostructured electrodes for lithium-ion and lithium-air batteries: the latest developments, challenges, and perspectives.* Materials Science and Engineering: R: Reports, 2011. **72**(11): p. 203-252.
8. J. Cho, S. Jeong, and Y. Kim, *Commercial and research battery technologies for electrical energy storage applications.* Progress in Energy and Combustion Science, 2015. **48**(0): p. 84-101.
9. M. Hu, X. Pang, and Z. Zhou, *Recent progress in high-voltage lithium ion batteries.* Journal of Power Sources, 2013. **237**(0): p. 229-242.
10 Z. Gong, and Y. Yang, *Recent advances in the research of polyanion-type cathode materials for Li-ion batteries.* Energy & Environmental Science, 2011. **4**(9): p. 3223-3242.
11. H.-W. Chan., et al., *New surface modified material for $LiMn_2O_4$ cathode material in Li-ion battery.* Surface and Coatings Technology, 2005. **200**(5–6): p. 1330-1334.
12. M.E. Arroyo-de Dompablo., et al., *On-demand design of polyoxianionic cathode materials based on electronegativity correlations: An exploration of the Li_2MSiO_4 system (Fe, Mn, Co, Ni).* Electrochemistry Communications, 2006. **8**(8): p. 1292-1298.

13. J.-P. Jegal, and K.-B. Kim, *Carbon nanotube-embedding $LiFePO_4$ as a cathode material for high rate lithium ion batteries.* Journal of Power Sources, 2013. **243**(0): p. 859-864.
14. H. Zhu., et al., *Facile synthesis of Li_2MnSiO_4/C/graphene composite with superior high-rate performances as cathode materials for Li-ion batteries.* Electrochimica Acta, 2015. **155**(0): p. 116-124.
15. R.J. Gummow, and Y. He, *Recent progress in the development of Li_2MnSiO_4 cathode materials.* Journal of Power Sources, 2014. **253**(0): p. 315-331.
16. F. Wang., et al., *Fast sol–gel synthesis of mesoporous Li_2MnSiO_4/C nanocomposite with improved electrochemical performance for lithium-ion batteries.* Journal of Electroanalytical Chemistry, 2013. **688**(0): p. 123-129.
17. H. Park., et al., *Li_2MnSiO_4/carbon nanofiber cathodes for Li-ion batteries.* Ionics, 2014. **20**(10): p. 1351-1359.
18. Y.-X. Li, Z.-L. Gong, and Y. Yang, *Synthesis and characterization of Li_2MnSiO_4/C nanocomposite cathode material for lithium ion batteries.* Journal of Power Sources, 2007. **174**(2): p. 528-532.
19. T. Muraliganth, K.R. Stroukoff, and A. Manthiram, *Microwave-Solvothermal Synthesis of Nanostructured Li_2MSiO_4/C (M = Mn and Fe) Cathodes for Lithium-Ion Batteries.* Chemistry of Materials, 2010. **22**(20): p. 5754-5761.
20. D. Sun., et al., *Multi-layered Al_2O_3/$Li_xV_2O_5$/LiV_3O_8 nanoflakes with superior cycling stability as cathode material for Li-ion battery.* Electrochimica Acta, 2015. **157**(0): p. 211-217.
21. L.J. Fu., et al., *Surface modifications of electrode materials for lithium ion batteries.* Solid State Sciences, 2006. **8**(2): p. 113-128.
22. G.T.K. Fey., et al., *Preformed Boehmite Nanoparticles As Coating Materials for Long-Cycling $LiCoO_2$.* Journal of Applied Electrochemistry, 2004. **34**(7): p. 715-722.
23. P.J. Hall, and E.J. Bain, *Energy-storage technologies and electricity generation.* Energy Policy, 2008. **36**(12): p. 4352-4355.
24. K.P.a.J. Tubke., ed. *Thermodynamics and Merchanistics*. Second Edition ed. Handbook of Battery Materials, ed. C.D.a.J. O.Besenhard. 2011, Wiley-VCH Verlag GmbH & Co. KGaA.
25. M. Winter, and R.J. Brodd, *What are batteries, fuel cells, and supercapacitors?* Chemical Reviews, 2004. **104**(10): p. 4245-4270.

26. K.C. Divya, and J. Østergaard, *Battery energy storage technology for power systems—An overview.* Electric Power Systems Research, 2009. **79**(4): p. 511-520.
27. L.T. Lam., et al., *Failure mode of valve-regulated lead-acid batteries under high-rate partial-state-of-charge operation.* Journal of Power Sources, 2004. **133**(1): p. 126-134.
28. A. Poullikkas., *A comparative overview of large-scale battery systems for electricity storage.* Renewable and Sustainable Energy Reviews, 2013. **27**(0): p. 778-788.
29. D. Berndt., *Electrochemical Energy Storage*, in *Battery Technology Handbook* H.A. Kiehne, Editor. 2003, Expert Verlag. p. 117-118.
30. P. Arora., and Z. Zhang, *Battery separators.* Chemical Reviews, 2004. **104**(10): p. 4419-4462.
31. T.N.C. Haisheng Chen, Wei Yang, Chunqing Tan, Yongliang Li, Yulong Ding, *Progress in electrical energy storage system: A critical review.* Progress in Natural Science, 2009. **19**: p. 291–312.
32. F. Feng, M. Geng, and D.O. Northwood, *Electrochemical behaviour of intermetallic-based metal hydrides used in Ni/metal hydride (MH) batteries: a review.* International Journal of Hydrogen Energy, 2001. **26**(7): p. 725-734.
33. M. Wakihara, *Recent developments in lithium ion batteries.* Materials Science and Engineering: R: Reports, 2001. **33**(4): p. 109-134.
34. B J.G. runo Scrosati., *Lithium batteries: Status, prospects and future.* Journal of power sources, 2010. **195**: p. 2419-2430.
35. A. Manthiram., *Materials Challenges and Opportunities of Lithium Ion Batteries.* The Journal of Physical Chemistry Letters, 2011. **2**(3): p. 176-184.
36. M.G. Theivanayagam., *Novel synthesis of nanostructured electrode materials for lithium-ion batteries*. 2010, Ph. D thesis, University of Texas at Austin, Retrieved from repositoreies.lib.utexas.edu.
37. A. Manthiram, and J. Kim, *Low temperature synthesis of insertion oxides for lithium batteries.* Chemistry of materials, 1998. **10**(10): p. 2895-2909.
38. C.O. Ikpo., *Development of high performance composite lithium ion battery cathode systems with carbon nanotubes functionalised with bimetallic inorganic nanocrystal alloys*. 2011, PhD thesis, University of Western Cape, Retrieved from etd.uwc.ac.za.
39. Y. Wang., *Design of Nanostructured Materials for Advanced Lithium Ion Batteries*. 2013, PhD, University of Technology, Sydney, Retrieved from lib.uts.edu.au.
40. J.W. Fergus., *Recent developments in cathode materials for lithium ion batteries.* Journal of Power Sources, 2010. **195**(4): p. 939-954.

41. J.B. Goodenough., ed. *Oxide Cathodes*. Advances in Lithium-Ion Batteries, ed. W.A.V.S.a.B. Scrosati. 2002, Kluver Academic/Plenum Publishers: New York.

42. B.N. Rao., et al., *Fast and Facile Synthesis of $LiMn_2O_4$ Nanorods for Li Ion Battery by Microwave Assisted Hydrothermal and Solid State Reaction Methods.* Int. J. Electrochem. Sci, 2014. **9**: p. 1207-1220.

43. X. Li, Y. Xu, and C. Wang, *Suppression of Jahn–Teller distortion of spinel $LiMn_2O_4$ cathode.* Journal of Alloys and Compounds, 2009. **479**(1): p. 310-313.

44. J. Liu, and A. Manthiram, *Understanding the improvement in the electrochemical properties of surface modified 5 V $LiMn_{1.4}2Ni_{0.4}2Co_{0.16}O_4$ spinel cathodes in lithium-ion cells.* Chemistry of Materials, 2009. **21**(8): p. 1695-1707.

45. J. Liu, and A. Manthiram, *Improved electrochemical performance of the 5 V spinel cathode $LiMn_{1.5}Ni_{0.42}Zn_{0.08}O_4$ by surface modification.* Journal of The Electrochemical Society, 2009. **156**(1): p. A66-A72.

46. A. Manthiram., et al., *Nanostructured electrode materials for electrochemical energy storage and conversion.* Energy & Environmental Science, 2008. **1**(6): p. 621-638.

47. R.R. Zhao., et al., *An improved Carbon-Coating Method for $LiFePO_4$/C composite derived from Fe^{3+} precursor.* Int. J. Electrochem. Sci, 2012. **7**: p. 10923-10932.

48. K. Park., et al., *Surface modification by silver coating for improving electrochemical properties of $LiFePO_4$.* Solid State Communications, 2004. **129**(5): p. 311-314.

49. A.V. Murugan., et al., *Dimensionally modulated, single-crystalline $LiMPO_4$ (M= Mn, Fe, Co, and Ni) with nano-thumblike shapes for high-power energy storage.* Inorganic chemistry, 2009. **48**(3): p. 946-952.

50. A. Kokalj., et al., *Beyond One-Electron Reaction in Li Cathode Materials: Designing $Li_2Mn_xFe_{1-x}SiO_4$.* Chemistry of Materials, 2007. **19**(15): p. 3633-3640.

51. C. Deng., et al., *Characterization of Li_2MnSiO_4 and Li_2FeSiO_4 cathode materials synthesized via a citric acid assisted sol–gel method.* Materials chemistry and physics, 2010. **120**(1): p. 14-17.

52. L. Bao., et al., *Progression of the silicate cathode materials used in lithium ion batteries.* Chinese Science Bulletin, 2013. **58**(6): p. 575-584.

53. S. Zhang., et al., *$Li_{2+x}Mn_{1-x}P_xSi_{1-x}O_4$/C as novel cathode materials for lithium ion batteries.* Electrochimica Acta, 2013. **107**: p. 406-412.

54. C.A. Fisher, N. Kuganathan, and M.S. Islam, *Defect chemistry and lithium-ion migration in polymorphs of the cathode material Li_2MnSiO_4.* Journal of Materials Chemistry A, 2013. **1**(13): p. 4207-4214.

55. S.-N. Lee., et al., *Cu–Li_2MnSiO_4-polyaniline composite hybrids as high performance cathode for lithium batteries.* Journal of Alloys and Compounds, 2015. **630**(0): p. 292-298.

56. I. Belharouak, A. Abouimrane, and K. Amine, *Structural and Electrochemical Characterization of Li_2MnSiO_4 Cathode Material.* The Journal of Physical Chemistry C, 2009. **113**(48): p. 20733-20737.

57. T. Yi., et al., *Local structure evolution of $Li_2Fe_{0.5}Mn_{0.5}SiO_4$ during delithiation/lithiation processes: A first-principles investigation.* Computational Materials Science, 2015. **99**(0): p. 96-104.

58. R. Gummow., et al., *Crystal chemistry of the Pmnb polymorph of Li_2MnSiO_4.* Journal of Solid State Chemistry, 2012. **188**: p. 32-37.

59. P. Ghosh., S. Mahanty, and R.N. Basu, *Improved electrochemical performance of Li_2MnSiO_4/C composite synthesized by combustion technique.* Journal of The Electrochemical Society, 2009. **156**(8): p. A677-A681.

60. N. Kuganathan, and M.S. Islam, *Li_2MnSiO_4 Lithium Battery Material: Atomic-Scale Study of Defects, Lithium Mobility, and Trivalent Dopants.* Chemistry of Materials, 2009. **21**(21): p. 5196-5202.

61. F. Wang., et al., *Fast sol–gel synthesis of mesoporous Li_2MnSiO_4/C nanocomposite with improved electrochemical performance for lithium-ion batteries.* Journal of Electroanalytical Chemistry, 2013. **688**: p. 123-129.

62. R. Gummow., et al., *Synthesis, structure, and electrochemical performance of magnesium-substituted lithium manganese orthosilicate cathode materials for lithium-ion batteries.* Journal of Power Sources, 2012. **197**: p. 231-237.

63. J. Zhu., et al., *Improved electrochemical performance of zinc oxide coated lithium manganese silicate electrode for lithium-ion batteries.* Journal of Alloys and Compounds, 2015. **633**: p. 194-200.

64. H. Wang., et al., *Lithium deficient mesoporous $Li_{2-x}MnSiO_4$ with significantly improved electrochemical performance.* Journal of Power Sources, 2014. **247**: p. 497-502.

65. C. Hwang., et al., *Fast ultrasound-assisted synthesis of Li_2MnSiO_4 nanoparticles for a lithium-ion battery.* Journal of Power Sources, 2015. **294**: p. 522-529.

66. H. Liu., *Design of nano-structured materials and their applications for lithium ion batteries*. 2010, PhD, University of Wollongong, Retrieved from ro.uow.edu.au.

67. L. Ji., et al., *Recent developments in nanostructured anode materials for rechargeable lithium-ion batteries.* Energy & Environmental Science, 2011. **4**(8): p. 2682-2699.

68. H.B. Wu., et al., *Nanostructured metal oxide-based materials as advanced anodes for lithium-ion batteries.* Nanoscale, 2012. **4**(8): p. 2526-2542.
69. J.B. Goodenough, and Y. Kim, *Challenges for rechargeable Li batteries†.* Chemistry of Materials, 2009. **22**(3): p. 587-603.
70. K. Xu., *Nonaqueous liquid electrolytes for lithium-based rechargeable batteries.* Chemical reviews, 2004. **104**(10): p. 4303-4418.
71. S.S. Zhang., *A review on the separators of liquid electrolyte Li-ion batteries.* Journal of Power Sources, 2007. **164**(1): p. 351-364.
72. U. Kumar Sen., et al., *Nano dimensionality: a way towards better Li-ion storage.* Nanoscience & Nanotechnology-Asia, 2013. **3**(1): p. 21-35.
73. Y. Wang., et al., *Nano active materials for lithium-ion batteries.* Nanoscale, 2010. **2**(8): p. 1294-1305.
74. D. Liu, and G. Cao, *Engineering nanostructured electrodes and fabrication of film electrodes for efficient lithium ion intercalation.* Energy & Environmental Science, 2010. **3**(9): p. 1218-1237.
75. I. Moriguchi., *Nanostructure-controlled Materials for Electrochemical Charging–Discharging.* Chemistry Letters, 2014. **43**(6): p. 740-745.
76. C.R. Sides., et al., *Nanoscale materials for lithium-ion batteries.* Mrs Bulletin, 2002. **27**(08): p. 604-607.
77. J. Maier., *Size effects on mass transport and storage in lithium batteries.* Journal of Power Sources, 2007. **174**(2): p. 569-574.
78. P.G. Bruce, B. Scrosati, and J.M. Tarascon, *Nanomaterials for rechargeable lithium batteries.* Angewandte Chemie International Edition, 2008. **47**(16): p. 2930-2946.
79. J. Goldstein., et al., *Scanning electron microscopy and X-ray microanalysis: a text for biologists, materials scientists, and geologists*. 2012: Springer Science & Business Media.
80. Z.L. Wang., *New developments in transmission electron microscopy for nanotechnology.* Advanced Materials, 2003. **15**(18): p. 1497-1514.
81. R. Sahu, and S. Mordechai, *Fourier transform infrared spectroscopy in cancer detection.* 2005.
82. J.D.S.a.V.H. Grassian., *ATR-FTIR Spectroscopy in the Undergraduate Chemistry Laboratory.* Journal of Chemical Education, 2008. **85**(2): p. 279-281.
83. N.E. Johnson., *X-ray Diffraction Simulation using Laser Pointers and Printers.* Journal of Geosciences Education, 2001. **49**(4): p. 346-350.

84. M.-Y. Liao., et al., *Local electronic structure of $LiMn_2O_4$ probed by solid state 7 Li-NMR.* Journal of Physics and Chemistry of Solids, 2001. **62**(9): p. 1893-1898.

85. C. Ferrara., *Solid State NMR studies of functional oxides*. 2014, PhD thesis, Ecole normale supérieure de lyon-ENS LYON; Università degli studi (Pavie, Italie), Retrieved from archives.ouvertes.fr.

86. D.S. Middlemiss., et al., *Density functional theory-based bond pathway decompositions of hyperfine shifts: Equipping solid-state NMR to characterize atomic environments in paramagnetic materials.* Chemistry of Materials, 2013. **25**(9): p. 1723-1734.

87. P. Van der Heide., *X-ray photoelectron spectroscopy: an introduction to principles and practices*. 2011: John Wiley & Sons.

88. Z. Piero., *Inorganic Electrochemistry - Theory, Practice and Application.* The Royal Society Of Chemistry, 2003: p. 49-111.

89. J.G.O.a.R.A. Osteryoung., *Square wave Voltammetry.* Analytical Chemistry, 1985. **57**(1): p. 101A-110A.

90. M. Pacios, I.M.n.-F.n., R. Villa, P. Godignon, M. Del Valle, J. Bartrolí and M.J. Esplandiu *Carbon Nanotubes as Suitable Electrochemical Platforms for Metalloprotein Sensors and Genosensors*, in *ISBN: 978-953-307-566-2*, M. Naraghi, Editor. 2011, Universitat Autònoma de Barcelona, Spain retrived from InTech: http://www.intechopen.com/books/carbon-nanotubes-growth-and applications/carbonnanotubesas-suitable-electrochemical-platforms-for metalloprotein-sensors-and-genosensors: Barcelona. p. 209-324.

91. S. Devaraj., et al., *Sol–gel derived nanostructured Li_2MnSiO_4/C cathode with high storage capacity.* Electrochimica Acta, 2013. **102**: p. 290-298.

92. M. Xie., et al., *Template-Assisted Hydrothermal Synthesis of Li_2MnSiO_4 as a Cathode Material for Lithium Ion Batteries.* ACS Applied Materials & Interfaces, 2015. **7**(20): p. 10779-10784.

93. K. Gao., et al., *Thermal dynamics and optimization on solid-state reaction for synthesis of Li_2MnSiO_4 materials.* Journal of Power Sources, 2012. **211**: p. 97-102.

94. L.A. Prado., et al., *Surface modification of alumina nanoparticles with silane coupling agents.* Journal of the Brazilian Chemical Society, 2010. **21**(12): p. 2238-2245.

95. J.X. Shuangke Liu, Dezhan Li, Yun Hu, Xiang Liu, Kai Xie, *High capacity Li_2MnSiO_4/C nanocomposite prepared by sol-gel method for lithium-ion batteries.* Journal of Power Sources, 2013. **232**: p. 258-263.

96. K.K. Aravindan, S. Ravi, S. Amaresh, S. Kim and S. Lee, *Adipic acid assisted sol–gel synthesis of Li_2MnSiO_4 nanoparticles with improved lithium storage properties.* Journal of Materials Chemistry 2010. **20**: p. 7340-7343.

97. Y.X. Wengang Liu, Rong Yang, *Synthesis, characterization and electrochemical performance of Li_2MnSiO_4/C cathode material by solid-state reaction.* Journal of Alloys and Compounds, 2009. **480**: p. L1-L4.

98. M. Arroyo-deDompablo., et al., *On the energetic stability and electrochemistry of Li_2MnSiO_4 polymorphs.* Chemistry of Materials, 2008. **20**(17): p. 5574-5584.

99. M.R. Gregor Mali, Chutchamon Sirisopanaporn, and Robert Dominko, *Understanding ^{6}Li MAS NMR spectra of Li_2MSiO_4 materials (M = Mn, Fe, Zn).* National Institute of Chemistry, Hajdrihova 19, SI-1001 Ljubljana, Slovenia retrieved from http://www.researchgate.net/publication/5175115 2011: p. 1-26.

100. C. Sirisopanaporn., et al., *Polymorphism in Li2(Fe,Mn)SiO4: A combined diffraction and NMR study.* Journal of Materials Chemistry, 2011. **21**(44): p. 17823-17831.

101. D. Rangappa., et al., *Ultrathin nanosheets of Li_2MSiO_4 (M= Fe, Mn) as high-capacity Li-ion battery electrode.* Nano Letters, 2012. **12**(3): p. 1146-1151.

102. X. Kong., et al., *Size controlled synthesis of uniform Li_2MnSiO_4 nanospheres and their electrochemical behaviors in lithium-ion batteries.* Int. J. Electrochem. Sci, 2012. **7**: p. 5565-5573.

103. G.B. Ben Amor, M. Jacquet, G. Nanse, P. Fioux, M. Nardin, *XPS characterisation of plasma-treated and alumina-coated PMMA.* Applied Surface Science, 2000. **153**: p. 172-183.

104. W.G.S. van den Brand, H. Terryn and J. H. W. de Wit, *Correlation between hydroxyl fraction and O/Al atomic ratio as determined from XPS spectra of aluminium oxide layers.* Surface and Interface Analysis, 2004. **36**: p. 81-88.

105. S. Zhang., et al., *Cr-doped Li_2MnSiO_4/carbon composite nanofibers as high-energy cathodes for Li-ion batteries.* Journal of Materials Chemistry, 2012. **22**(29): p. 14661-14666.

106. S.-W. Lee., et al., *Electrochemical characteristics of Al_2O_3-coated lithium manganese spinel as a cathode material for a lithium secondary battery.* Journal of Power Sources, 2004. **126**(1–2): p. 150-155.